Experimental study of information engines at the mesoscopic scale

Aubin Archambault

THÈSE

en vue de l'obtention du grade de Docteur, délivré par

l'ÉCOLE NORMALE SUPERIEURE DE LYON

École Doctorale N° 52
École doctorale de Physique et Astrophysique de l'Université de Lyon

Discipline : Physique

Soutenue publiquement le 12/12/2023, par :

Aubin ARCHAMBAULT

Experimental study of information engines at the mesoscopic scale

Devant le jury composé de :

GENET, Cyriaque	Directeur de recherche CNRS Uni.Strasbourg	Rapporteur
ROLDAN, Edgar	Associate Research Officier ICTP	Rapporteur
MALLICK, Kirone	Directeur de recherche CEA CEA Saclay	Examinateur
CRAUSTE-THIBIERGE, Caroline	Chargée de recherche CNRS ENS de Lyon	Directrice de thèse
BELLON, Ludovic	Directeur de recherche CNRS ENS de Lyon	Co-Directeur de thèse

"Physics doesn't care if your question is weird. It just gives you the answer, without judging. For example, according to the comprehensive 456-page handbook *Cheese Rheology and Textures...*"
Randall Munroe, "How To, absurd scientific advice for common real-world problems" ed. John Murray

Contents

Acknowledgements/Remerciements

I will take a few words in French here to thank a lot of very nice people I met in Lyon and who supported me during my PhD. I owe them a lot and maybe I could have done a PhD without them, but not of this quality and not with such pleasure.

Paradoxalement, ces mots sont les derniers du manuscrit que j'écris. Je ne suis pas forcément habile avec les mots, alors j'irai un peu à l'essentiel.

Une thèse c'est long, et ça ne se fait pas seul au fond de sa cave enchainé à sa manip. Je tiens à remercier Sergio, pour les discussions de physique et ses milliers d'idées à la seconde, souvent bonnes et régulièrement géniales. Ludovic pour son immense capacité à trouver des solutions qui règlent quatre problèmes d'un coup ainsi que sa connaissance des microleviers et sa maîtrise de la FPGA qui m'ont permis de faire tout ce que vous allez lire dans la suite (ou pas, je ne vous en voudrai pas). Et bien sûr Caroline, qui a accepté de me prendre en thèse, qui m'a encadré jusqu'au bout, qui a passé son HDR, qui m'a montré comment coller des billes, qui s'est creusée la tête longuement avec moi sur Casimir, qui a suivi sans broncher quand j'ai décidé de faire de la thermo stochastique, qui m'a aidé à comprendre comment fonctionne l'unused information, qui m'a appris à être un physicien, et toujours avec plein de bonne humeur. La qualité incroyable de ce trio d'encadrants, c'est la place et l'autonomie qu'ils m'ont laissées. Plus qu'un thésard, je me suis senti comme un collaborateur dans le groupe.

Je tiens à remercier mes rapporteurs, Edgar Roldan et Cyriaque Genet, pour leurs retours et suggestions sur le manuscrit ainsi que Kirone Mallick qui a accepté de compléter et présider ce jury. Je les remercie pour leur bienveillance et les discussions scientifiques autour de ma thèse qui m'ont fait comprendre que mon travail peut aussi être intéressant pour d'autres chercheurs.

Les autres (anciens) membres du groupe, Baptiste, Richard, Alex, Jorge, Basile, Nicolas, Salambô, Jérôme, et Benjamin qui ont animé les salles de manip et avec qui j'ai beaucoup discuté de physique et des farces de la manip.

Le labo de physique, les permanents accueillants, ravis de parler de leur recherche, du monde de la recherche et du reste avec des jeunes qui débarquent, en particulier Audrey, Valérie, Pascal, Sylvain et Mokhtar. Les autres doctorants et post-doc qui rendent ce lieu de travail aussi vivant. Tous les gens que j'ai pu croiser au café, qui participent aux discussions le midi, et qui font de ce labo un lieu agréable. Merci à la bande de 11h45 (sauf si séminaire), Youssef, Lucien, Geoffroy, Baptiste et Yohann pour la compagnie le midi. J'ai une pensée particulière pour la petite bande qui s'est tenu compagnie en 2020-2021, pendant les couvre-feux, au milieu de l'hiver.

Un grand merci au service administratif, Nadine, Érika, Laurence, Nelly, Fatiha qui nous sauvent et nous rendent la vie bien plus simple lorsqu'on doit prendre un billet de train ou commander du matériel. Le tout avec efficacité et gentillesse.

Je remercie aussi les services d'ingénieries mécanique et électronique, qui nous font gagner un temps incroyable, sont toujours de très bon conseil et savent rester calmes quand un physicien débarque avec son idée saugrenue. Un merci particulier à Frank Vittoz pour son travail sur la rôtissoire à micro-leviers que vous pouvez admirer au chapitre 9 figure 9.6.

Je remercie Samuel, ancien post-doc au labo, qui m'a encadré quand j'étais jeune stagiaire

de L3 qui découvrait la thermo et les manips d'AFM, et que j'ai embarqué faire des jeux de société en échange pendant que la manip tournait après minuit.

Le Laboratoire de Physique a la chance d'avoir deux ingénieurs de recherche exceptionnels. Vincent Dolique qui m'a beaucoup appris sur l'utilisation des microscopes électronique et à force atomique, ainsi que sur les processus de microfabrication, et Artyom Petrosyan, qui fait des merveilles en optique, en électronique, et pas que, qui m'a souvent sorti le truc exact dont j'avais besoin et qu'il gardait précieusement au fond d'un tiroir.

Ayant fait ma licence et mon master au département de physique de l'ENS, j'en profite pour remercier tous les intervenants et intervenantes de la formation. On a la chance d'avoir une équipe enseignante motivée et impliquée, à l'écoute des élèves, et qui les suivent de près pendant leur 4 années à l'ENS. J'ai eu également la chance de passer de l'autre côté en donnant les TD de matière condensée et en encadrant les mini-projets d'électronique. Merci beaucoup à Peter et Sylvain de m'avoir fait confiance sur ces enseignements et de m'avoir impliqué à ce point dans la conception des sujets et le lien avec les étudiants et étudiantes. Je remercie également mes élèves, qui ont été bien sages, qui ont bien écouté, qui ont fait l'effort de venir le lundi matin à 8h, qui ont posé plein de questions auxquelles je n'avais pas la réponse, et qui ont testé le TP d'amplification avec du Joe Hisaishi.

Sortons un peu du labo, mais restons dans l'école. Merci à toute la communauté de ludistes avec qui j'ai fait beaucoup trop de trucs ces 7 dernières années. On a fondé une association, on a organisé un weekend de jeux non-stop pour 4 ENS, deux fois, on a monté une chorale qui veut pas chanter juste mais juste chanter, on a trié des BD et changé des étagères, le tout en buvant du thé et en mangeant des cookies (mais pas au dessus des BD). C'était chouette de faire tout ça, et en plus ça m'a beaucoup appris sur la façon de travailler en équipe. Vive l'associatif !

Un gros et grand merci aux copains de la fanfare pour la bonne ambiance en répét les jeudis soirs, pour les crêpes, pour m'avoir appris le trombone et la percu de zéro, pour les deux tournées super sympa en été, les moments de détente au Foyer à n'importe quelle heure de la semaine. Merci à Raphaël, mon grand maître du trombone, Benjamin, mon senpai de la percu, et Rémi pour ses regards noirs.

Particulièrement merci à Yohann qui m'a trainé à la fanfare, qui avait bien raison, et qui a été un ami précieux pendant ma thèse.

Merci à Garance de m'avoir embarqué dans du jeu de rôle Pokémon et m'avoir fait retomber dans cet univers cher à mon enfance. (Je suis pas si vieux que ça en vrai, hein.)

Merci à Lison pour le mignon, les discussions salées jusqu'à pas d'heure et l'hébergement à Marseille.

Merci à Caroline pour les discussions crochet, Pratchett et jardinage.

Merci à Élodie pour le fromage, les gâteaux, les soirées jeux vidéo sur Crypt et MH, les coiffures rigolotes, les corrections de code Python et tout le reste.

Merci à mes parents, mon frère et ma sœur qui ont "tout compris à ce que je fais, mais oui c'est très bien, tu reveux de la soupe ?" et sont toujours là quand j'ai besoin d'eux. (Je passerai le permis un jour ! (Je le pressentiment que cette phrase va devenir de plus en plus drôle avec les années.))

Merci à Eden. Tu sais que bloup ? ❤

Merci à toutes celles et ceux que je n'ai pas nommés faute de place, ou que j'ai oublié faute de cerveau.

Si vous êtes toujours là, je vous souhaite une bonne lecture, au pays des fluctuations thermiques et des démons de Maxwell.

Chapter 1

Introduction

The quest for an unlimited energy source, a perpetual motion machine, can seem absurd and vowed to fail nowadays. A perpetual motion machine is a device that once set in motion, would keep providing energy by itself, without ever stopping. This quest is so foolish that many great minds tried to tackle it throughout history. Leonardo Da Vinci, for example, proposed many designs of wheels which would keep on spinning indefinitely (see figure 1.1), but he concluded [1, 2]:

> Seekers after perpetual motion, how many vain chimeras have you pursued? Go and take your place with the alchemists.

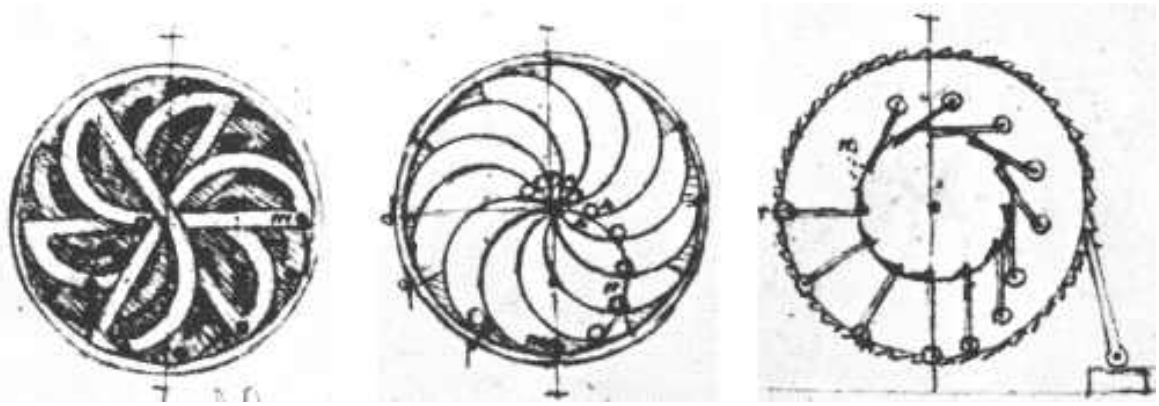

Figure 1.1: Design of perpetual motion wheel by Leonardo Da Vinci. Taken from [1]. The idea behind these design is that a part of the wheel is mobile, so that one side of the wheel is always heavier than the other, increasing the torque from gravitational forces. However, Da Vinci understood that doing so also increases the moment of inertia of the wheel and reduces the effect of torque, the two effects cancelling each other.

This search for a device that once in motion would keep providing energy by itself, without ever stopping has been compared to the search for the philosopher stone [3]. While it is commonly accepted that such a device is impossible, the reasons behind are not so easy to understand, and required many years of scientific work in the field of thermodynamics.

1.1 Macroscopic thermodynamics

Thermodynamics is the science describing the laws behind energy exchange and transformation. It was developed during the industrial revolution, to answer questions about the operation of steam engines. The main questions were about the limit to the efficiency of these engines. How

much mechanical work can be extracted? What is the maximal power that can be achieved? What is the required energy input? Thermodynamics answers all these questions with only two fundamental Laws.

The first Law of thermodynamic was explicitly stated by Clausius in 1850, in [4].

> In a thermodynamic process involving a closed system, the increment in the internal energy is equal to the difference between the heat accumulated by the system and the work done by it.

This is a very strong constraint on the operation of engines or any kind of physical transformation. This law states that a system can store energy in a form here called "internal energy", so that energy is conserved during any process. A distinction is made between work, energy exchanged by mechanical means, and heat, exchanged by thermal means.

While the First Law of thermodynamic is a very powerful result, it lacks predictive power. Indeed, it puts a strong constraint on the types of transformation that are allowed, but it doesn't rule out heat flowing from cold objects to hot objects. Another example is that one could imagine a boat whose motion is powered by energy taken from the ocean, that is cooled by the operation.

To complement the First Law, Clausius introduces in 1865 the concept of entropy, a quantity linked to the heat fluxes with a thermostat during a transformation. He concludes:

> The entropy of the universe tends to a maximum.

While this statement is quite loose, it is indeed valid for any isolated system and can be used to predict its evolution. This has strong implications again on the operation of all kind of machines, one of the stronger result being a derivation of Carnot's maximum efficiency for heat engines in 1824 [5].

These two principles are very powerful tools and allow us to understand the limit of engines or any kind of cyclic machines (refrigerators, heat pumps, etc...). However, they rely on two quantities, internal energy and entropy, for which no interpretation is given.

1.2 Microscopic origins

The microscopic explanation of the nature of internal energy and entropy comes from works by Maxwell and Boltzmann on the kinetic theory of gases. Their approach is based on two main ideas. First, the assumption that a gas is made of very small particles in motion, colliding with each other. Second, the idea that the number of particles is so large that a statistical approach is enough to recover the overall behaviour of the gas. Maxwell derived the probability distribution of speed in the gas at equilibrium and linked it to the macroscopic pressure [6]. It also gives an understanding of internal energy in term of the sum of the kinetic energy of all the particles in the gas.

In 1872, Boltzmann generalised Maxwell's distribution to explain the role of collisions in the relaxation toward equilibrium [7]. In his work, Boltzmann notices the existence of a function, H, that can only decrease during the evolution of the gas, very similarly to the entropy used by Clausius. This H-theorem by Boltzmann was one of the first statistical understanding of the second law of thermodynamics.

This successful microscopic and statistical approach introduces the notion of probability distribution and thus thermal fluctuations. Years before, Robert Brown, a botanist, reported on the motion of particles from grains of pollen in a fluid. He also observed the same kind of motion in inorganic particles, thus ruling out any kind of biological activity [8]. This phenomenon, now called Brownian motion, was left unexplained until 1905, when Einstein [9] proposed a model

based on an atomistic model for the fluid, and a random motion in the fluid due to the thermal distribution of speeds. This model was tested experimentally by Jean Perrin in 1913 [10]. His verification of Einstein's predictions was a confirmation of the atomistic theory of matter.

This new understanding, physical and mathematical, of the microscopic nature of matter raises many questions about the fluctuations and how they impact the laws of thermodynamics.

1.3 The role of fluctuations

One of the main questions about fluctuations is the possibility of extracting energy from the fluctuations. If a particle in a fluid moves spontaneously, maybe this motion can be used to produce work. In 1912, Marian Smoluchovksi proposed a thought experiment in which a ratchet is used to rectify fluctuations [11]. In this thought experiment a paddle wheel immersed in a gas rotates under thermal fluctuations. A ratchet is used to allow the wheel to rotate only in one direction, blocking it in the other direction. By selecting only fluctuations pushing the wheel in one direction, the system could be used to elevate a mass, thus extracting work from a monothermal source, in contradiction with the second law of thermodynamics.

This thought experiment is similar to another thought experiment proposed by Maxwell in 1871. Maxwell considers the case of a box full of gas, with an observer, able to measure accurately the position and speed of the molecules. By controlling a trapdoor, this observer can sort the particle of the gas. If this observer lets the slow particles go to one side of the box and the faster ones go to the other side, they can construct a temperature difference from a system initially homogeneous, thus reducing its entropy at no cost. Such an observer, now called Maxwell Demon, would break the second law of thermodynamics. Many examples of such thought experiments have been proposed, notably by Szilard [12].

A first solution to the paradox of the Brownian ratchet was proposed in 1962 by Feynman in his lectures [13], by considering the temperature of the ratchet itself. Since the ratchet has a temperature, it must fluctuates and induces errors in the process. In order for the Brownian ratchet to work, the ratchet needs to be cooled at a lower temperature than the gas.

A second explanation came from Landauer. He introduced in 1961 a now famous principle linking information and thermodynamics [14]. He showed that the erasure of one bit of information is linked to a heat cost of at least $k_B T \log(2)$, where k_B is Boltzmann constant and T the temperature. This fundamental limit in the operation of information bits has been extensively verified experimentally [15–24] and links thermodynamics to the field of information theory, a field transverse to physics, economy, computer science, and many other domains [25, 26]. Since to operate in a cycle, a Maxwell Demon has to erase its memory, it introduces an energy cost, making the demon compatible with the second Law of thermodynamics.

1.4 Modern thermodynamics

The main idea from Landauer is that information is physical. Since information can be used to extract energy from fluctuations, we need a way to include it in the laws of thermodynamics. Many questions are opened, similar to ones from the early stages of thermodynamics. What kind of engine can we build using information? What is the maximum amount of energy we can extract from such an engine? How can we measure information? How does it affects the way we store and operate information? [27]

A powerful framework for the study of thermodynamics at the scale of fluctuations, stochastic thermodynamics, will be presented in the next chapter. The rest of this manuscript presents a versatile experimental device and its applications to the study of different kinds of information engines. The last two chapters are independent and present instrumental development for

small forces measurements.

Chapter 2

Introduction: Stochastic Thermodynamics

Stochastic thermodynamics applies generally to microscopic systems, where the thermal fluctuations are a main component of the physics observed [28]. It is used to described the motion of small particles in a fluid, be it passive colloids, bioparticles, or small bacteria. One of the main feature of stochastic thermodynamics is its large domain of validity, across many classes of systems and far from equilibrium [3].

2.1 Equation of motion and energy balance at the mesoscopic scale

The description of motion of small objects under thermal noise is difficult due to the random nature of the forces from the surrounding fluid. The fluid is composed of many particles, typically 10^{23}, on the scale of Avogadro's number. An exact solution of the equations of motion would require knowledge and mathematical treatment of all the positions and velocities of the fluid particles.

2.1.1 Langevin equation

To circumvent this problem, a probabilistic approach can be used. It was first proposed by Paul Langevin to describe Brownian motion in 1908 [29]. He models the force from the fluid as a random force η, whose amplitude follows a Gaussian distribution. The collision time between fluid particles is considered negligible for the dynamic of the mesoscopic object. This leads to zero correlation in the random force.

The 1D Langevin equation for the position x of a mesoscopic particle of mass m immersed in a fluid of viscosity γ is :

$$m\ddot{x} + \gamma\dot{x} = \eta(t) + F(x,t) \tag{2.1}$$

where F is an external force applied on the particle. The term $\eta(t)$ follows a Gaussian distribution with:

$$\langle\eta\rangle = 0 \quad \langle\eta(t)\eta(t')\rangle = 2\gamma k_B T\delta(t-t') \tag{2.2}$$

For particles immersed in a fluid such as water, the inertial time m/γ is often smaller than the time scale at which the phenomenon is studied. For example, for a SiO_2 silica microsphere with a diameter of 4 µm, the inertial time is on the order of the tenth of a microsecond. In this regime, often called overdamped, the inertial term can be neglected in eq.2.1. Conversely, the more generic regime is called underdamped, or inertial.

The Langevin equation cannot be solved analytically but provides a description of mesoscopic systems on which we can compute averaged quantities or probability distributions.

2.1.2 Stochastic energetics

Each realisation of the thermal noise $\eta(t)$, corresponds to a unique trajectory $x(t)$, determined by the Langevin equation. This equation can be used to construct quantities to study individual trajectories. Sekimoto proposed in 1997 a way to reconstruct the 1st Law of thermodynamics at the scale of each trajectory [30].

We consider the case of a conservative force associated to potential $U(x;\lambda)$ with a control parameter λ: $F(x,t) = -\frac{\partial U(x;\lambda)}{\partial x}$. λ is an external parameter that can be tuned by the operator.

$$m\ddot{x} + \gamma\dot{x} = \eta(t) - \frac{\partial U(x;\lambda)}{\partial x} \tag{2.3}$$

We consider a displacement of the system dx over a time dt. By multiplying 2.3 by dx, we obtain an energy balance:

$$m\ddot{x}dx + \gamma\dot{x}dx = \eta(t)dx - \frac{\partial U(x;\lambda)}{\partial x}dx \tag{2.4}$$

$$d\left(\frac{1}{2}m\dot{x}^2\right) + \frac{\partial U(x;\lambda)}{\partial x}dx = (-\gamma\dot{x} + \eta(t))dx \tag{2.5}$$

$$\tag{2.6}$$

The right-hand side is the energy given to the system by the forces from the bath. We can define the infinitesimal heat exchanged toward the system dq:

$$dq = (-\gamma\dot{x} + \eta(t))dx \tag{2.7}$$

The left-hand side is almost the variation of energy of the system. Indeed the term $\frac{\partial U(x;\lambda)}{\partial x}dx$ is not the total derivative of $U(x;\lambda)$, a term $\frac{\partial U}{\partial \lambda}d\lambda$ must be added.

$$d\left(\frac{1}{2}m\dot{x}^2\right) + dU = \frac{\partial U(x;\lambda)}{\partial \lambda}d\lambda + dq \tag{2.8}$$

The left-hand side is then the infinitesimal variation of mechanical energy. The term $dK = d\left(\frac{1}{2}m\dot{x}^2\right)$ is the variation of kinetic energy. On the right hand side, we have the term dq and the added term $\frac{\partial U(x;\lambda)}{\partial \lambda}d\lambda$ which must correspond to the work dw performed by the operator on the system when tuning the potential:

$$dw = \frac{\partial U(x;\lambda)}{\partial \lambda}d\lambda \tag{2.9}$$

We then recover an expression of the energy balance equivalent to the first Law of thermodynamics with a definition of work and heat at the scale of the individual trajectory:

$$dK + dU = dw + dq \tag{2.10}$$

This definition of dq can hardly be used to compute experimentally a heat flux. Indeed, it requires knowledge of the exact realisation of the thermal noise $\eta(t)$ to compute dq. Most of the time the only observables accessible are the position x and the control parameter λ.

$$dq = dK + dU - dw \tag{2.11}$$

$$= dK + \frac{\partial U}{\partial x}dx + \frac{\partial U}{\partial \lambda}d\lambda - dw \tag{2.12}$$

$$= d(\frac{1}{2}m\dot{x}^2) + \frac{\partial U}{\partial x}dx \tag{2.13}$$

where the definition of dw is used to cancel the term $\frac{\partial U}{\partial \lambda} d\lambda$. This expression for dq is much more useful experimentally as it relies only on measurements of x and λ.

The Langevin equation is a useful mathematical framework to described degrees of freedom submitted to random noise and has many applications in physics and beyond, as it allows us to construct thermodynamics quantities from experimental observables. This framework provides already an extension of the First Law of thermodynamics in the form of eq. 2.10.

2.2 Fluctuation theorems

At the mesoscopic scale, since phenomena are driven by random forces, quantities are better described by their probability distributions. By properly taking into account the whole distribution, equalities can be deduced as an extension of the macroscopic inequalities on averaged quantities [31]. Stochastic thermodynamics have provided many results on these distributions. While these fluctuation theorems are very general and apply to many systems even far from equilibrium, they contain interesting relations between out-of-equilibrium fluctuations and equilibrium properties of the systems [32].

2.2.1 Jarzynski equality

In 1997, Jarzynski derived an expression linking the fluctuations of work during a transformation to the free energy difference ΔF between the initial and final states [33]. This result is valid as long as the initial and final states are equilibrium states. However, the transformation between the states can be out-of-equilibrium.

The Jarzynski equality (JE) states that:

$$\langle e^{-\beta w} \rangle = e^{-\beta \Delta F} \tag{2.14}$$

where w is the work performed on the system during the transformation, $\langle \cdot \rangle$ notes ensemble averages, and $\beta = 1/k_B T$.

This results is often cited as an extension to the Second Law of thermodynamics [34]. Indeed, by using the convexity of exponential functions, we recover the 2$^{\text{nd}}$ Law of Thermodynamics:

$$\langle w \rangle \geq \Delta F \tag{2.15}$$

The JE is one of the major results of stochastic thermodynamics and has a lot of experimental applications since it links ΔF, an equilibrium property, to the whole distribution of w along a potentially out-of-equilibrium transformation. One of the first experimental test of the Jarzynski equality was made in 2002 by measuring the free energy change needed for folding and unfolding a RNA strain [35]. This relation was also generalised for various cases, such as non equilibrium steady states [36–38], or the quantum case [39–41].

2.2.2 Crooks' relation

In 1999 Crooks derived another constraint on the distribution of work [42]. Consider the transformation of the system from state i at time $t = 0$ to state f at $t = t_f$, by driving an external parameter $\lambda(t)$. Crooks' relation links the probability distribution of work, $P^F(w)$ during this transformation to the distribution of work, $P^R(w)$, measured during the time-reverse process obtained by driving the system from f to i with a driving $\lambda^\dagger(t) = \lambda(t_f - t)$:

$$\frac{P^F(+w)}{P^R(-w)} = e^{\beta(w - \Delta F)} \tag{2.16}$$

This result generalises the Jarzynski equality. Indeed, by averaging over w, we recover eq.2.14.

Crooks' relation is a very famous example of Fluctuation Theorems and has been verified experimentally at many occasions [43, 44].

The Jarzynski equality and Crooks' relation are two strong constraints on the fluctuations in a system. Their many applications and generalisations in the literature show how useful they are for extracting equilibrium properties from out-of-equilibrium processes. This universality makes them great tests of experimental setups, as verifying the Jarzynski equality or Crooks' relation indicates good accounting of the thermal fluctuations in an experiment.

2.3 Including information

The previous results apply to a lot of systems driven out of equilibrium. However, as they reproduce the Second Law of thermodynamics, we expect them to fail in the case of a measurement with feedback such as the Maxwell Demon or Szilard's engine. In this case, $\lambda(t)$ applied on the system is made dependent on the result of a measurement performed on the system. We first give an example of such protocol before presenting the extension proposed to take into account the role of information.

2.3.1 Szilard's engine

The role of backaction on a system has been known for a long time. Szilard's gave a famous example through a thought experiment in 1929 [12]. In this experiment, illustrated in figure 2.1, a single gas molecule is placed in a box of volume $2V$. An observer measures the position of the particle in the box and a wall is placed in the middle of the box, splitting it into two domains of volume V. Note that the introduction of a wall in the middle of the box is an operation that can be done while spending as little work as wanted and is thus considered to be done without any energy exchange with the system. Based on the outcome of the measurement, the wall is moved in order to perform an expansion of the gas. If we consider this single molecule to be an ideal gas at pressure P, we can use the law of ideal gas to compute the average work applied to the system by the expansion:

$$\langle w \rangle = -\int_v^{2v} P dv = -\int_v^{2v} \frac{k_B T}{v} dv = -k_B T \log(2) \tag{2.17}$$

After the extraction, the system is back to the initial state at temperature T in a volume $2V$.

This transformation can be operated in a cycle and the free energy change of the system is $\Delta F = 0$. Since $w < 0$, this violates the Jarzynski equality (eq.2.14) and the 2^{nd} Law (eq.2.15).

The experimental realisation of a Szilard's engine and other feedback protocols has been recently an active field of research [45, 46], both theoretically, with many models of engine proposed [47, 48], and experimentally [17, 49]. These experimental realisations make it possible to test the validity of proposed extensions of the theorems in the case of backaction.

2.3.2 Extension of the Jarzynski equality

One of the most promising extension of the Jarzynski equality was published by Sagawa and Ueda [50]. They worked on extending the validity of the Jarzynski equality for protocols with measurement and feedback. For a measurement with outcome y, performed on a system at a point Γ of the phase space, they define an information $I[y, \Gamma] = \log(P(y|\Gamma)/P(y))$. This is the mutual information between the measurement outcome and the state of the system. Using this definition, they proove that:

$$\langle e^{-\beta w - I} \rangle = e^{-\Delta F} \tag{2.18}$$

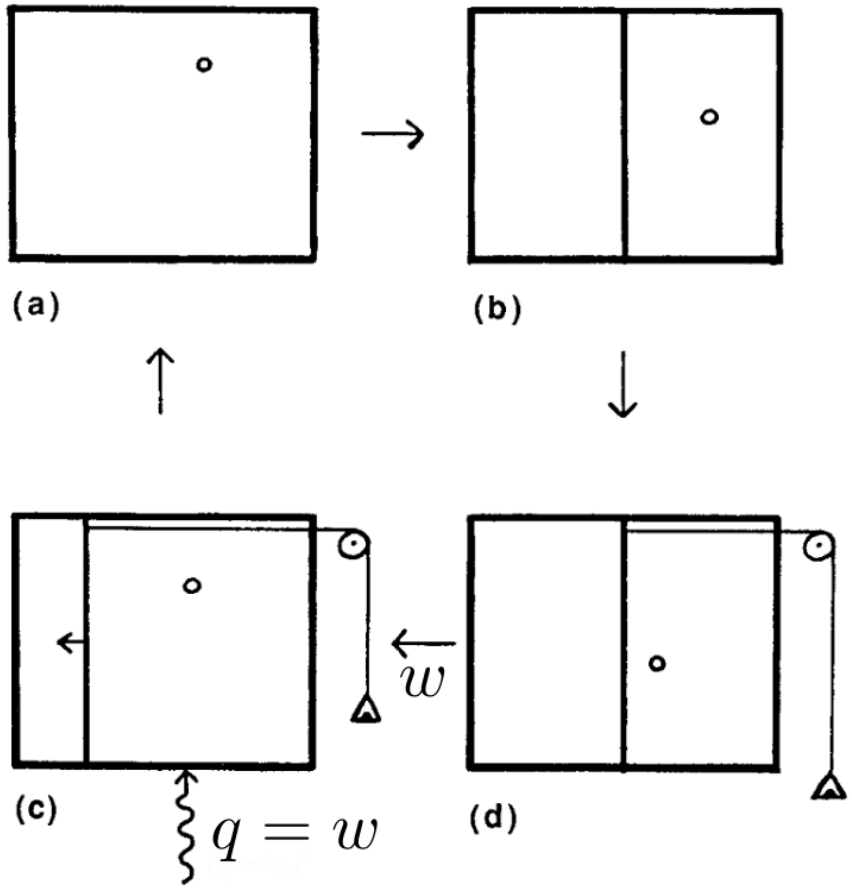

Figure 2.1: The Szilard engine. Reproduction from [45]. a) The particle is initially in equilibrium at temperature T. b) A wall is inserted in the middle of the box. c) Depending on the position of the particle, a mass is attached to the wall. d) Due to random collisions, the wall is pushed to the side and the mass is lifted. On average, a heat flux q from the thermal bath compensates the work w taken from the particle.

where the ensemble average $\langle\cdot\rangle$ is taken over y and Γ.

From this equality, we can derive a bound on the work extracted, using once again the convexity of exponential functions:

$$\langle w\rangle > \Delta F - \langle I\rangle \tag{2.19}$$

Compared to the 2nd Law from eq. 2.15, the information extracted from the system lowers the bound on the work applied to the system. In the case of a cyclic operation such as Szilard's engine where $\Delta F = 0$, if $I > 0$ this bound is compatible with $\langle w\rangle < 0$ which allows work extraction from the system. Taking into account the information used in the cycle by the feedback, the fundamental laws of thermodynamics can be redefined and extended. This both new and important result was verified experimentally in a system analogous to a Szilard engine, using a single electron box [51].

Another approach proposed by Sagawa and Ueda in [50] is to write a Jarzynski equality with an error term $\gamma \neq 1$:

$$\langle e^{-\beta(w-\Delta F)}\rangle = \gamma \tag{2.20}$$

γ measures the deviation from the Jarzynski equality induced by the feedback control. It can be expressed by considering the backward process. With feedback control the process is driven by a parameter $\lambda(t, y)$ which depends on the outcome of the measurement y for $t > t_m$, where t_m is the time at which the measurement is performed. The reversed process is then driven by $\lambda^\dagger(t, y) = \lambda(t_f - t, y)$.

Since in the reversed process the protocol depends on y from $t = 0$ to $t = t_f - t_m$, and the measurement is performed at $t = t_f - t_m$, it is impossible to perform a feedback due to causality. The protocol $\lambda^\dagger(t, y)$ has to be chosen before hand. It is then possible to measure $P^R[y'|\lambda^\dagger(t, y)]$, the probability of measuring the outcome y' in the backward process while imposing the protocol associated with the outcome y in the forward process. Since no feedback is performed in the reverse process, it is perfectly possible to obtain $y' \neq y$. Then $P^R[y|\lambda^\dagger(t, y)]$ can be different from 1.

Sagawa and Ueda linked γ to the probabilities $P[y'|\lambda^\dagger(t, y)]$ as:

$$\gamma = \int dy P^R[y|\lambda^\dagger(t, y)] \tag{2.21}$$

The result from eq. 2.18 generalises the Jarzynski equality in a simple way, but the definition of I can be hard to work with experimentally. Indeed, it relies on the knowledge of the joint distribution for y, the outcome of the measurement, and Γ the exact configuration of the system in the phase space which is not accessible experimentally. Furthermore, in the case of a noiseless measurement, the mutual information diverges and eq. 2.18 reverts to the standard Jarzynski equality from eq. 2.14.

The second result from eq. 2.20 relies only on the outcome of measurements in the reversed process and is accessible experimentally if the backward process can be done. This bypasses the need to know the exact distribution $P(\Gamma)$ in the phase space.

This second relation was tested experimentally by Toyabe et al. [52]. Using a dimer particle and a rotating electric field, they were able to realise an experiment in which they achieve work extraction by using a feedback protocol. They measure γ and check the validity of eq. 2.20.

2.3.3 Unavailable Information

While eq. 2.18 extends the Jarzynski equality by taking into account the information measured from the system, it doesn't take into account the properties of the feedback using this information. Ashida et al. proposed another extension of the Jarzynski equality. They define

an unavailable information I_u that is the information measured that isn't used by the feedback and is therefore lost. Their generalisation of the Jarzynski equality is the following:

$$\langle e^{-\beta w - I + I_u} \rangle = e^{-\Delta F} \tag{2.22}$$

where I is the information and I_u the unavailable information.

The definition of I used here is different from the one used in 2.18. Here, the information is taken as Shannon information, defined for each measurement outcome y as $I(y) = -\log(P(y))$. I_u is the unavailable information, defined for each measurement outcome y using the reverse protocol. If y' is the measurement outcome obtained when performing a protocol $\lambda^\dagger(t, y)$, the unavailable information is defined as:

$$I_u(y) = -\log\big(P^R(y' = y)\big) \tag{2.23}$$

$$= -\log\big(P^R(y|\lambda^\dagger(t, y))\big) \tag{2.24}$$

This definition is very similar to the one proposed by Sagawa and Ueda for γ in eq.2.20. The unavailable information measures the probability of obtaining a trajectory in the reverse protocol for which the measurement outcome matches the applied protocol.

$$\langle w \rangle > \Delta F - \langle I - I_u \rangle \tag{2.25}$$

This result, as well as the one from eq.2.20, relies only on the knowledge of the measurement outcome and can be tested experimentally. This is what we do in the following.

2.4 Conclusions

In this introductory chapter we presented all the main physical and mathematical results we use to analyse our experiments. The Langevin equation is a fundamental model that we will apply to different scenarios to extract useful thermodynamic quantities such as heat and work. The fluctuation theorems provide powerful tools to test the validity of our experimental setup and data analysis. We introduced the notion of information that allows us to generalise stochastic thermodynamics results to the case of feedback protocols. All these tools will be useful in the following chapters to analyse and interpret experimental data.

Chapter 3

Experimental Setup for Stochastic Thermodynamics

In this chapter, we present how micro-cantilevers and fast operating electronics are used to build an easy to tune and operate system for experimental stochastic thermodynamics. We use a micro-cantilever which behaves as an oscillator to model the dynamics of a 1D underdamped brownian particle. Arbitrary potentials and forces can be applied to the cantilever, thanks to a feedback loop with a short delay compared to the period of the oscillator.

To study experimentally stochastic thermodynamics, we need a system:

- With few degrees of freedom
- subject to thermal noise
- whose degrees of freedom can be measured with high accuracy
- on which we can apply a controlled external forcing

A good candidate, fulfilling these criterion are micro-cantilevers. The interesting degree of freedom is the deflection, subject to thermal noise. The scale of the fluctuations is small, typically less than a nanometer. However, micro-cantilevers are often used as probes for atomic force microscopy, and techniques have been developed to measure the deflection with high accuracy, as well as apply external forces on the cantilever.

3.1 Micro-cantilever: A 1D brownian particle

Our experimental system is a micro-cantilever from Micromotive (Octosensis 1000S). The cantilevers are typically 1 mm long, 90 µm wide and 1 µm thick and are made of silicon. A SEM picture from the manufacturer is shown in figure 3.1a. The interesting degree of freedom for our experiments is the vertical displacement of a point along the cantilever, the deflection x. Under thermal fluctuations, the deflection has a standard deviation $\sigma_x \simeq 0.8\,\mathrm{nm}$. This deflection is measured through interferometry, using an phase quadrature interferometric setup developed earlier in the group [53, 54]. A laser beam is split in two coherent measurement beams. One focused on the base of the cantilever acts as a reference, while the second one, focused on a point near the tip of the cantilever, acquires a phase shift $\phi = 4\pi\frac{x}{\lambda}$, where $\lambda = 632.8\,\mathrm{nm}$ is the wavelength of the He-Ne laser used. The two beams are recombined and analysed using two pairs of photodiodes from which signals the deflection x can be computed. The interest of the specific interferometric setup used is its accuracy up to the pm combined to a bandwidth up to 1 MHz. These high resolutions both in time and space allow us to measure precisely the thermal fluctuations of the cantilever.

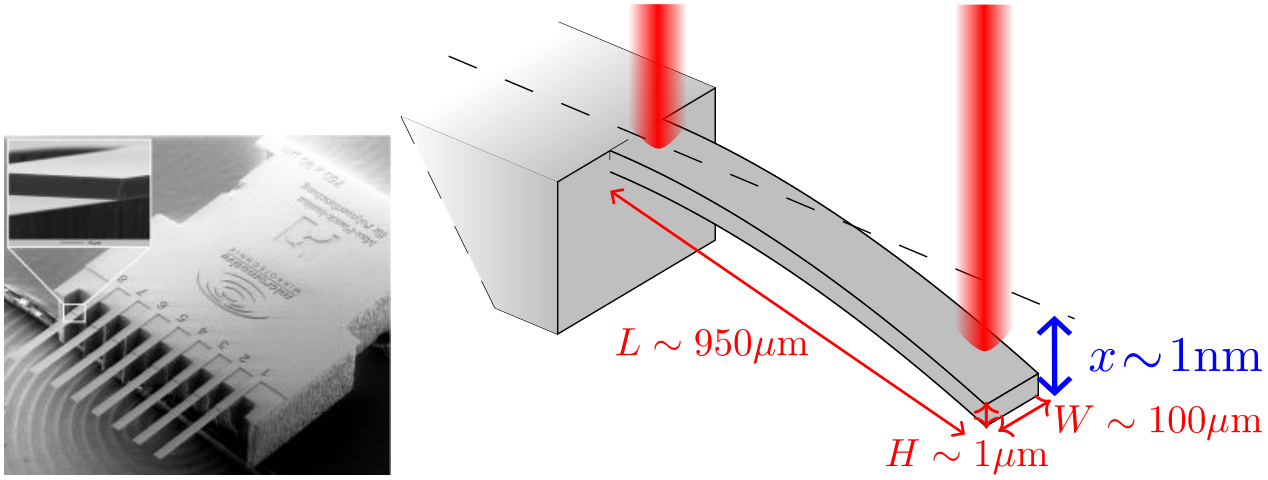

(a) SEM image of the cantilevers used, from the manufacturer. One chip holds 8 cantilevers, but only one at a time is used to perform the experiment.

(b) Sketch of the cantilever, with typical dimensions. Two laser beams (in red) are used to perform an interferometric measurement of x.

Figure 3.1: A model for a 1D Brownian particle: a micro-cantilever.

Micro-cantilevers are resonant objects. The ones used here have a fundamental resonant frequency $\frac{\omega_0}{2\pi} = f_0 \simeq 1100\,\text{Hz}$ and a quality factor $Q \simeq 8$ in air. Figure 3.2 shows the measured deflection x in time. Due to the resonant nature of the cantilevers, the signal has a strong oscillating component with fluctuations from thermal noise. However, if we look at the power spectrum of this signal in figure 3.3, several peaks at higher frequencies are present. These correspond to higher order flexural or torsional modes. In order to have a simple system to study, the first mode needs to be isolated.

The different modes have nodes at different locations along the cantilever [55]. By positioning the measuring laser beam on the node of the second mode, its amplitude is lowered and it can be neglected. The third mode and higher have a lower amplitude and don't alter significantly the measurements. If needed, we can filter them out by applying a low-pass filter. The spectrum after cancelling the second mode is shown on figure 3.3.

The dynamics of the deflection under thermal noise can be modelled by a Langevin equation for a simple harmonic oscillator (SHO):

$$m\ddot{x} + \gamma\dot{x} + kx = \sqrt{2k_BT\gamma}\xi(t), \tag{3.1}$$

where m is an effective mass, γ an effective viscosity, k the stiffness of the cantilever, k_B is the Boltzmann constant, T the temperature and ξ a gaussian white noise satisfying $\langle\xi\rangle = 0$ and $\langle\xi(t)\xi(t+\tau)\rangle = \delta(\tau)$. This equation can be written as:

$$\ddot{x} + \frac{\omega_0}{Q}\dot{x} + \omega^2 x = \sqrt{\frac{2k_BT\omega_0}{Qm}}\xi(t). \tag{3.2}$$

The deflection behaves as the position of a 1D brownian particle in a harmonic potential, under thermal noise. Since the cantilever has a quality factor $Q \simeq 8$, the oscillator is underdamped.

The different parameters for the model can be extracted from the power spectrum of the deflection using the fluctuation-dissipation theorem [55]. This theorem states that the spectrum

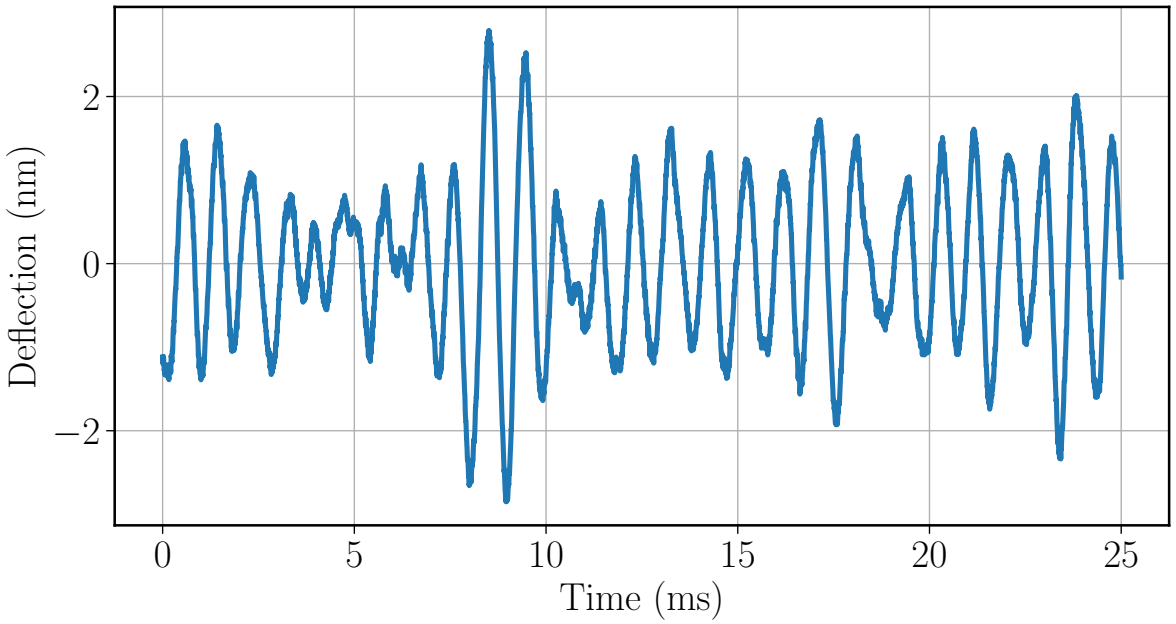

Figure 3.2: Deflection of the free cantilever in time. The signal is dominated by oscillations at a frequency around 1100 Hz, characteristic of the resonant nature of the cantilever. These oscillations are driven randomly by the thermal noise, which creates the noisy aspect of the signal.

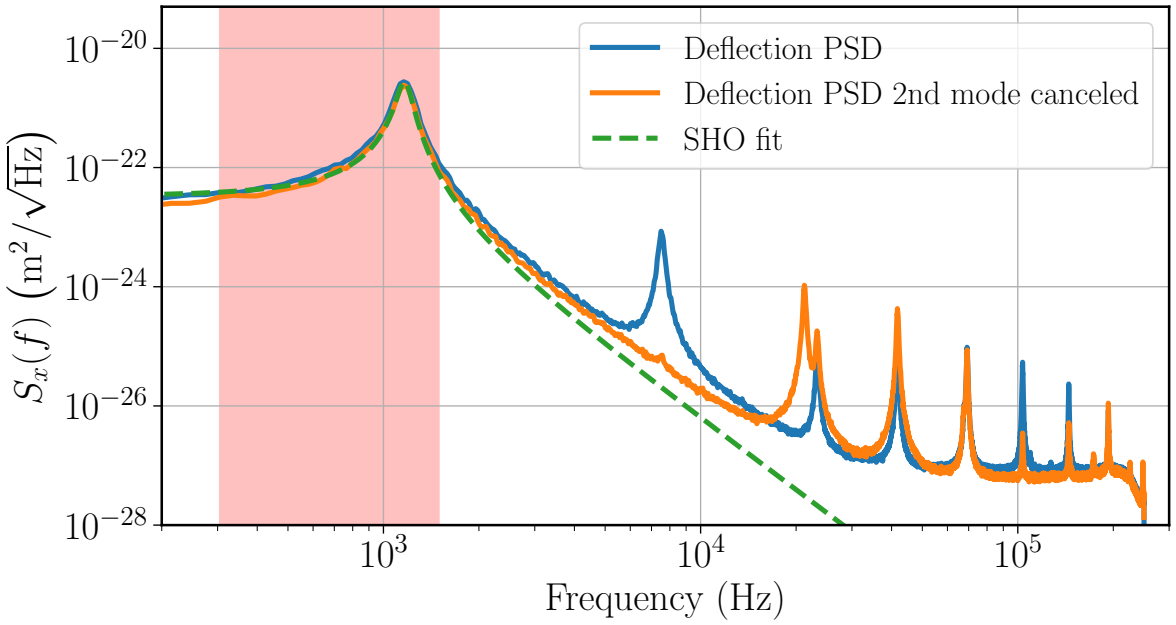

Figure 3.3: Blue: Power Spectrum Density of the deflection of the cantilever. Each peak corresponds to a different mode. Orange: PSD of the deflection with second mode cancellation: the peak of the second mode around 7500 Hz has a negligible amplitude. Both spectrum are measured on unfiltered deflection signal, acquired at 500 kHz. Green: Fit of the SHO model using a fit window centered on the first mode (red shaded area).

of the deflection under thermal noise is

$$S_x(\omega) = \frac{2k_BT}{\pi\omega}\,\mathrm{Im}\left(\frac{1}{H(\omega)}\right), \tag{3.3}$$

with $H(\omega) = -m\omega^2 + i\gamma\omega + k$ the mechanical response function of the cantilever. This gives:

$$S_x(\omega) = \frac{4k_BT}{\omega_0 k}\frac{1/Q}{((1-(\frac{\omega}{\omega_0})^2)^2 + (\frac{\omega}{Q\omega_0})^2} \tag{3.4}$$

By fitting the power spectrum from figure 3.3, we can extract the values of the parameters k, ω_0, Q, of the SHO model of equation 3.2. We typically find $k = 7\times10^{-3}\,\mathrm{N\,m^{-1}}$, $Q = 8$ and $\omega_0 = \frac{1100}{2\pi}\mathrm{rad\,s^{-1}}$.

We apply the formalism of the Langevin equation to describe our system. It gives us access to the mechanical parameters of our oscillator, needed to build a feedback loop.

3.2 Controlled force

The feedback control is done by tuning an electrostatic force between the cantilever and a counter-electrode. We introduce a bias voltage to linearise the force and achieve a simpler feedback.

The cantilever is conductive (gold coated) and faces a metallic plate (figure 3.4). This forms a capacitor, with capacity C that depends on the distance z between the cantilever and the plane. z can be decomposed as $z = h + x$ with h the distance between the plane and the cantilever at rest. If a voltage V is applied between the cantilever and the plane, there is an energy $E_c = \frac{1}{2}CV^2$ stored in the capacitor, resulting in a force $F = -\partial_x E_c = \frac{1}{2}\partial_x C|_z V^2$. This force is proportional to V^2 with a prefactor $\alpha(z) = \frac{1}{2}\partial_x C|_z$. Considering $h \gg x$ we can assume $\alpha(z) \simeq \alpha(h)$ to be constant in our experiments.

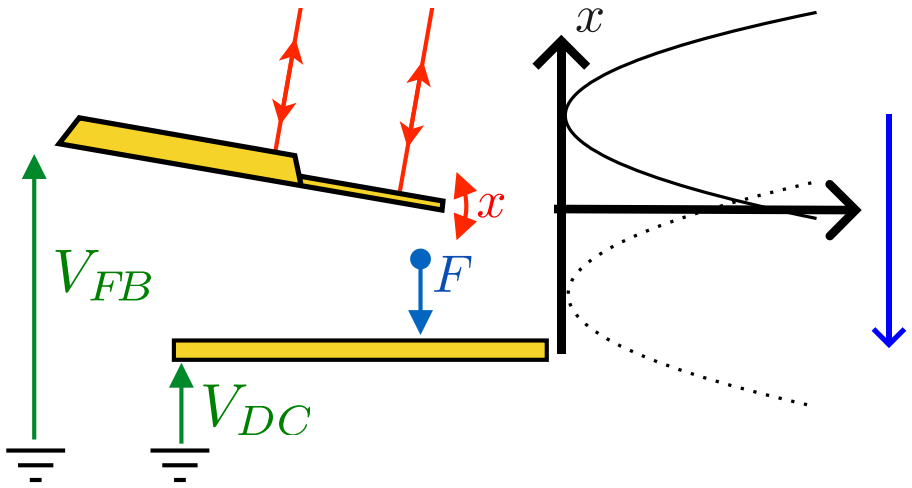

Figure 3.4: The capacitor formed by the cantilever and the metallic plane. A force $F \propto (V_{FB} + V_{DC})^2$ pulls on the cantilever, shifting the harmonic potential created by the natural stiffness of the cantilever.

This force is always attractive and has a dependency on the square of the applied voltage. It is more interesting to have a feedback linear in the applied voltage, with a force that can be both attractive and repulsive. To achieve this, a strong DC bias V_{DC} is applied to the system

on top of a smaller control voltage V_{FB}. Doing so the total force is:

$$F_{tot} = \alpha(V_{FB} + V_{DC})^2 \tag{3.5}$$
$$= \alpha(V_{DC}^2 + 2V_{FB}V_{DC} + V_{FB}^2) \tag{3.6}$$
$$\tag{3.7}$$

Typically $V_{DC} = 90\,\mathrm{V}$, $V_{FB} \simeq 1\,\mathrm{V}$ and $V_{FB} \ll V_{DC}$. The leading term in V_{DC}^2 is constant throughout the experiment and correspond to a shift of the equilibrium position of the cantilever that can be absorbed in the definition of $x = 0$. Since $2V_{FB}V_{DC} \gg V_{FB}^2$, the last term can be neglected. This leads to a force linear in V_{FB}:

$$F = 2\alpha(h) \times V_{DC}V_{FB} \tag{3.8}$$

Changing the applied bias V_{DC} or the distance between the cantilever and the surface h gives two ways to set the sensitivity of the system in the desired range. The proportionality constant is measured through a calibration step. The voltage V_{FB} is swept from $-1\,\mathrm{V}$ to $1\,\mathrm{V}$, by step of typically $0.33\,\mathrm{V}$. An example of calibration data is shown on figure 3.5. The sweep in V_{FB} is done first from $-1\,\mathrm{V}$ to $1\,\mathrm{V}$ and then in reverse in order to cancel effects from drifts in time. For each step the deflection of the cantilever is measured for $0.5\,\mathrm{s}$ and the average deflection $\langle x \rangle$ is computed. Since on average $\langle x \rangle = \frac{F}{k} = a \times V_{FB}$, a linear fit of $\langle x \rangle$ as a function of V_{FB} gives the slope $a \simeq 8.3\,\mathrm{nm\,V^{-1}}$.

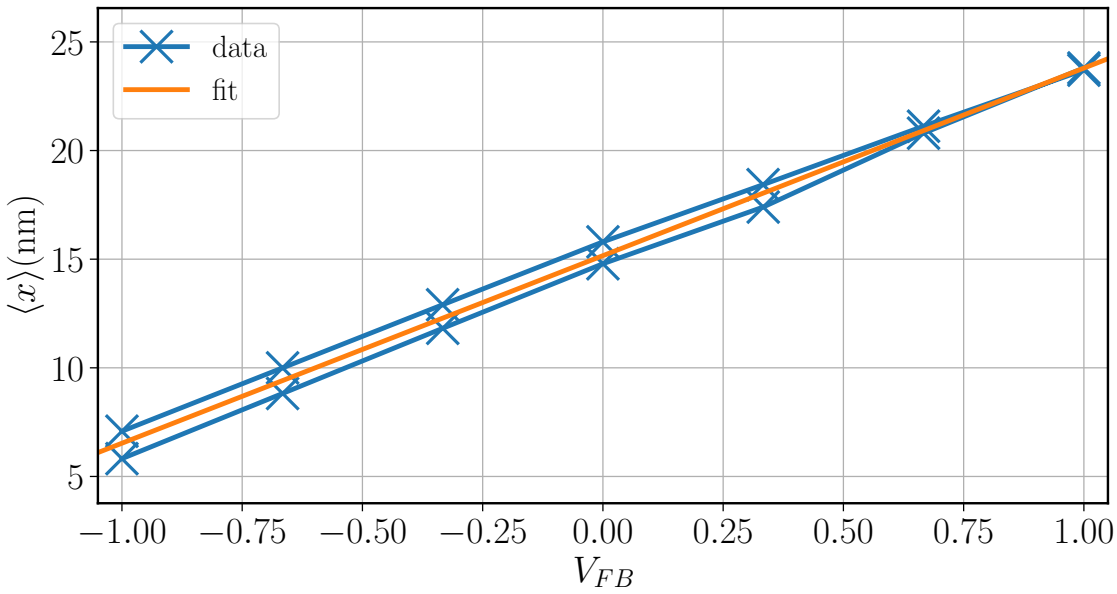

Figure 3.5: The mean deflection $\langle x \rangle$ as a function of the applied voltage V_{FB}. Blue: Experimental points, taken over $0.5\,\mathrm{s}$ each. Orange: Linear fit of the data, giving a slope $a = 8.3\,\mathrm{nm\,V^{-1}}$.

To conclude, we have a way to apply a controlled and calibrated force on the cantilever. This force is proportional to the control voltage V_{FB} and easy to pilot.

3.3 Feedback device

To generate the feedback voltage V_{FB} as a function of the deflection x in real-time, we need a device able to perform computations at high frequency. We use a National Instrument Field Programmable Gate Array (FPGA) card, clocked at $100\,\mathrm{MHz}$. This card can be programmed

to compute the deflection, apply filters, and output the feedback voltage $V_{FB}(x)$. The card is operated from a computer, used to program the feedback, record data, and start or stop experiments. The function $V_{FB}(x)$ is coded by the user and can be complex enough to create arbitrary feedbacks on the system, without any change in the experimental setup.

The deflection x is computed from the signals of the interferometer. To eliminate high frequency noises and the contribution of higher order modes, the deflection needs to be filtered. To be able to operate the feedback, the filtering needs to be done in real-time. Standard Fourier filtering cannot be used here: Fourier filtering can only be done on whole time series and is not causal. We instead use Infinite Impulse Response filters (IIR). These filters work by using the previous outputs as well as previous inputs to filter the signal. The n-th output of the filter $x_{out}[n]$ can be computed as:

$$x_{out}[n] = \sum_{k=0}^{+\infty} a_k x_{in}[n-k] + \sum_{k=1}^{+\infty} b_k x_{out}[n-k] \tag{3.9}$$

where $x_{in}[n]$ is the n-th input of the filter and a_k, b_k are series of coefficients that determines the nature of the filter. In practice, we use a 3rd order low-pass Butterworth filter at 50 kHz.

The whole process of digitalising the photodiodes signals (ADC), computing the deflection, filtering it, computing the output voltage V_{FB}, and converting it to an analog voltage output (DAC), takes time and induces a latency in the feedback of $\tau_{FB} \simeq 1\,\mu s$. This results in a feedback $V_{FB}(x_{FB})$, computed on a position $x_{FB}(t) = x(t - \tau_{FB})$ delayed with respect to the ideal one $x(t)$. To compensate for this latency and increase the accuracy of the feedback, we add a correction proportional to the speed of the particle to anticipate its future position. In practice, we modify the low-pass filter. We call $BW(\omega)$ the transfer function of the Butterworth filter in the Fourier space. We apply a filtering $(1 + i\omega\tau_{corr})BW(\omega)$ with an anticipation time τ_{corr} that has to be optimised to be as close as possible from τ_{FB} (fig 3.6).

$$x_{FB} = x(t - \tau_{FB}) + \dot{x}(t - \tau_{FB}) \times \tau_{corr} \tag{3.10}$$
$$\simeq x(t) + \dot{x}(t) \times (\tau_{FB} - \tau_{corr}) \tag{3.11}$$

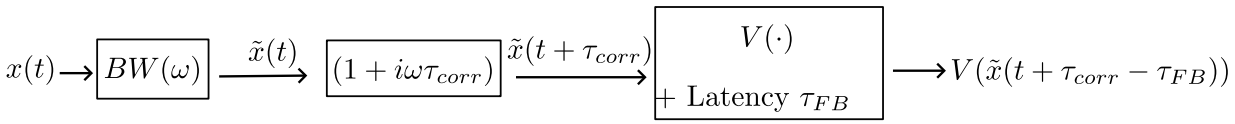

Figure 3.6: The filtering process used on the FPGA card.

If τ_{corr} is set to a value close from τ_{FB}, the feedback voltage is $V_{FB}(x)$ and the latency of the feedback loop is compensated. The value of τ_{corr} has been optimised previously in the group [56] and is set to 1.26 µs.

Since the function $V_{FB}(x)$ driving the feedback force can be easily changed in the software, the setup is highly versatile and allows us to perform different kinds of experiments without any change on the experimental conditions. This brings a good stability of the experiment and reproducibility.

The complete feedback loop results in a system that can be described by a Langevin equation with an external force $F_{FB}(x,t)$ arbitrarily defined by the operator:

$$\ddot{x} + \frac{\omega_0}{Q}\dot{x} + \omega^2 x = \sqrt{\frac{2k_B T\omega_0}{Qm}}\xi(t) + \frac{\omega_0^2}{k}F_{FB}(x,t) \tag{3.12}$$

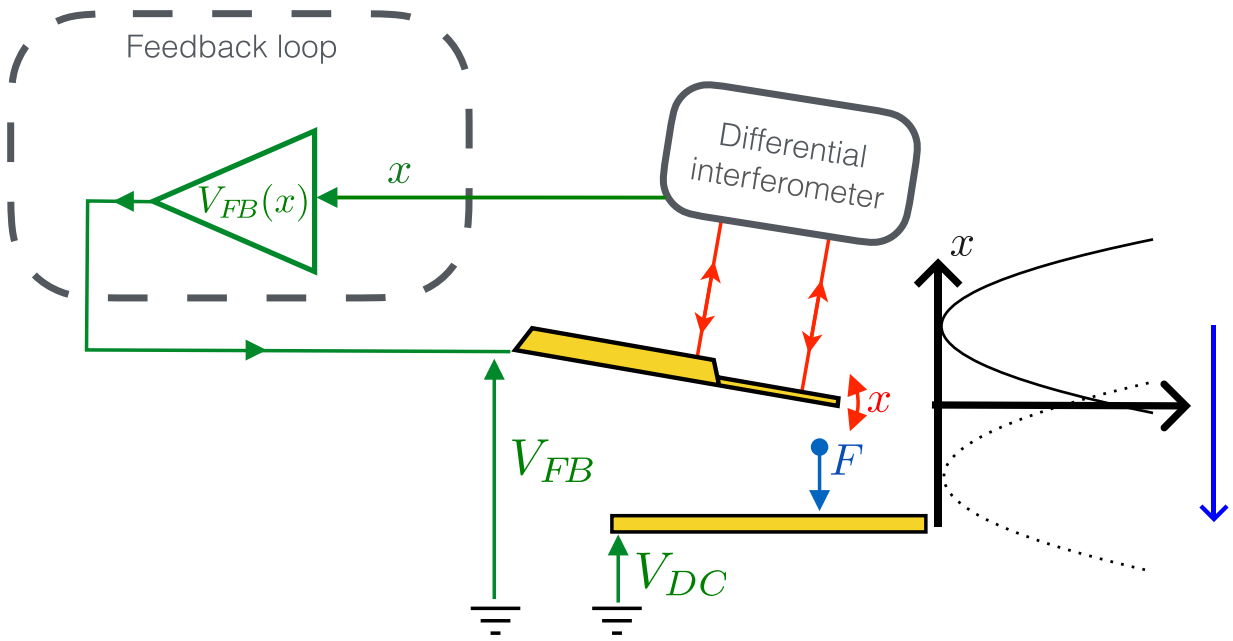

Figure 3.7: The complete feedback loop.

The adaptability of the feedback allows for a lot of different experiments without any change to the hardware used. By changing the program on the FPGA card, we can control arbitrarily the force F_{FB}.

3.4 Thermodynamics quantities

In stochastic thermodynamics, we want to study the energy exchange between the particle, the heat bath, and the operator. We need to be able to reconstruct the thermodynamic quantities U, w and q, introduced in chapter 2, from x and V_{FB} that we measure experimentally.

The energy of a 1D system E can be expressed as a $E = K + U$ where $K = \frac{1}{2}m\dot{x}^2$ is a kinetic term and $U(x, \lambda)$ is a potential energy depending on the position of the particle x, and an external control parameter λ. In our experiments, U is of the form $U(x) = \frac{1}{2}k(x - x_0)^2$. By applying a constant voltage V_{FB}, we can shift the harmonic well center x_0. In chapter 4, we show that we can also tune k using our feedback loop. In practice, λ can be x_0 or the effective stiffness k felt by the cantilever.

Using the definition from 2.1.2, we have:

$$\dot{q} = \frac{\partial(K+U)}{\partial x}\dot{x} + \frac{\partial(K+U)}{\partial \dot{x}}\ddot{x} \tag{3.13}$$

$$= k(x - x_0)\dot{x} + m\dot{x}\ddot{x} \tag{3.14}$$

$$\tag{3.15}$$

For $\dot{w}$, the exact expression depends on the actual parameter represented by lambda. We can generally write:

$$\dot{w} = \partial_k U\dot{k} + \partial_{x_0} U\dot{x_0} \tag{3.16}$$

$$= \frac{1}{2}(x - x_0)^2\dot{k} - k(x - x_0)\dot{x_0} \tag{3.17}$$

Using these expressions we can compute the instantaneous heat, $\dot{q} = \frac{dq}{dt}$, and work, $\dot{w} = \frac{dw}{dt}$, from the experimental measurement of x.

Figure 3.8 shows an example of an experiment where the control parameter x_0 is switched from $-L$ to $+L$ at $t = 0$. We see on the top figure that when x_0 is shifted the value around which the deflection x oscillates follows. The bottom figure shows the instantaneous fluxes $\dot{q}$ and $\dot{w}$. Whereas the heat flux fluctuates due to thermal fluctuations throughout the whole experiment, the work is non zero only when the control parameter x_0 is switched at $t = 0$.

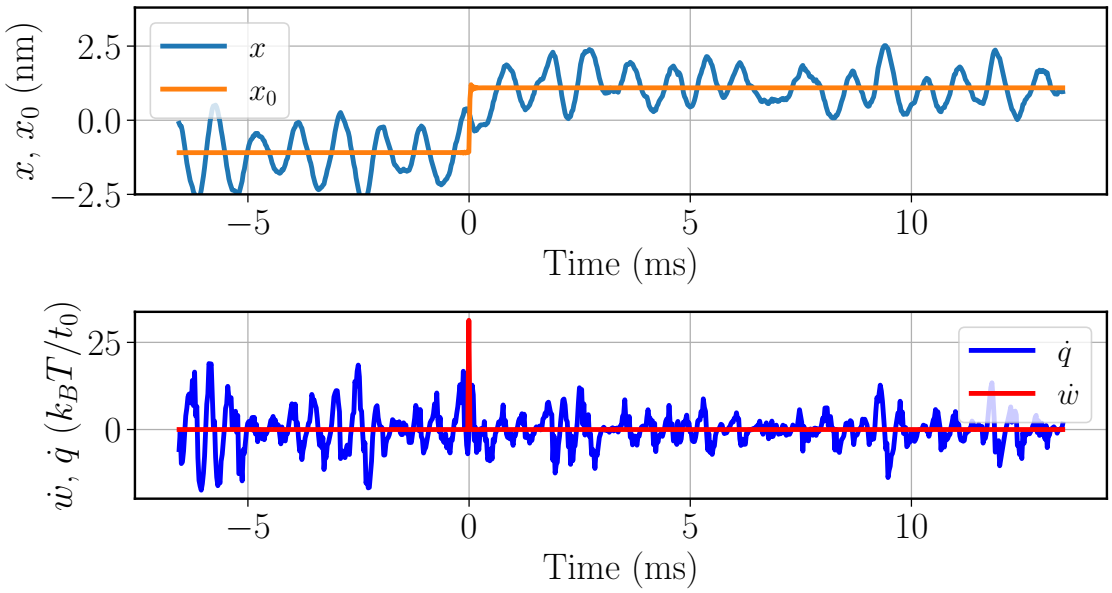

Figure 3.8: Top: Deflection of the cantilever x and control parameter x_0 (position of the center of the trapping potential) during an experiment where x_0 is shifted from $-L$ to $+L$ at $t = 0$. Bottom: $\dot{w}$, $\dot{q}$, the instantaneous work and heat flux during the experiment. $\dot{q}$ fluctuates throughout the whole experiment, whereas $\dot{w} \neq 0$ only when the potential is shifted.

This is a powerful tool that allows us to measure both heat and work during any kind of experiment.

Using the formalism introduced in 2.1.2, we are able to obtain expressions for w and q that can be used to reconstruct these quantities from our experimental measurements of x and V_{FB}. From the measure of the deflection of the cantilever, we are able to reconstruct the whole thermodynamics of the process.

3.5 Conclusions

In this chapter, we presented a very flexible feedback loop to be used for stochastic thermodynamic experiments. This setup is built on an interferometric setup providing the resolution needed to measure thermal fluctuations and reconstruct the thermodynamic quantities of interest. It can be controlled using an electrostatic force with or without feedback. We have an easy way of changing the feedback to perform different kinds of experiments. We seize the flexibility of the setup in the following by changing artificially the stiffness of the cantilever, building information engines, or a Maxwell Demon.

Chapter 4

Tuning of the harmonic potential

A landmark tool in stochastic thermodynamics is the ability to tune the stiffness of the trapping potential. This allows to perform the equivalent of a macroscopic compression on the system. In this chapter, we present how the feedback loop can be used to create an artificial stiffness on the cantilever.

Modifying the stiffness can be easily achieved in optical tweezers by tuning the power of the trapping laser. For a micro-cantilever, since the stiffness is determined by the Young modulus of silicon and the dimensions of the cantilever, there is not such an easy way to tune the stiffness k.

Our idea is to apply a feedback engineered to mimic an additional stiffness acting on the particle. These results were obtained during Emile Cochin's internship that I supervised during two months in summer 2022.

4.1 Experimental tuning of the stiffness

To change the stiffness of the cantilever, we set the feedback so the output voltage $V_{FB} \propto x$. This results in a force $F = -k_1 x$. The resulting Langevin equation is then :

$$m\ddot{x} + \gamma\dot{x} + kx = -k_1 x + \sqrt{2k_B T\gamma}\xi(t) \tag{4.1}$$

$$m\ddot{x} + \gamma\dot{x} + (k + k_1)x = \sqrt{2k_B T\gamma}\xi(t) \tag{4.2}$$

k_1 acts as an additional stiffness that can be tuned by the user. We define λ, a dimensionless control parameter for the stiffness as $\lambda = \frac{k+k_1}{k}$. A target value for λ is chosen in the software and we want to check if the particle behaves accordingly by measuring the effective stiffness λ_{eff}. At equilibrium in a potential $U(x)$, the position of the particle follows a Boltzmann distribution:

$$P(x) = \frac{1}{Z} e^{-\beta U(x)} \tag{4.3}$$

with Z the partition function and $\beta = \frac{1}{k_B T}$ the inverse temperature. We can recover the effective potential felt by the particle from the measurement of $P(x)$ as:

$$\beta U(x) = -\log(P(x)) + C \tag{4.4}$$

where $C = \log(Z)$ is a constant absorbed in the definition of the zero of the potential. Figure 4.1 shows the potential measured experimentally in the case without feedback ($\lambda = 1$). Since in this case $U(x) = \frac{1}{2}kx^2$, we can extract the value of k from a parabolic fit of the potential (red curve on figure 4.1). $P(x)$ is measured from an acquisition of 0.5 s, very long compared to the relaxation time of the particle. The obtained value is $k = 5.67 \times 10^{-3}\,\mathrm{N\,m^{-1}}$.

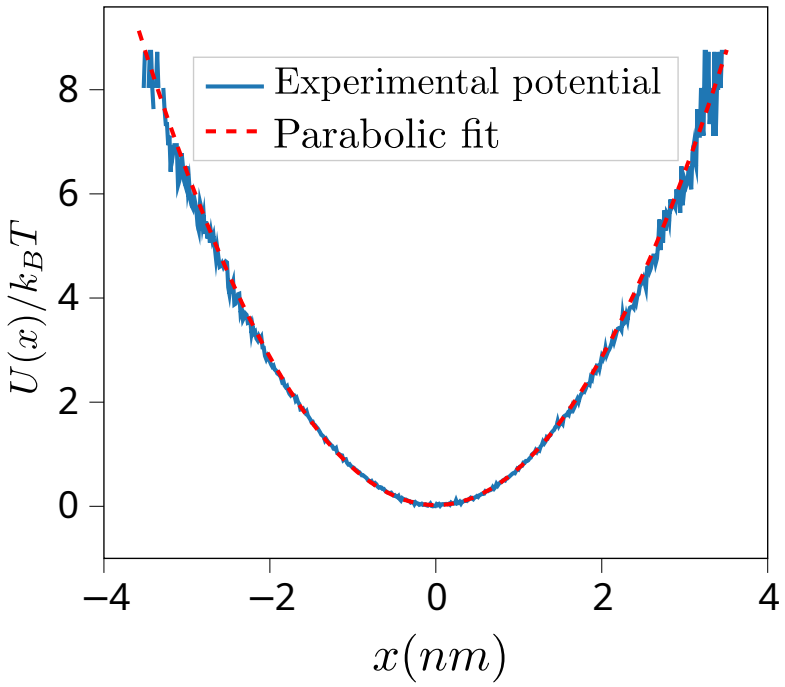

Figure 4.1: Potential measured as $U(x) = -\log(P(x))$, in the case $\lambda = 1$ (no feedback). In blue, experimental data. In red, a parabolic fit. The parabolic fit gives a stiffness $k = 5.67 \times 10^{-3}\,\mathrm{N\,m^{-1}}$

We can now check the obtained potential in the case with feedback. Figure 4.2 shows the different potentials reconstructed from experiments with different values of the target λ. As λ increases, the potential gets narrower, which corresponds to an increase in the effective stiffness and a compression of the system. To compute λ, we use the equipartition theorem for the distribution of speeds, as well as the distribution of positions. The equipartition theorem states that at equilibrium:

$$\frac{1}{2}k_BT = \frac{1}{2}\lambda_{\text{eff}}k\langle x^2\rangle = \frac{1}{2}m\langle v^2\rangle \tag{4.5}$$

hence, using the last equality:

$$\lambda_{\text{eff}} = \frac{\langle v^2\rangle}{\omega_0^2\langle x^2\rangle} \tag{4.6}$$

with $\omega_0 = \sqrt{\frac{k}{m}}$ the natural angular resonance frequency of the oscillator.

The resulting λ_{eff} as a function of λ can be seen on figure 4.2. We see that $\lambda_{\text{eff}} = \lambda$, meaning that the feedback acts correctly and that we can tune the stiffness of the system. Note that we can access values of λ lesser than 1. This means that the feedback allows us to reduce the stiffness of the system as well as increase it.

However, changing the potential $U(x)$ should not change the distribution of speeds. If we measure the variance of the speed $\sigma_v^2 = \langle v^2\rangle$ as a function of λ, we can access a kinetic temperature $T_K = m\frac{\langle v^2\rangle}{k_B}$ which is different than the temperature T of the thermal bath. Figure 4.3 shows the kinetic temperature as a function of λ. We normalise the kinetic temperature as T_K/T by taking the value to be 1 in absence of feedback ($\lambda = 1$). We see on the blue curve that the feedback lowers the effective temperature of the system. This can be explained by a delay in the feedback loop. If there is a latency τ_{FB}, then the force applied on the system is $F = -k_1x(t - \tau_{FB})$. The Langevin equation describing the system is now:

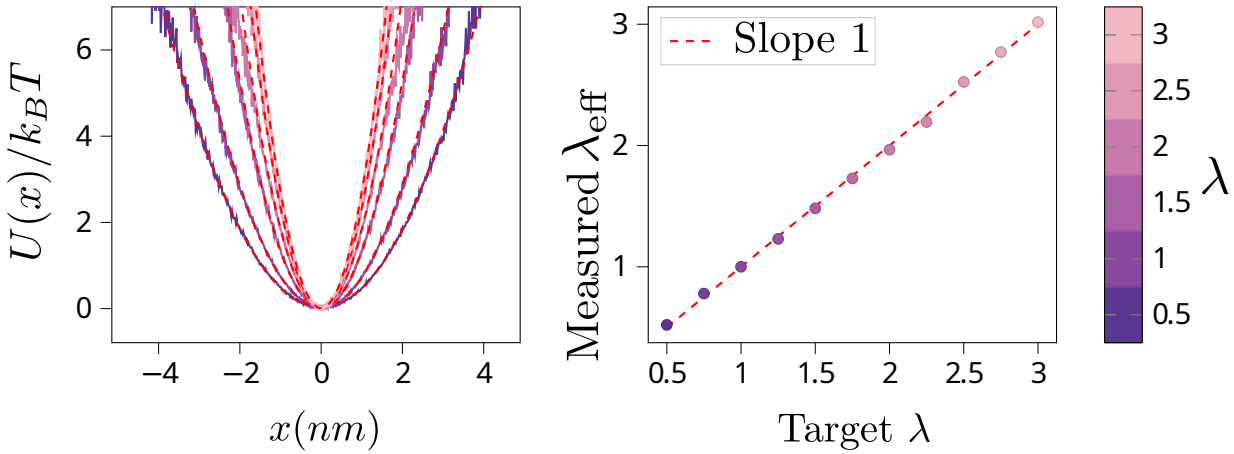

Figure 4.2: Left: Potential measured with feedback for different values of the target λ. As λ increases, the potential gets narrower, corresponding to an increase in the effective stiffness λ_{eff}. Dashed red lines are the best parabolic fits of the potentials. Right: λ_{eff} as a function of λ, measured using equipartition of energy. The points align perfectly on a line with slope 1, which means that the feedback operates as wished.

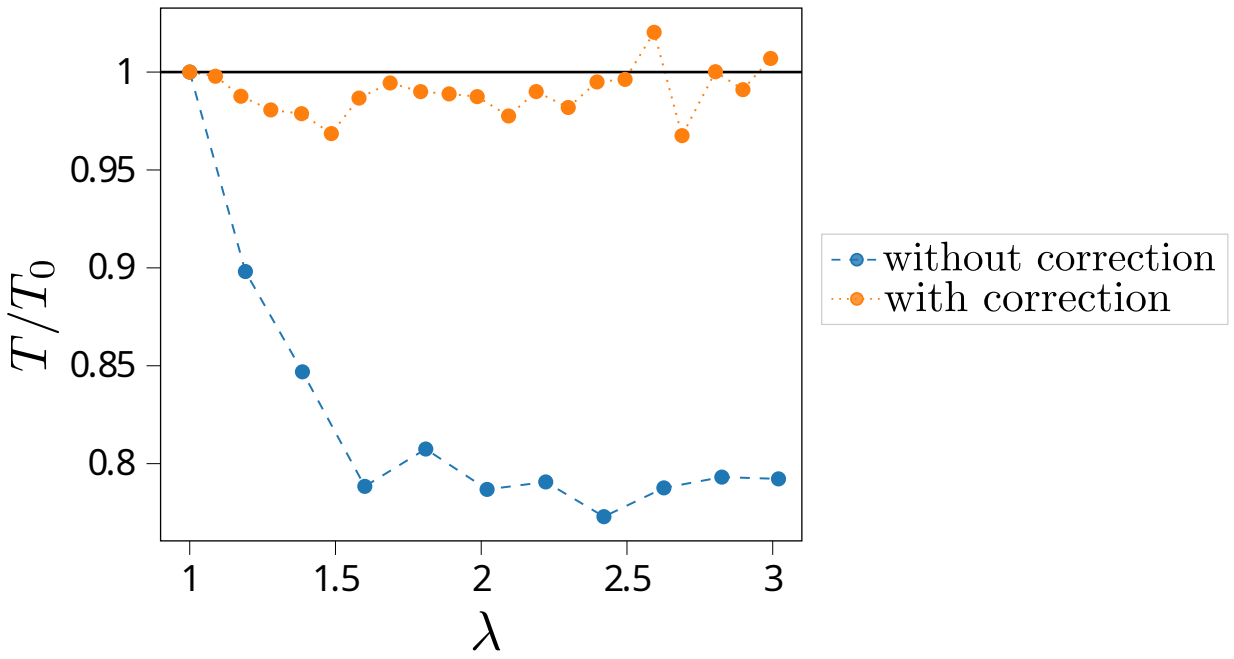

Figure 4.3: T_K/T as a function of λ. Blue: Experimental data without optimisation of τ_{corr}. We notice a huge variation of T_K/T, with a discrepancy up to 20%. Orange: Experimental data with optimisation of τ_{corr}. The discrepancy between T_K and T is at most 3%.

$$m\ddot{x} + \gamma\dot{x} + kx = -k_1 x(t - \tau_{FB}) + \sqrt{2k_B T\gamma}\xi(t) \tag{4.7}$$
$$m\ddot{x} + \gamma\dot{x} + kx = -k_1 x(t) + k_1\dot{x}(t)\tau_{FB} + \sqrt{2k_B T\gamma}\xi(t) \tag{4.8}$$
$$m\ddot{x} + (\gamma - k(\lambda - 1)\tau_{FB})\dot{x} + \lambda k x(t) = \sqrt{2k_B T\gamma}\xi(t) \tag{4.9}$$
$$m\ddot{x} + \gamma_{\text{eff}}\dot{x} + \lambda k x(t) = \sqrt{2k_B T_K \gamma_{\text{eff}}}\xi(t) \tag{4.10}$$
$$\tag{4.11}$$

where $\gamma_{\text{eff}} = \gamma - k(\lambda - 1)\tau_{FB}$ and $T_K = \frac{\gamma}{\gamma_{\text{eff}}}T$ are effective viscosity and temperature. The latency in the feedback acts as an additional viscosity that changes the distribution of speeds and $\langle v^2 \rangle$. This additional viscosity breaks the fluctuation-dissipation relation and results in a kinetic temperature T_K different from the bath temperature T.

The previous optimisation of the compensation of the latency, τ_{corr} (presented in section 3.3), was done on a different kind of experiment. Since the set of operations run by the FPGA card for this feedback is different, the latency τ_{FB} is different and τ_{corr} has to be optimised for this scenario. A set of experiments with different values of τ_{corr} were performed for different values of λ to find the optimal τ_{corr} minimizing the difference between T_K and T. The results of this optimisation is shown in figure 4.4. The striking result is that values of τ_{corr} are negative and much greater in absolute value than the previous optimum of $\tau_{corr} = 1.26\,\mu\text{s}$. We still don't have a convincing explanation for this.

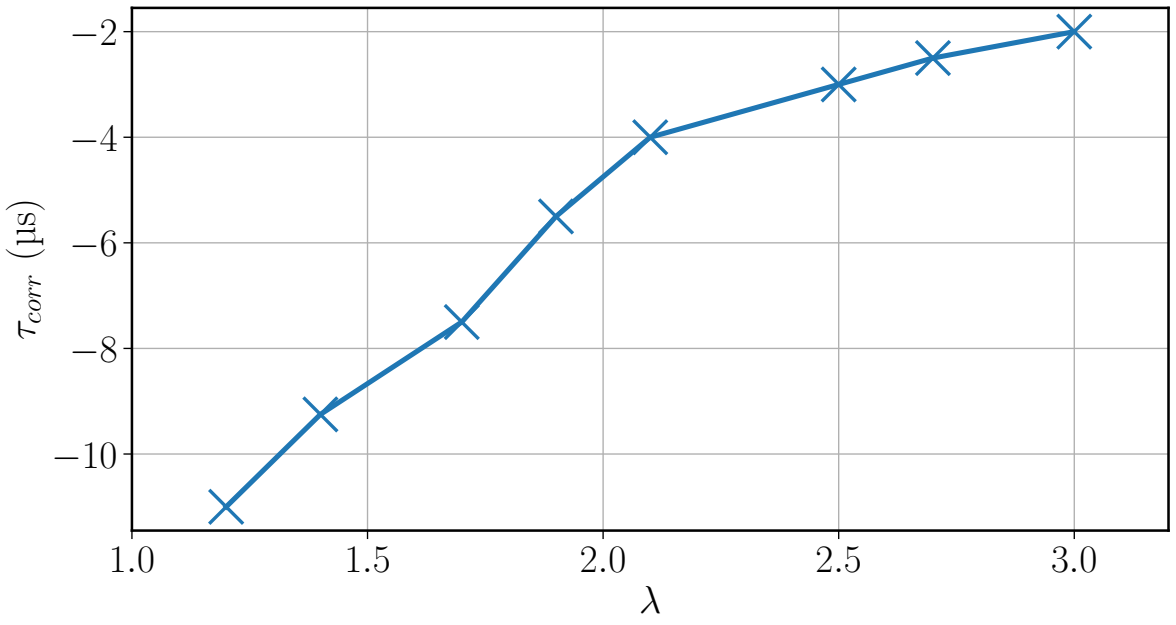

Figure 4.4: Optimal values of τ_{corr} as a function of λ. These values were obtained by trying many different values of τ_{corr} for each value of λ and choosing the one such that $T_K/T = 1$. Negative values of τ_{corr} means that the delay of the feedback loop has to be increased in order to match the bath temperature.

Despite the surprising result that $\tau_{corr} < 0$, by interpolating between these values, we can obtain an approximation for the optimal τ_{corr} for any value of λ, meaning that the stiffness can be tuned to any value within this range without affecting the kinetic temperature T_K. The orange curve on figure 4.3 shows the variation of T_K/T using this interpolation procedure. The discrepancy between T_K and T is much lower than previously, with an error of less than 3%.

This is a validation of our technique in the case of constant stiffness. We are able to tune the harmonic potential and recover the expected equilibrium properties, both for the distribution of position and speed.

4.2 Compression experiments

Now, we are interested in experiments where the stiffness is changed continuously. The stiffness is then described by $\lambda(t)$, with a time dependence, and the potential is $U(x,t) = \frac{1}{2}\lambda(t)kx^2$. For simplicity we only studied compression protocols with linear change in stiffness i.e. constant $\dot{\lambda}$, going from λ_i to λ_f. The protocols are performed at constant temperature, by adapting the value of τ_{corr} accordingly to the change in λ. We present two sets of experiments: a quasistatic one performed over 50ms with $\lambda_i = 1$ and $\lambda_f = 1.5$, and an out of equilibrium one performed over 5ms with $\lambda_i = 1$ and $\lambda_f = 3$. We focus on the fast one in this section.

We record 5000 realisations of the out of equilibrium protocol. Each realisation is 5 ms long, a timescale comparable to the relaxation time of the system, τ_{relax}. From these data we compute the joint probability $P(x, \dot{x}, t)$. The probability distribution is plotted in figure 4.5 for $t = 0$ (start of the protocol), $t = 2.5$ ms (middle of the protocol) and $t = 5$ ms (end of the protocol). The probability distribution is a bivariate Gaussian that gets narrower in the x direction, as expected from a compression. The distribution in v seems to be unchanged by the protocol and independent of x, we will therefore only consider the distribution of deflection $P(x,t)$ in the following.

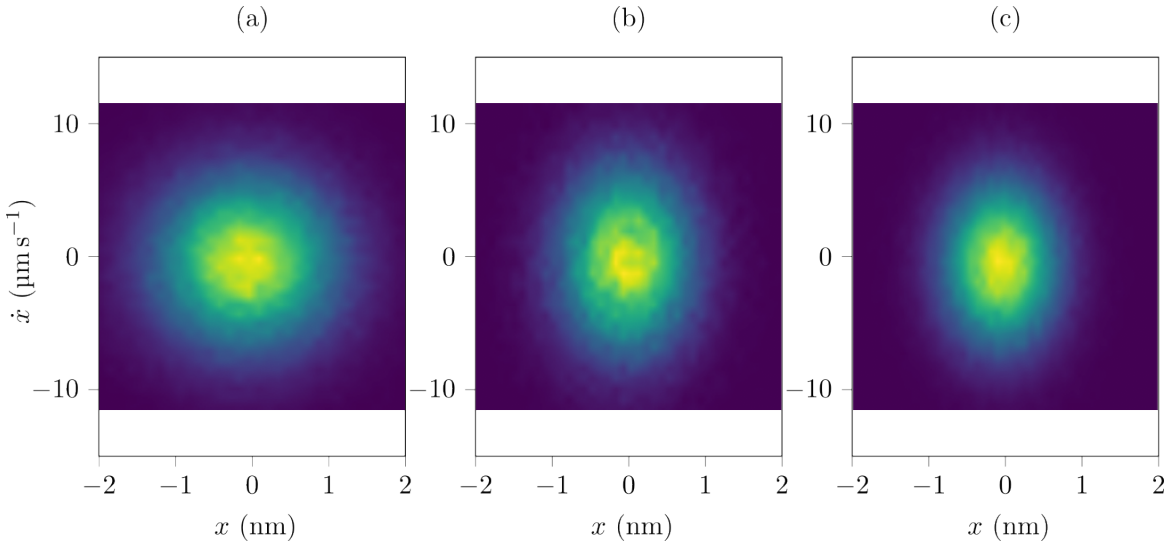

Figure 4.5: Probability distributions $P(x, \dot{x}, t)$ for the compression protocol. Measured at $t = 0$ (a.), $t = 2.5$ ms (b.), $t = 5$ ms (c.). The distributions are gaussian. Due to the compression, the distribution gets narrower in the x direction.

Since the distributions $P(x,t)$ are gaussian, we can characterise them by their variance σ_x^2, or by their inverse variance σ_x^{-2}. The inverse variance is interesting because at equilibrium, $\sigma_x^{-2} \propto \lambda$ (eq.4.5) and we can compare its variation to the imposed variation of stiffness. Figure 4.6 shows the evolution of σ_x^{-2} as a function of time during the compression experiment. At equilibrium $\sigma_x^{-2} k_B T/k = \lambda$. The protocol starts at $t = 0$ and ends at $t = 5$ ms. We can see that before the protocol ($t < 0$), we recover the natural stiffness of the cantilever, and that the final value for $t > 5$ ms is three times the initial value, which is coherent with $\lambda_i = 1$ and $\lambda_f = 3$.

We are able to change continuously the stiffness using our feedback. We recovered expected values for σ_x^{-2}, in agreement with the prescribed variation in λ and with the theoretical predic-

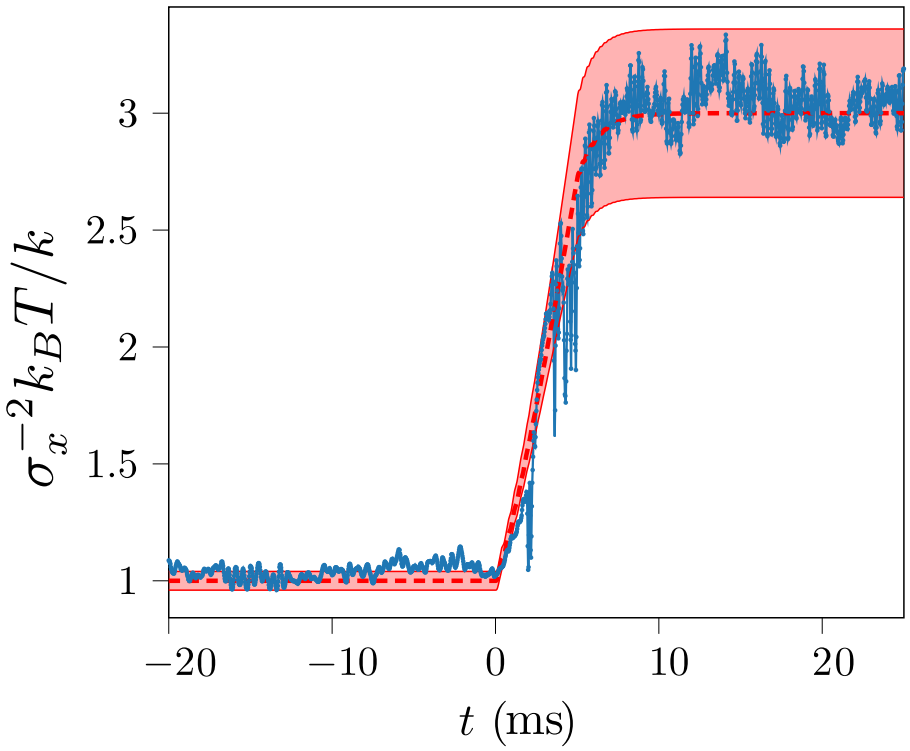

Figure 4.6: Evolution of σ_x^{-2} during the compression protocol. Blue: Experimental average over 5000 experiments. Red: theoretical prediction [57]. Red shade: statistical uncertainty. The protocol starts at $t = 0$ and ends at $t = 5\,\text{ms}$. The protocol goes from $\lambda = 1$ to $\lambda = 3$, in good agreement with the initial and final values of $\sigma_x^{-2} k_B T/k$.

tions from [57]. Another interesting aspect is the study of energy transfers in the form of heat and work during the process.

4.3 Work exchange during compressions

We can measure the amount of work exchanged with the system during the ramp of stiffness and compare it to standard theorems of stochastic thermodynamics like Crooks' relation.

In our protocol the rate of change in stiffness $\dot{\lambda}$ is constant. Using definitions from 3.4, the instantaneous work performed on the particle is:

$$\dot{w} = \frac{\partial U}{\partial \lambda}\dot{\lambda} \tag{4.12}$$

$$= \frac{\partial}{\partial \lambda}\left(\frac{1}{2}\lambda k x^2\right)\dot{\lambda} \tag{4.13}$$

$$= \frac{1}{2}\dot{\lambda} k x^2 \tag{4.14}$$

We can integrate $\dot{w}$ over a realisation to obtain the total work, w, exchanged during a protocol:

$$w = \int \dot{w}(t)dt = \int \frac{1}{2}\dot{\lambda} k x(t)^2 dt = \frac{1}{2}\dot{\lambda} k \int x(t)^2 dt \tag{4.15}$$

The value of w is accessible experimentally by integrating $x(t)^2$ over a ramp of stiffness, $\dot{\lambda}$ and k being known. We apply this result to two different compression experiments, one in the quasistatic regime, and an other out of equilibrium.

4.3.1 Quasistatic transformations

We first study the case of quasistatic transformations, with $\lambda_i = 1$ and $\lambda_f = 1.5$ over a duration 50 ms, very long compared to the period of the oscillator. In this regime we can compute analytically the mean heat and work given to the particle. For quasistatic transformations, the heat fluctuations are equilibrium fluctuations with zero mean. Hence the average heat exchanged during the process is $\langle q \rangle = 0$. For $\langle w \rangle$, we can use the fact that for a quasistatic transformation, the equipartition of energy is satisfied at all times, hence $\frac{1}{2}\lambda(t)k\langle x(t)^2 \rangle = \frac{1}{2}k_BT$ for all t. Starting from eq.4.15:

$$\langle w \rangle = \int \frac{\dot{\lambda}}{\lambda(t)} \frac{1}{2} k\lambda(t)\langle x(t)^2 \rangle dt \tag{4.16}$$

$$= \frac{1}{2}k_BT \int \frac{\dot{\lambda}}{\lambda(t)} dt \tag{4.17}$$

$$= \frac{1}{2}k_BT \log\left(\frac{\lambda_f}{\lambda_i}\right) \tag{4.18}$$

For a protocol with $\lambda_i = 1$ and $\lambda_f = 1.5$, this gives $\langle w \rangle \simeq 0.2 k_BT$.

For any transformation, the Second Law of thermodynamics (or the Jarzynsky equality) give a bound:

$$\langle w \rangle \geq \Delta F \tag{4.19}$$

where ΔF is the free energy change of the particle between the initial and final equilibrium states. For a quasistatic protocol this bound is an equality and $\langle w \rangle = \Delta F$. As ΔF is a state function, its value depends only on the initial and final state, and not on the protocol used to perform the transformation. This gives us the value of ΔF for any protocol of this kind, even for non quasistatic transformations:

$$\Delta F = \frac{1}{2}k_BT \log\left(\frac{\lambda_f}{\lambda_i}\right). \tag{4.20}$$

The probability distribution function for the work performed on the particle $P(w)$ is computed over 5000 realisations of the quasistatic protocol. The result is shown as the blue curve on figure 4.7. $P(w)$ cannot be derived analytically, but it can be computed numerically using the parameters of the cantilever from calibration, and a model from ref. [57]. The theoretical prediction for $P(w)$ is shown as the red curve on figure 4.7. The experimental data are in good agreement with the theoretical predictions. We also measure the experimental mean work $\langle w \rangle = (0.22 \pm 0.02) k_BT$ and compare it with the predicted average from eq.4.18. The two values are close with only a 5% difference.

4.3.2 Out of equilibrium transformations

We also study faster protocols, with $\lambda_i = 1$ and $\lambda_f = 3$ performed in 5 ms, out of the quasistatic limit. In this regime, the mean heat exchanged is non-zero and $\langle w \rangle > \Delta F$. A way to study these protocols is to compare with the reversed protocol, starting from $\lambda_i = 3$ and ending in $\lambda_f = 1$, that we perform similarly. We can measure a distribution of work $P^F(w)$ for the forward process going from $\lambda_i = 1$ to $\lambda_f = 3$, and $P^R(-w)$ for the reverse process going from $\lambda_i = 3$ to $\lambda_f = 1$. The distribution for the forward (backward) process, as well as the theoretical predictions, are plotted in blue (orange) in figure 4.8. For a quasistatic process, we should have $\langle w \rangle_F = -\langle w \rangle_R = \Delta F$. Since the protocol is performed in a shorter time, the

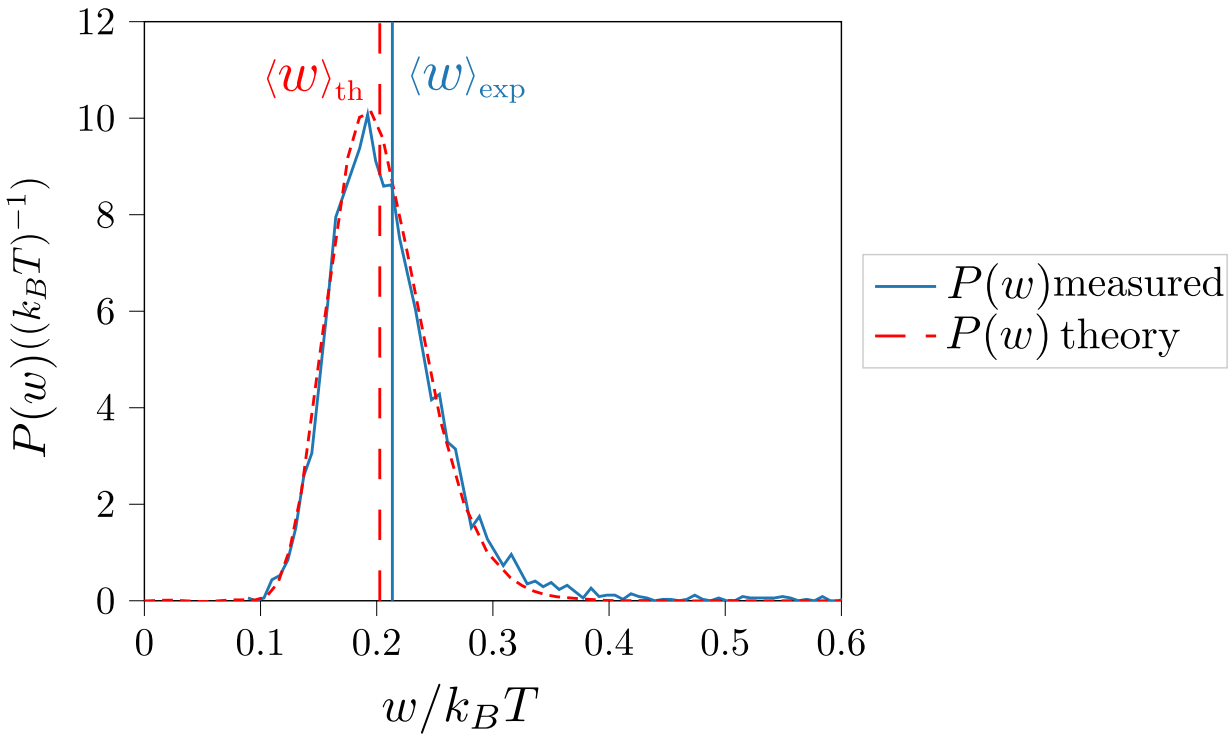

Figure 4.7: Probability distribution functions $P(w)$ for a quasistatic compression protocol with $\lambda_i = 1$, $\lambda_f = 1.5$, performed in 50 ms. Blue: experimental distribution obtained with 5000 realisations of the protocol. Red: theoretical prediction using [57]. The mean value of work $\langle w \rangle = (0.22 \pm 0.02) k_B T$ measured experimentally is plotted as a blue vertical line and is found close to the theoretical prediction (red dashed vertical line).

bound from eq.4.19 is a strict inequality for both the forward and the reverse process and we have $\langle w \rangle_F > \Delta F > -\langle w \rangle_R$. This is verified experimentally as shown on figure 4.8.

From the full distribution of probability $P^F(w)$, we can apply the Jarzynski equality to deduce the value of ΔF. The Jarzynski equality [33] states that:

$$\langle e^{-\beta w} \rangle = e^{-\beta \Delta F} \tag{4.21}$$

Thus we can compute $\Delta F_{JE} = -k_B T \log\big(\langle e^{-\beta w} \rangle\big)$, both for the forward and the reverse process. We find $\Delta F^F_{JE} = (0.57 \pm 0.02) k_B T$ for the forward process and $\Delta F^R_{JE} = (0.54 \pm 0.02) k_B T$ for the reverse process. Both values are in close agreement with the value from eq.4.20: $\Delta F = 0.55 k_B T$.

The forward and reverse protocol are also linked by Crooks relation[42] presented in 2.2.2:

$$\frac{P^F(w)}{P^R(-w)} = e^{\beta(w - \Delta F)} \tag{4.22}$$

This is a constraint on the probability distributions linking the forward probability of work w with the reverse probability of the opposite work $-w$. In particular when $w = \Delta F$, the right term becomes 1 and we have $P^F(w) = P^R(-w)$. This allows for another measurement of ΔF as the point where the two distributions cross. On figure 4.8, the two distributions $P^F(w)$ and $P^R(w)$ cross near the predicted value for ΔF.

We have 3 different ways of measuring ΔF: Using Jarzynski equality in the forward process, in the reverse process and using the crossing point of $P^F(w)$ and $P^R(w)$ according to Crooks relation. These 3 methods all give value for ΔF close to the prediction using the exact result for quasistatic transformations (eq.4.20).

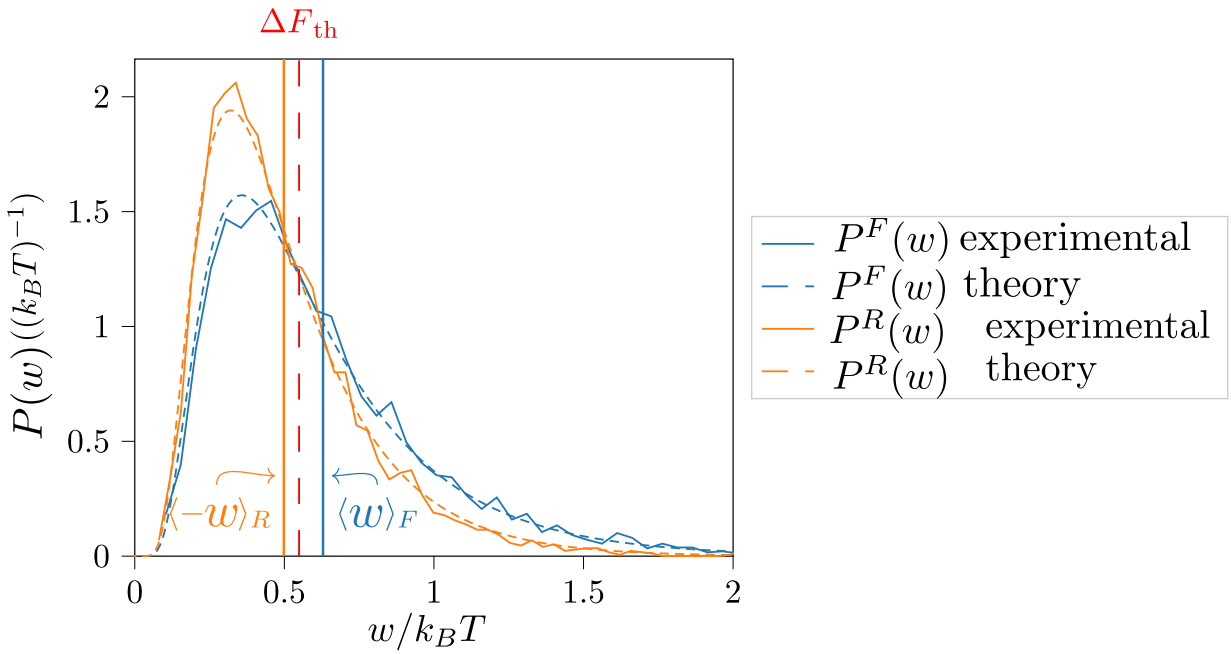

Figure 4.8: Probability distribution functions $P(w)$ for a fast compression protocol with $\lambda_i = 1$, $\lambda_f = 3$, performed in 5 ms. Blue: experimental distribution obtained with 5000 realisations of the protocol, and theoretical prediction (dashed). Orange: Experimental distribution obtained by performing the protocol in reverse, with $\lambda_i = 3$ and $\lambda_f = 1$ and theoretical prediction (dashed). According to Crooks's relation, the two distributions $P^F(w)$ and $P^R(w)$ cross at $w = \Delta F$. The two distributions indeed cross close to the value for ΔF computed using eq.4.20.

4.4 Conclusions

Our feedback can be programmed to act as a tunable artificial stiffness, that allows us to perform thermodynamic protocols at the scale of the cantilever, in which we recover the fundamental theorems of stochastic thermodynamics (Crooks relation, Jarzynski equality). Work is still needed to understand the mechanisms affecting the kinetic temperature T_K. An application could be to be able to tune the temperature using the same feedback, by adjusting τ_{corr}. This would allows us to experiment with a two parameters phase space (T, k) in which we can perform thermodynamic cycles, such as Carnot cycles [58–60], or Stirling cycle [61]. While these cycles are well-known at the macroscopic scale, their behaviour under fluctuations or out of equilibrium have been widely studied theoretically [62–64].

Chapter 5

Discrete sampling information engine

In this chapter, we present a realisation of a protocol inspired by [50], in which a measurement is performed on a particle in an harmonic trap. Depending on the outcome of the measurement, the potential is shifted or not thus selecting only events corresponding to work extraction. This constitutes an information engine: a cycle involving only one thermal bath during which a measurement is exploited to achieve work extraction. We study this protocol in different regimes, first by letting the particle relax after each cycle, then by reducing the time between cycles. Finally we study the role of information in the operation of the engine, and how it provides a bound on the amount of work that can be extracted.

5.1 Feedback protocol

Here, we introduce the protocol used to perform these experiments and achieve work extraction from thermal fluctuations. We study a protocol, illustrated in figure 5.1, where the position of the particle is read by a feedback with a sampling rate τ.

- We start with a potential centered in $-L$, $U(x,-L) = \frac{1}{2}k(x+L)^2$.
- Every time τ, the position of the particle, x, is read.
- There are two possible outcomes. If $x < h$, nothing is done. If $x > h$, the potential is instantaneously switched to $U(x,+L) = \frac{1}{2}k(x-L)^2$. Assuming $h > 0$, during this process, the potential energy of the particle is lowered, the internal energy of the particle decreases and work is extracted.
- The particle is let to relax for a time τ in the current potential well before the next reading, independently of the measurement outcome.

When the potential is switched, the operation is performed almost instantaneously. Therefore the heat exchanged from the bath to the particle is $q = 0$ and $\Delta U = -w$. Note that w is the work extracted from the particle, hence the minus sign. Working in units of $\sigma_x = k_B T/k$ for L and x, and in units of $k_B T$ for energies, the change in internal energy of the particle is:

$$\Delta U = \frac{1}{2}(x-L)^2 - \frac{1}{2}(x+L)^2 = -2Lx \tag{5.1}$$

If $x > 0$, $\Delta U < 0$ and $w > 0$ which means that the feedback is extracting work from the particle. The particle is left in the potential centered in L for a time τ. For simplicity, we present the case starting in the well centered in $-L$, with a threshold h. The cycle operates symmetrically if the potential was switched to $U(x,+L)$, using a threshold in $-h$.

This protocol is similar to the protocol proposed by Sagawa and coauthors [50]. The difference between the two protocols is that in our protocol the particle switches back and forth between two potential wells, centered in $\pm L$, whereas the protocol from Sagawa and coauthors uses successive potential wells centered in $-L$, L, $3L$, etc.

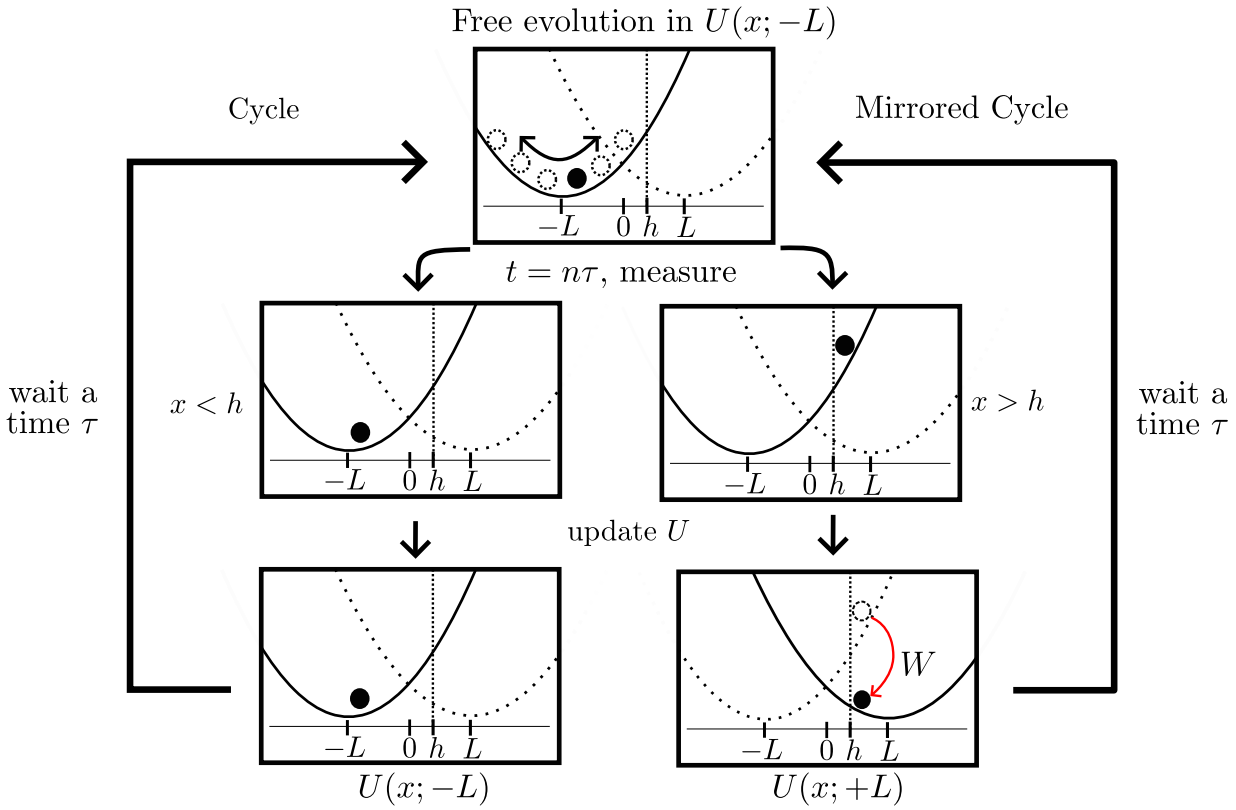

Figure 5.1: The discrete sampling protocol. Starting with a potential $U(x,-L) = \frac{1}{2}k(x+L)^2$ centered in $-L$, every time step τ the position x of the particle is measured. If $x > h$ the potential center is switched from $-L$ to L. In both cases we wait a time τ before performing the next measure.

5.2 Experimental implementation

To reproduce experimentally the aforementioned protocol, we need a Brownian particle in a harmonic trap and to be able to shift the center of the potential well, x_0, between two positions $-L$ and $+L$. Our setup presented in chapter 3 is particularly adapted to this kind of protocols, as the trapping is naturally produced by the stiffness, and the feedback loop is built to move the potential as a function of measurements.

For clarity, we will consider in the following that the protocol starts in the well centered in $-L$. Experimentally, the position of the particle is measured continuously with a sampling frequency $f_s = 100$MHz, with a harmonic potential which center is shifted to $x_0 = -L$ by applying a voltage $V_{FB}^- = -L/a$. The feedback compares the measured position x to the threshold $x_{th} = h$ and switch the voltage to $V_{FB}^+ = L/a$ if $x > x_{th}$, then the comparison between x and x_{th} and the update of the feedback voltage are frozen for a time τ. Once the voltage has been switched to V_{FB}^+, the feedback acts symmetrically with a threshold $x_{th} = -h$. Experimental signals are presented in figure 5.2. The deflection (blue curves) oscillates due to the resonant nature of the cantilever and is driven by the thermal noise. The oscillations are centered around the potential well center x_0. When x_0 is switched from $-L$ to $+L$, the deflection follows as the harmonic trap is moved. Red crosses mark moments when the feedback

is applied and a reading of the deflection is performed. Since the measurements are performed at discrete instants in time, the particle can cross the threshold x_{th} (green curve) many times without causing any change in the applied potential as the feedback is not acting.

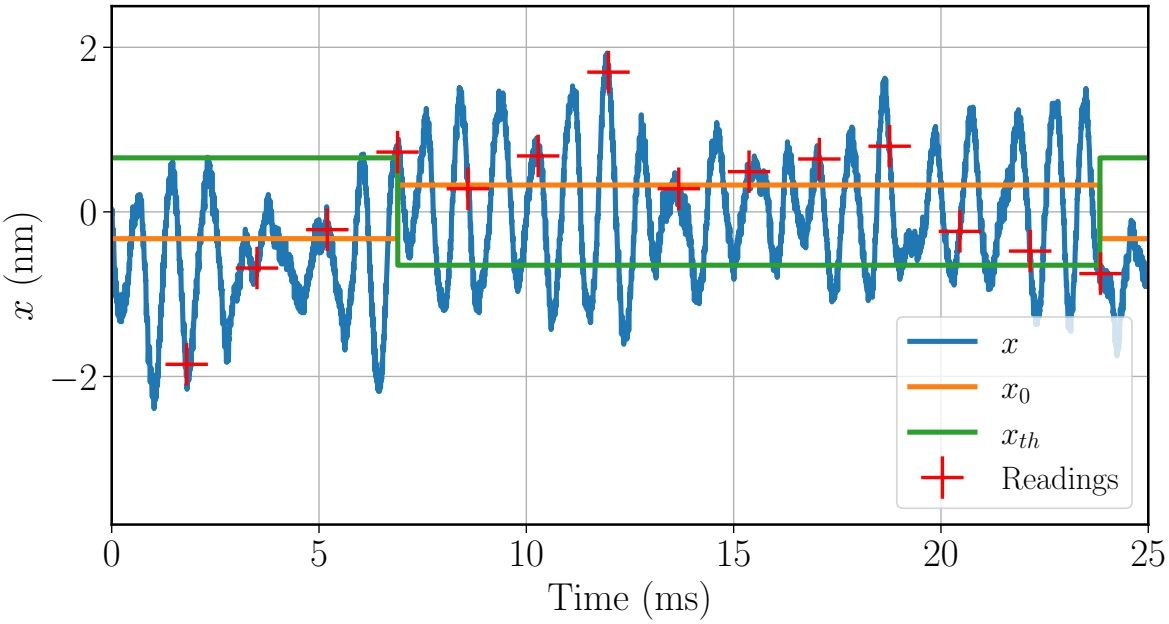

Figure 5.2: Experimental signals in time. The blue signal is the measured deflection of the cantilever, x. The orange curve is the position of the center of the potential well, x_0, and takes values $\pm L$. The green curve is the threshold the particle has to cross for the potential to be switched, x_{th}, that takes values $\mp h$. Red crosses mark moments where the feedback reads the position of the particle. Since the feedback loop updates only every time τ, the particle can cross the threshold without feedback on the potential if it happens between the readings.

From the measured trajectory and applied potential, we can compute the work of the particle on the electric field along the trajectory using results from 3.4. We can then obtain the statistics of the work extracted from the particle at each reading.

5.3 Long times limit

We first study the limit $\tau \to \infty$. This situation corresponds to the case where the particle is back to equilibrium between each reading of the feedback loop. Experimentally, we take $\tau = 16\, t_0$. Our oscillator has a quality factor $Q \simeq 8$ so the relaxation time is $t_{relax} = \frac{Qt_0}{\pi} = 2.54\, t_0$. Since $\tau \gg t_{relax}$ the system goes back to equilibrium between each measurement. We first present the probability distribution of work obtained when performing the cycle for a fixed set of the parameters L and h, and compare it to theoretical predictions. We then present an optimisation of the values of L and h to achieve maximum work extraction.

5.3.1 Work distribution

The goal of this cycle is to extract work from the particle. We show that our experiment successfully extracts work, and present the probability distribution of the work w extracted per cycle.

At each reading of x by the feedback loop, we compute the work w extracted by the protocol. The probability distribution function of w is shown in figure 5.3 for the case $L = 0.6$ and $h = 0$

(blue curve). A strong peak is present at $w = 0$ and corresponds to events where the feedback reads a position $x < h$ and does not switch the potential, leading to zero work. As expected, most events correspond to $w > 0$ and work is extracted by the feedback. This cycle allows us to extract work from a particle in contact with a single thermal bath, which is forbidden by the Second Law of thermodynamic. Here, using a protocol that adapts to the outcome of the measurement breaks this limit. We realise a so-called information engine, where the processing of information taken from the system is used to extract work.

We can compute analytically the probability distribution $P(w)$ of the extracted work to compare with experimental results. Since the system is at equilibrium at each reading, the position x is sampled from equilibrium in a harmonic well centered in $-L$ with a probability distribution:

$$\mathcal{P}_{eq}(x; -L) = \frac{1}{\sqrt{2\pi}} e^{\frac{(x+L)^2}{2}} \tag{5.2}$$

Using equation 5.1, we can compute the probability distribution of the work extracted from the particle at each reading w:

$$\mathcal{P}(w) = \begin{cases} \delta(w) \times \int_{-\infty}^{L+h} \mathcal{P}_{eq}(x; -L)dx = \frac{\delta(w)}{2}\left(1 + \text{erf}\left(\frac{L+h}{\sqrt{2}}\right)\right) & \text{if } w = 0 \\ \frac{1}{2L}\mathcal{P}_{eq}(\frac{w}{2L}; -L) = \frac{1}{2L\sqrt{2\pi}} e^{\frac{1}{2}(\frac{w}{2L}+L)^2} & \text{if } w > w_0 \\ 0 & \text{if } w_0 > w > 0 \text{ or } 0 > w \end{cases} \tag{5.3}$$

with $w_0 = 2Lh$, the minimum amount of work extracted. This value is reached when the particle is right at the threshold: $x = h$. The theoretical probability distribution, derived from this calculation is plotted for the case $L = 0.6$ and $h = 0$ in green on figure 5.3, using the same binning as for the experimental data. We recover the peak at $w = w_0 = 0$ corresponding to all the cases where $x < h$, and the Gaussian wing for $w > w_0$. The good agreement between theoretical predictions and experimental results means that this experiment is a reliable system to test this protocol and that we can take it to more complex regimes.

5.3.2 Optimisation of the engine parameters

We can look for the optimal regime for work extraction by exploring the space of parameters (L, h, τ) to maximize the work extracted per cycle. We start by tuning the pair (L, h) in this regime of $\tau \to \infty$.

The mean work extracted can be computed from eq.5.3:

$$\langle w \rangle = \int w\mathcal{P}(w)dw = \frac{1}{2L\sqrt{2\pi}} \int_{w_0}^{+\infty} e^{\frac{1}{2}(\frac{w}{2L}+L)^2} dw \tag{5.4}$$

$$= L^2 \left(\text{erf}\left(\frac{L+h}{\sqrt{2}}\right) - 1\right) + L\sqrt{\frac{2}{\pi}} e^{\frac{1}{2}(L+h)^2} \tag{5.5}$$

The parameters L and h can be chosen to optimize the amount of work and the mean power $P = \langle w \rangle / \tau$ extracted by the feedback. According to eq. 5.1, increasing L increases the work extracted. However, increasing L also puts the threshold further away from the center of the potential and makes it harder for the particle to cross it. Finding the optimal value for L is a competition between the number of work extraction events and the amplitude of these events.

A series of experiments is performed with $\tau = 16\, t_0$ and $h = 0$ fixed, and varying L from 0.2 to 1.4 by steps of 0.2. For each value of L, 450 files with a duration of 1 s are acquired. This corresponds to a total of about 30000 readings for each value of L.

For each experiment, the number of switching and the work extracted are computed. The results are shown on figure 5.4, showing the rate of switching events (orange) and the average

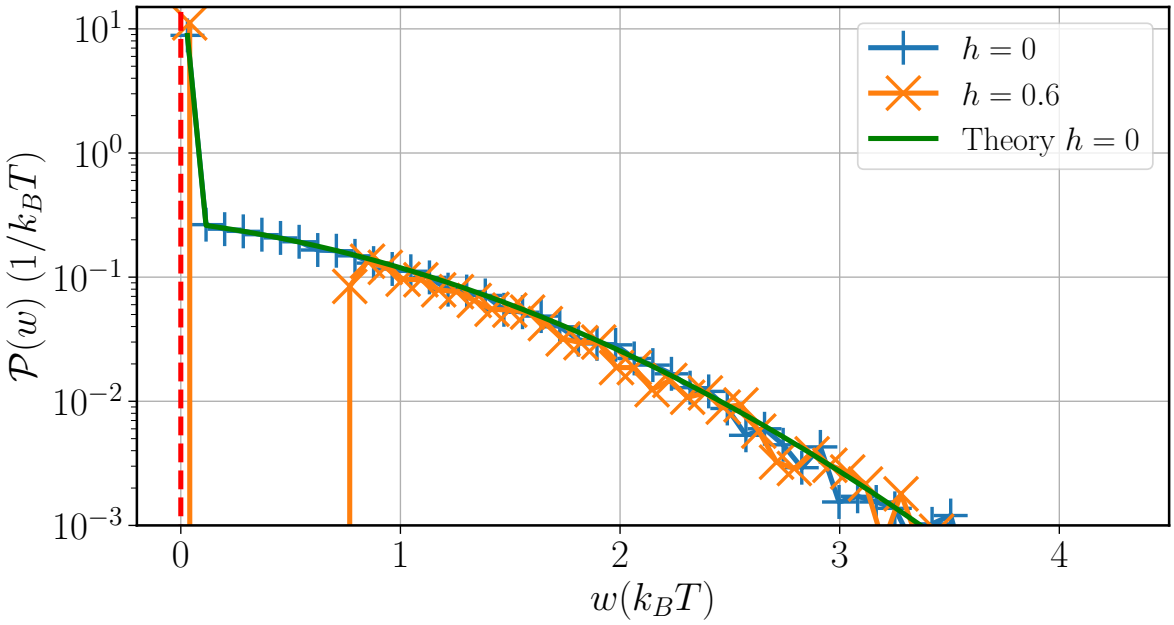

Figure 5.3: Probability distribution functions of the work performed by the particle at each reading of the feedback loop for $L = 0.6$ with $h = 0$ (blue) and $h = 0.6$ (orange) with $\tau = 16\,t_0$. The measured pdf is obtained over 10^4 readings of the position. All events are for $w > 0$, which corresponds to work extraction. A strong peak in $w = 0$ corresponds to all the readings where $x < h$ and the potential is unchanged, hence $w = 0$. For $h = 0.6$, the minimal amount of work extracted at switch is $w_0 = 2Lh$. Therefore $\mathcal{P}(w) = 0$ for $0 < w < w_0$. Compared to the case $h = 0$, all the events $0 < w < w_0$ now contributes to the peak in $w = 0$. Comparison with the theoretical expectation (green) computed from eq. 5.3

amplitude of work extracted at the switching (blue). As predicted, the number of events decreases as L increases, whereas their amplitude raises. These two effects are in competition and an optimum can be found.

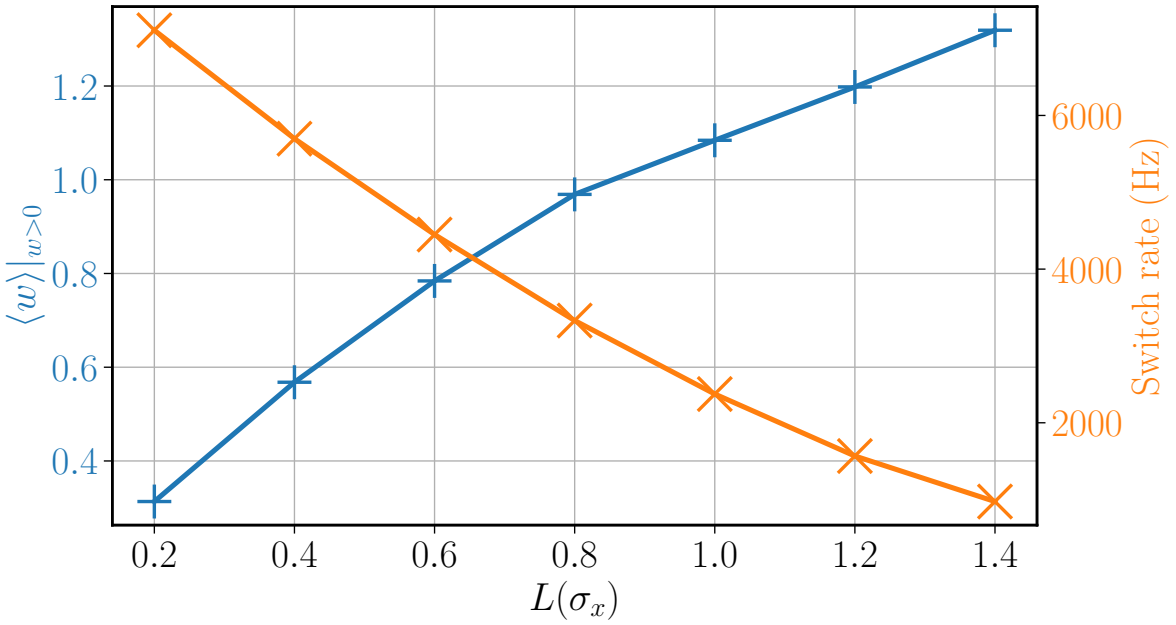

Figure 5.4: Average work extracted per switching of the potential and frequency of these events as a function of L, for $h = 0$. The amplitude of events (blue) increases as L increases, but the number of events (orange) decreases.

Since the system has the time to relax to equilibrium between each reading by the feedback, there is no memory of the previous reading and the previous switch in the potential. Therefore it is equivalent to operate back and forth between two potential wells or to operate with successive wells. In this regime our protocol is equivalent to the protocol from Sagawa [50], for which analytical results have been derived by Parks et al. Furthermore, in the limit of $\tau \to \infty$ the overdamped case from [50, 65] and our experiments in the underdamped regime are equivalent because the system has time to relax to equilibrium between each reading. In both situations the probability distribution for x is $\mathcal{P}_{eq}(x; -L)$ defined in eq.5.2.

We compute the mean power over a cycle of the engine from our experimental data, for each value of L. Figure 5.5 shows the extracted power per cycle of the engine as a function of L at $h = 0$. We find an optimal work extraction for $L^* \simeq 0.6$, close to the predicted value by Park et al. at $L^* \simeq 0.612$.

The position of the threshold, h, can also be tuned. Simple arguments allow us to find that the optimal value is $h = 0$. Indeed, if $h < 0$ (figure 5.6a), then we are allowing the system to switch when the particle is in x with $h < x < 0$ leading to $w < 0$, according to equation 5.1. In this case, the feedback is providing work to the system to put it in a higher energy state when the potential is switched. If $h > 0$ (figure 5.6c), we are imposing a minimal amount of work to be extracted each time $w > 2Lh$, which means that each time the particle is measured in x with $0 < x < h$, no work will be extracted and $w = 0$ whereas if the potential was switched the work extracted would have been positive. The feedback is loosing occasions to extract work.

This has been verified experimentally by measuring the extracted power at different values of h for a fixed value of $L = 0.6$. An example of the resulting pdfs is shown in orange on figure 5.3 for $h = 0.6$. The two curves for $h = 0$ and $h = 0.6$ are similar for $w > w_0 = 2Lh$, however for $0 < w < w_0$ the pdf falls to 0 and the peak at $w = 0$ is increased.

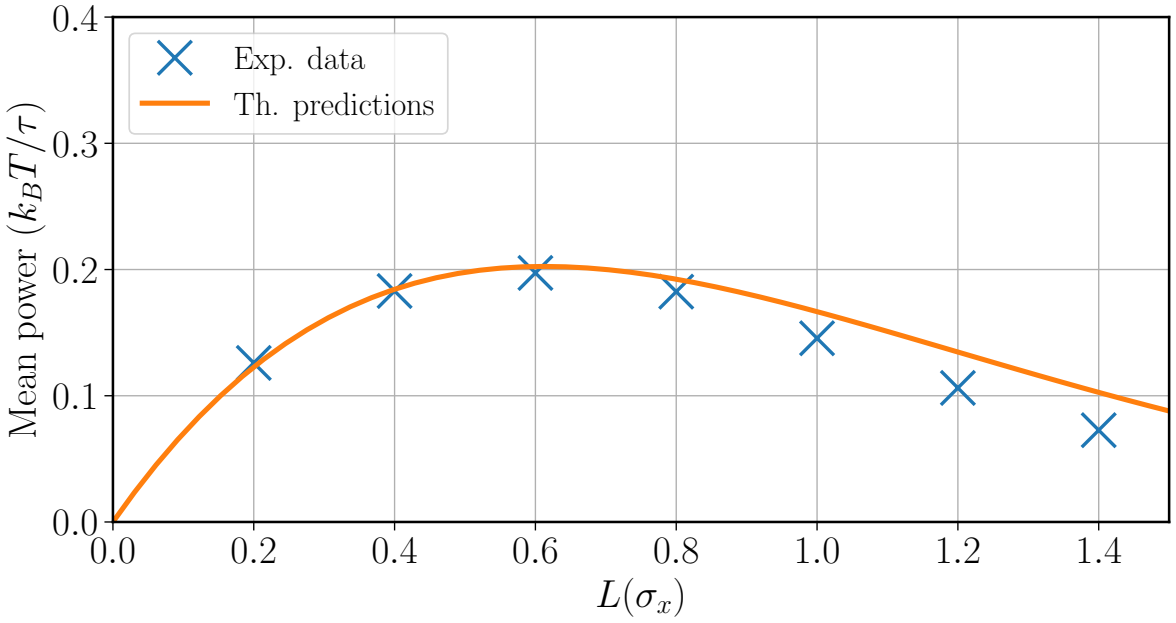

Figure 5.5: Extracted power as a function of L with $h = 0$ in the limit $\tau \to \infty$. An optimum appears for $L \simeq 0.6$.

The extracted power as a function of h is shown on figure 5.7. As expected the power decreases as soon as $h \neq 0$.

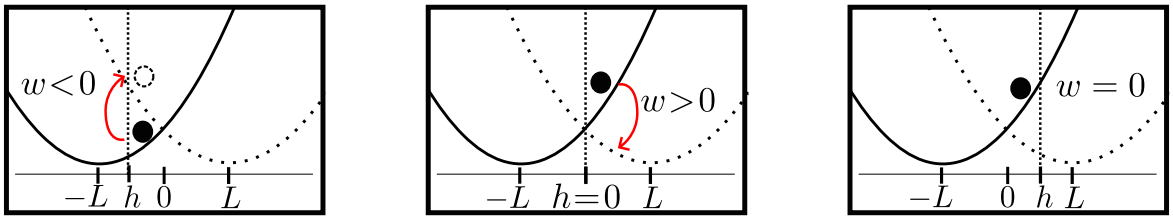

(a) $h < 0$ (b) $h = 0$ (c) $h > 0$

Figure 5.6: Different situations depending on the value of h. a) $h < 0$: The potential is switched for positions $x < 0$, resulting in negative work extracted. b) $h = 0$: The potential is switched if and only if $x > 0$, which is equivalent to $w > 0$ and is thus the optimum. c) $h > 0$: There are some values $0 < x < h$ where the potential is left unchanged and $w = 0$ while work could have been extracted.

Park et al. compute analytically the average work extracted per event for different values of L and h, in the case where $\tau \to \infty$. What they found is that the largest work is extracted for $L = 0.6$ and $h = 0$, which corresponds to the results we obtained experimentally. Note that Park et al. optimize the work per event whereas in our experiment we optimize the extracted power. However, in the case where $\tau \gg \tau_{relax}$, the frequency of events is limited mostly by the time τ during which the particle equilibrates, and both optimizations give the same result.

The regime $\tau \to \infty$ is a simple regime to study theoretically. The work distributions and optimal parameters obtained experimentally are totally compatible with the theory. We can also explore the intermediate time limit where the system doesn't return fully to equilibrium between cycles.

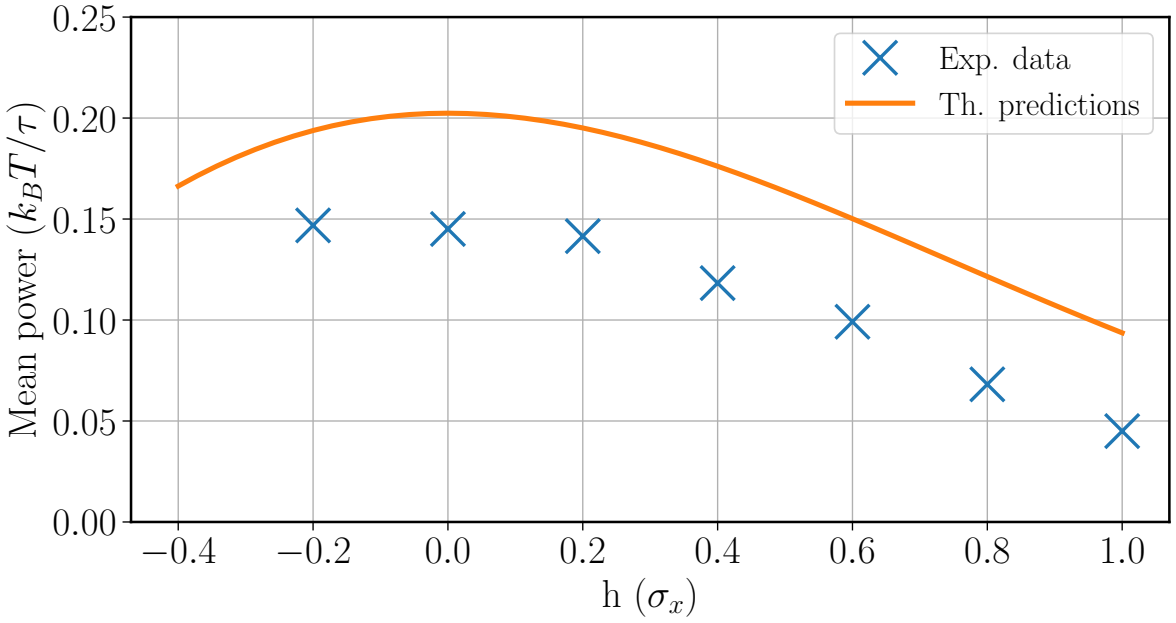

Figure 5.7: Extracted power for a fixed value of $L = 0.6$, as a function of the position of the threshold h in the limit $\tau \to \infty$. As predicted, the optimal value is found at $h = 0$.

5.4 Intermediate time regime

A way to increase the power output of the engine is to reduce the time between cycles τ, preventing the system to totally relax between cycles. We measure the extracted work while keeping $L = 0.6$ and $h = 0$ fixed but varying the sampling time from $\tau = 0.1\,t_0$ to $\tau = 3\,t_0$. For comparison, simulations of an overdamped 1D brownian particle under the same feedback protocol are performed.

5.4.1 Numerical simulations

For overdamped particles, the mass term in the Langevin equation can be neglected. An overdamped particle in a harmonic potential centered in x_0 can be described by the following equation:

$$\gamma\dot{x} + k(x - x_0) = \sqrt{2\gamma k_B T}\xi(t) \tag{5.6}$$

The timescale for the diffusion is $\mu = k/\gamma$. The typical spatial scale is given by $\sigma_x = \sqrt{k_B T/k}$. By rescaling time in unit of μ as $\tilde{t} = t/\mu$, and positions in units of σ_x as $\tilde{x} = x/\sigma_x$ and $\tilde{x_0} = x_0/\sigma_x$, the equation becomes:

$$\frac{d\tilde{x}}{d\tilde{t}} + (\tilde{x} - \tilde{x_0}) = \sqrt{2}\xi(\tilde{t}) \tag{5.7}$$

Working in these units for the system, there are no parameters to be set for the system and a single set of simulations can describe all overdamped systems.

To perform simulations, we need to turn eq.5.7 into an evolution equation for discrete time processes. Using a discrete time step dt, the position is described by a series $X_n = \tilde{x}(n \times dt)$ with an evolution:

$$X_{n+1} = X_n + \sqrt{2dt}\Xi_n - dt(X_n - \tilde{x_0}) \tag{5.8}$$

where $\{\Xi_n\}$ is a set of independent gaussian random variables with zero mean and unitary variance. Using this equation we can simulate the evolution of an overdamped particle in a potential well centered in x_0.

To simulate our feedback protocol, we initialise the simulation with a position X_0 sampled from an equilibrium distribution with $x_0 = -L$. As in the experimental setup, the position X_n is compared to a threshold $x_{th} = h$. If $X_n > h$, the simulation continues with $x_0 = +L$ and $x_{th} = -h$, else it continues with $x_0 = -L$ and $x_{th} = h$. After this check, a number of simulation steps τ/dt are performed, during which no check is performed. This accounts for the discrete sampling time in our experiment while ensuring that we can use simulation steps dt small enough for the simulation to be stable.

We perform simulations with $L = 0.6$ and $h = 0$, with values of τ ranging from $0.10\,\mu$ to 3μ and a time step $dt = 0.01\,\mu$. An example of simulated trajectory is shown in figure 5.8. The blue curve is the simulated overdamped dynamic and the orange curve indicates the location of the center of the potential well. Since $h = 0$, the threshold for comparison is always $x_{th} = 0$, and is represented by a green dashed line. Crosses indicates the moments where readings are performed. For each reading, the extracted work is computed. The distribution of work for the same simulation is shown in figure 5.9. This distribution of work has a very similar shape as the one obtained experimentally in the underdamped regime. Since the feedback extracts work only if the threshold is reached, w is always positive. A peak near $w = 0$ comes from all the readings without switching, while the positive wing of the distribution comes from events where the potential is switched.

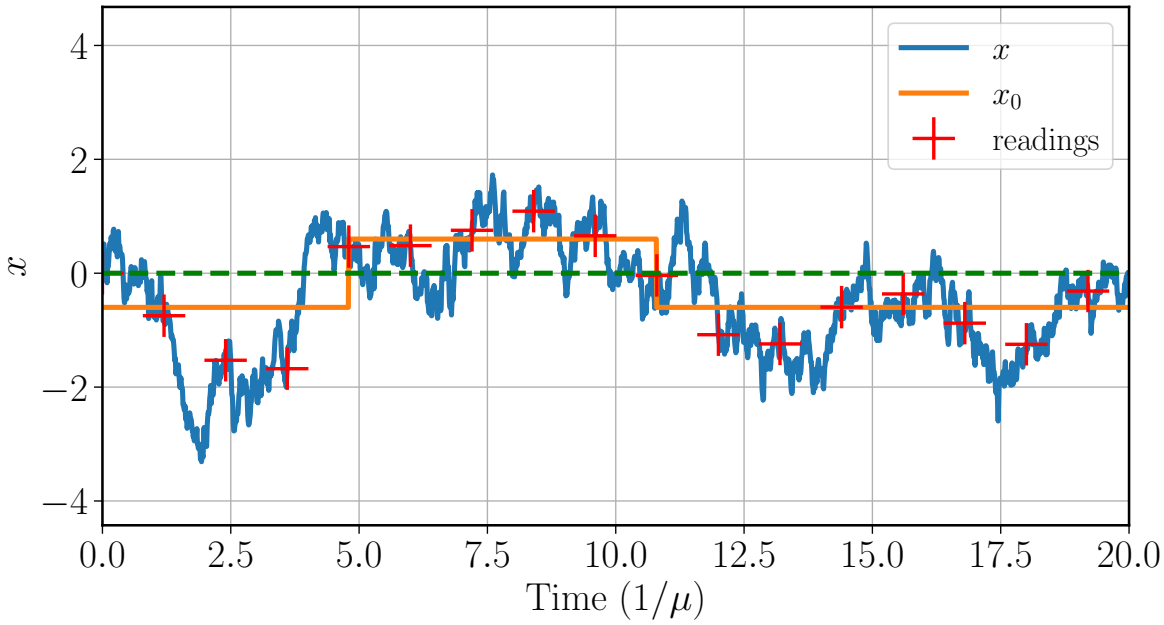

Figure 5.8: An example of simulated overdamped dynamic for $L = 0.6$, $h = 0$, and $\tau = 1.2\,\mu$. Blue: simulated positions X_n. Orange: Center of the potential well $\tilde{x_0}$. Green: Threshold used by the feedback at $h = 0$. Crosses note moments where a reading is performed and the position is compared to the threshold.

While the shape of the distribution $P(w)$ is similar to the ones obtained experimentally for the underdamped regime, we compare in the next section the power extracted as a function of τ for both regimes and show that the two regimes have very different behaviours.

5.4.2 Comparison between overdamped and underdamped

To compare the overdamped simulation and underdamped experiments, we used the relaxation time of the systems, t_{relax} as a unit of time. Since the two systems are in different regimes,

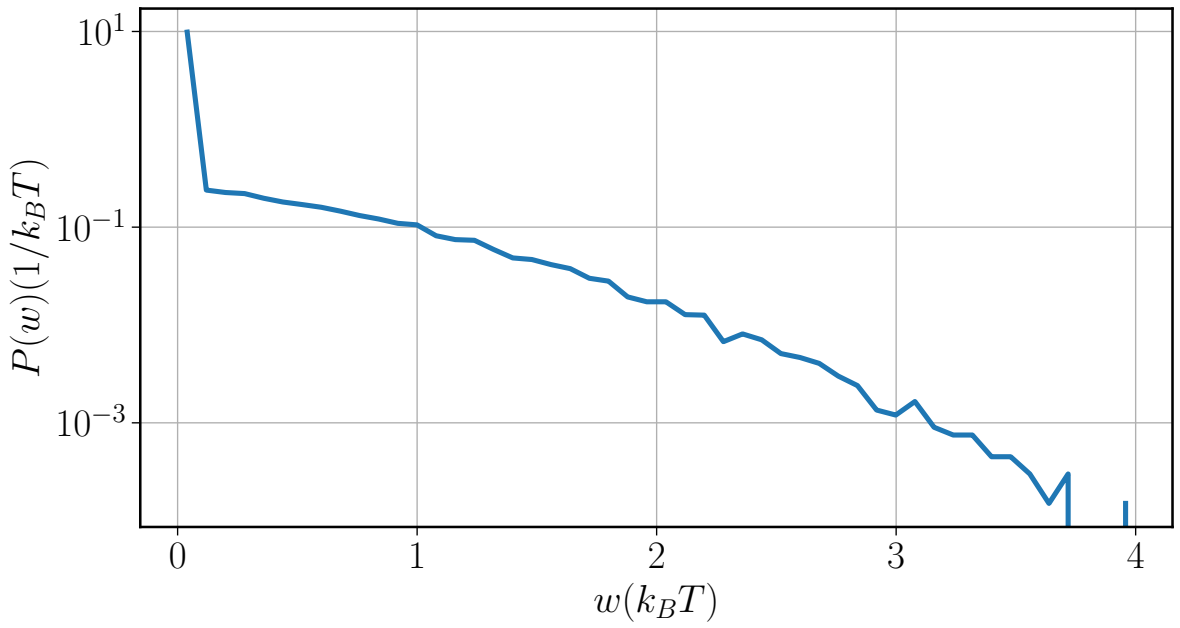

Figure 5.9: Probability distribution of w extracted in the overdamped simulation for $L = 0.6$, $h = 0$ and $\tau = 1.2\,\mu$.

they have different definitions for t_{relax}:

$$t_{relax} = \begin{cases} \frac{Qt_0}{\pi} & \text{for underdamped} \\ \gamma/k = \mu & \text{for overdamped} \end{cases} \tag{5.9}$$

Figure 5.10 shows the comparison of the power extracted for the two regimes as a function of τ/t_{relax}. Using t_{relax} as a unit for times, the curve of overdamped regime appears as an enveloppe for the curve of underdamped regime.

To confirm this scaling with t_{relax} we perform the same experiment under low pressure to raise the quality factor. The pressure in the chamber is reduced to 10 mbar, lowering the effective viscosity term γ in eq.3.2, which increases the quality factor. In these conditions we measure $Q \simeq 20$ from a fit of $S_x(\omega)$ using the SHO model presented in 3.1. The green curve on figure 5.10 shows the results from this experiment. The overdamped result still behaves as an envelope. This is a confirmation that the relaxation time is the good time scale to study this system. The extracted power in the underdamped regime is always higher than for the overdamped. This can be understood as the underdamped regime couples two degrees of freedom (position and velocity) with a typical energy k_BT, whereas in the overdamped regime, only the position degree of freedom is relevant, with typical energy $\frac{1}{2}k_BT$.

5.4.3 Specific underdamped effect

We now discuss the anomalies that appear on the curve for the underdamped regime at specific values of τ, where the extracted power drops. To understand these anomalies, we look at the time between switching events by looking at the mean number of readings performed on the particle before the threshold is crossed: $\langle n \rangle$. This number corresponds to the number of consecutive events with $w = 0$ before an event with $w > 0$. $\langle n \rangle$ is represented in figure 5.11 as a function of τ, for $Q = 8$. For most values of τ, $\langle n \rangle \simeq 3.5$. However for values of τ corresponding to the anomalies on figure 5.10, $\langle n \rangle$ raises up to 7. This means that for these specific values of τ, the number of events with $w = 0$ increases. This can also be seen on figure 5.12 where

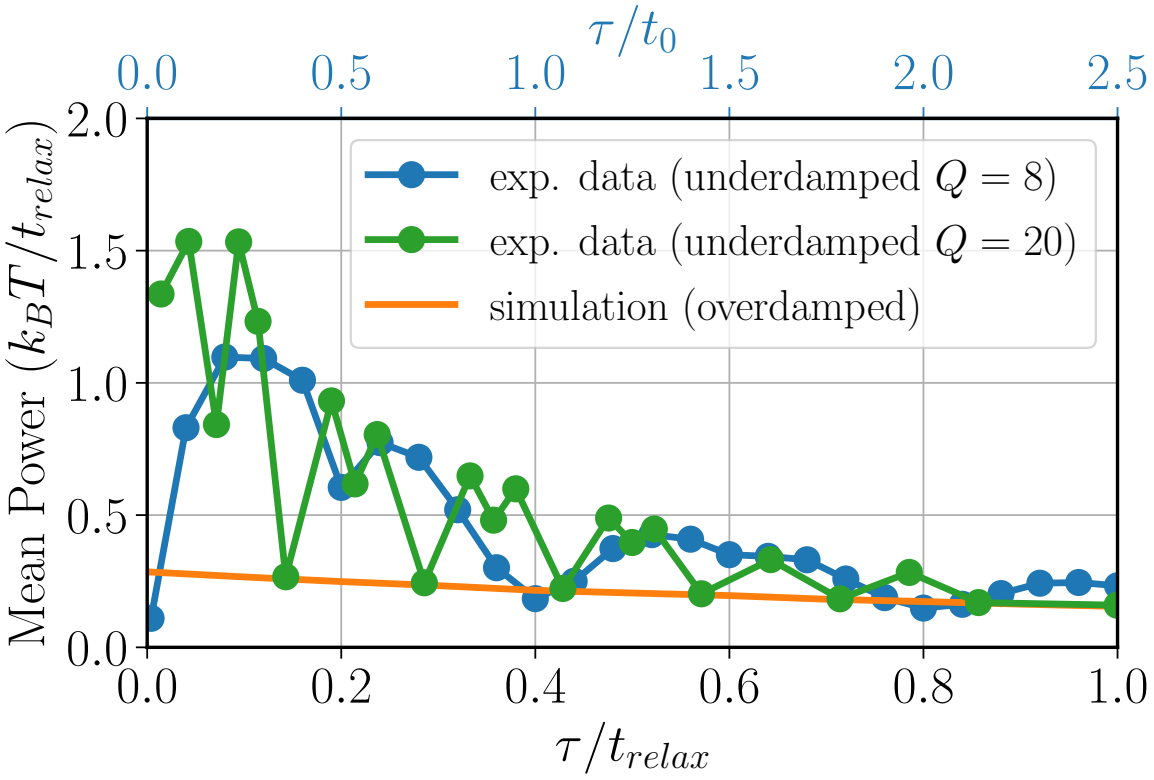

Figure 5.10: Extracted power as a function of τ/t_{relax}. In blue, experimental data with $L = 0.6$, $h = 0$ and $Q = 8$ in the underdamped regime. In green, experimental data with $L = 0.6$, $h = 0$ and $Q = 20$. In orange, data from simulations of an overdamped brownian particle. The top horizontal axis shows the sampling time τ in unit of the period of t_0 for $Q = 8$. We can notice that the minima of extracted power for $Q = 8$ falls on half-integer values of t_0.

two distributions of work are presented, one in red corresponding to $\tau = 0.4\, t_{relax} = 1\, t_0$, an anomalous case, and one in purple corresponding to $\tau = 0.28\, t_{relax} = 0.7\, t_0$, a case close to the envelope.

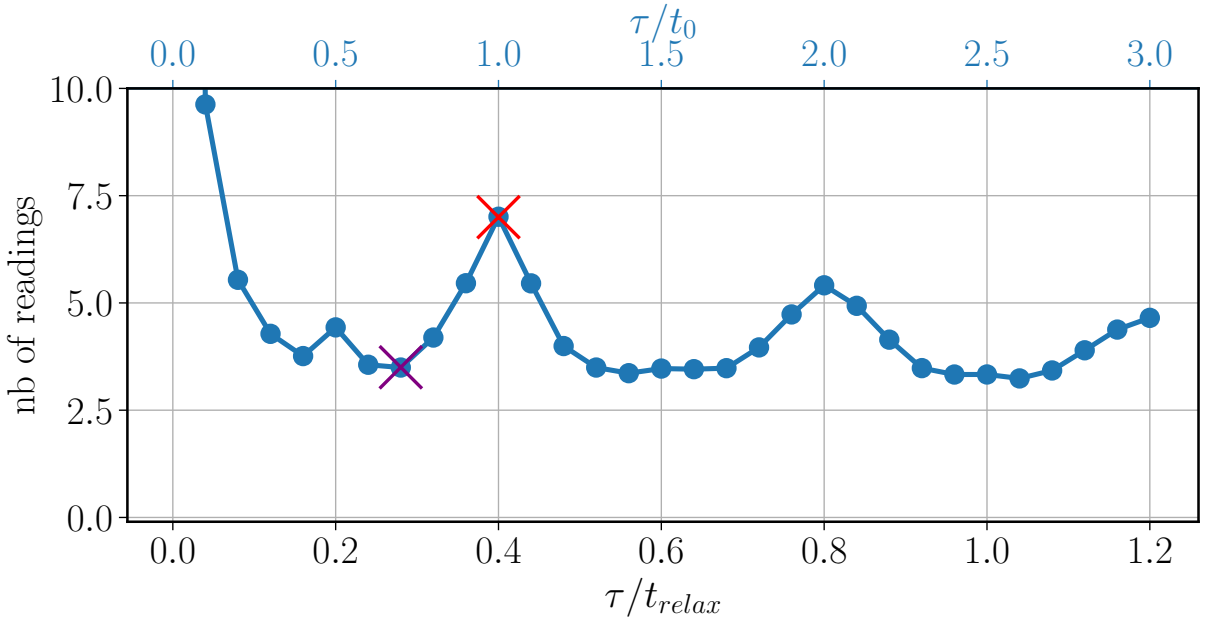

Figure 5.11: Mean number of readings between potential switches as a function of τ, with $Q = 8$. For most values of τ, about 4 readings are needed between switching of the potential. However for specific values, corresponding to the anomalies on fig. 5.10, this number increases. The top horizontal axis shows the sampling time τ in unit of the period of t_0. The increases of this number fall on half-integer values of t_0.

We also plot on figure 5.12 the pdf of the extracted work in the case $Q = 8$ for different values of τ: $0.4\, t_{relax}$ and $0.28\, t_{relax}$ corresponding respectively to the red and purple crosses on figure 5.10 and 5.11. Two effects can be noticed. First the peak in $w = 0$ is stronger for the anomalous case due to the increase in $\langle n \rangle$. The second effect is that in the anomalous case, the spread of the non-zero part of the pdf is smaller. Since $w = 2Lx$, this means that the particle is found closer to the threshold when the measurement is performed. Both effects contribute to a reduction of the extracted power and can be understood as a synchronisation effect between our measurements and the natural oscillation of the underdamped particle. Indeed, the anomalies of figure 5.10 fall exactly on integer and half-integer values of t_0.

We compare a standard overdamped simulation to an underdamped experiment in a new regime. We show that the relaxation time is the universal time to compare these systems. This comparison highlights the specificity of the underdamped dynamics, where synchronisation effects arise.

5.5 Short times limit

In figure 5.10, we can see that the extracted power falls to 0 as $\tau \to 0$. To understand this phenomenon, we perform experiments in the regime where $\tau \ll t_{relax}$, taking $\tau = 0.01 t_0$.

In the regime when $\tau \to 0$, the position of the system is sampled continuously, and it can be studied as a first-passage problem. Since the feedback reads the position of the system continuously, the excursion of the particle above the threshold is limited and the potential is switched as soon as the particle reaches the threshold. A particle in a potential $U(x, -L)$, will

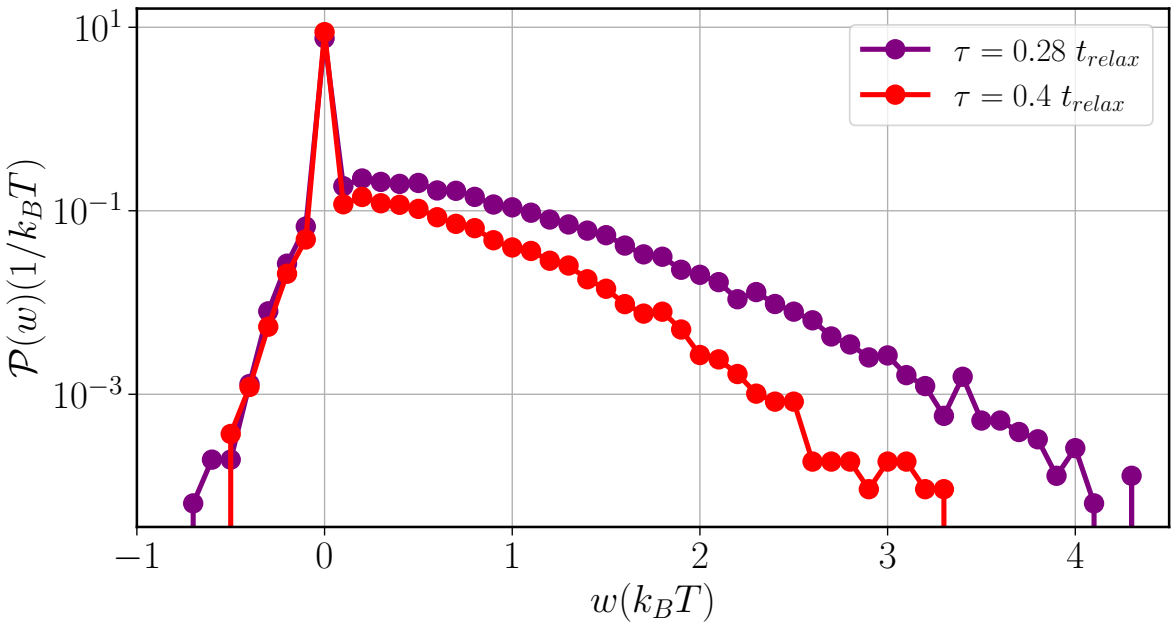

Figure 5.12: Probability distribution function of extracted work after readings for $L = 0.6$, $h = 0$, $Q = 8$, with $\tau = 0.28\, t_{relax}$ and $\tau = 0.4\, t_{relax}$.

start in $-h$ as a result of the previous potential switch with target in h, as illustrated in figure 5.13.

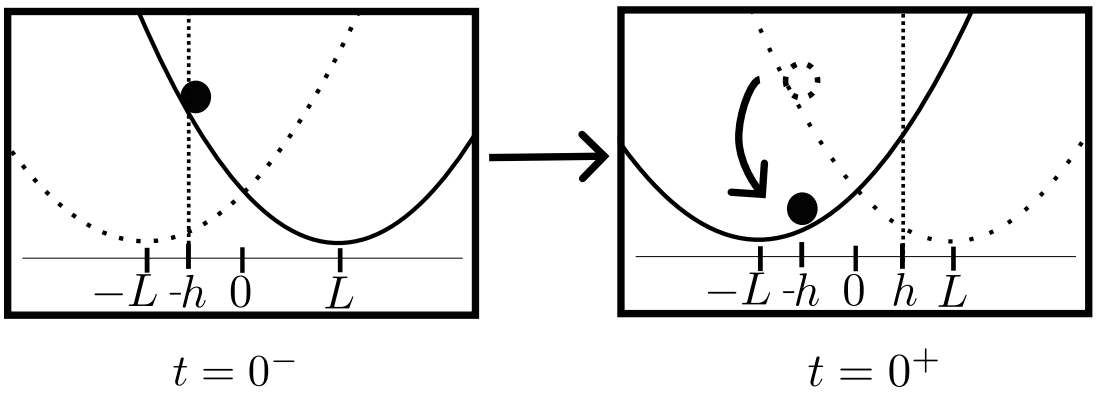

Figure 5.13: Evolution of the potential and threshold during the switching. Left: Just before the switching, the potential is centered in $+L$. Since $\tau \to 0$, the particle has just reached the target in $-h$. $U(x; +L)$. Right: Just after the switching, the potential is centered in $-L$. The particle is located in $-h$ and the target for the next switch is now in $+h$.

We measure experimentally the pdf of work extracted in this regime with $h = 0$. The results are shown in blue on figure 5.14. The distribution is sharply peaked in $w = 0$. Experimentally, since $\tau \ll t_0$ but $\tau \neq 0$, x can be slightly above the threshold. According to eq. 5.1, since the switching happens close to $x = h$, the work extracted is $w = 2Lh$. Therefore, if $h = 0$ we have $w = 0$ and no work can be extracted.

In order to have $w > 0$ and extract work, we need to use $h > 0$. An example of work distribution obtained with $h = 0.6$ is shown in orange on figure 5.14. A peak in $w = 0$ remains from all the readings where x hasn't reached the threshold but the rest of the distribution has been shifted to positive values of w.

However, as h is raised, the position of the target is moved away from the initial position, and the time needed for the particle to reach the target is increased. As a consequence there is

an optimal value of h that has to be found to maximize the extracted power.

Working with $\tau \to 0$ allows for very fast experiments. Which allows for extensive exploration of the parameter space. We measure the mean power extracted as a function of both L and h to find the optimum. The results are presented as a heatmap on figure 5.15a. The optimal value for power extraction is found at $L^* = 0.6$, $h^* = 0.75$ and gives a power $P^* = 1.48 k_B T / t_{relax}$. This value is higher than all the values measured in section 5.4 for the same value of $Q = 8$, but different values of L and h.

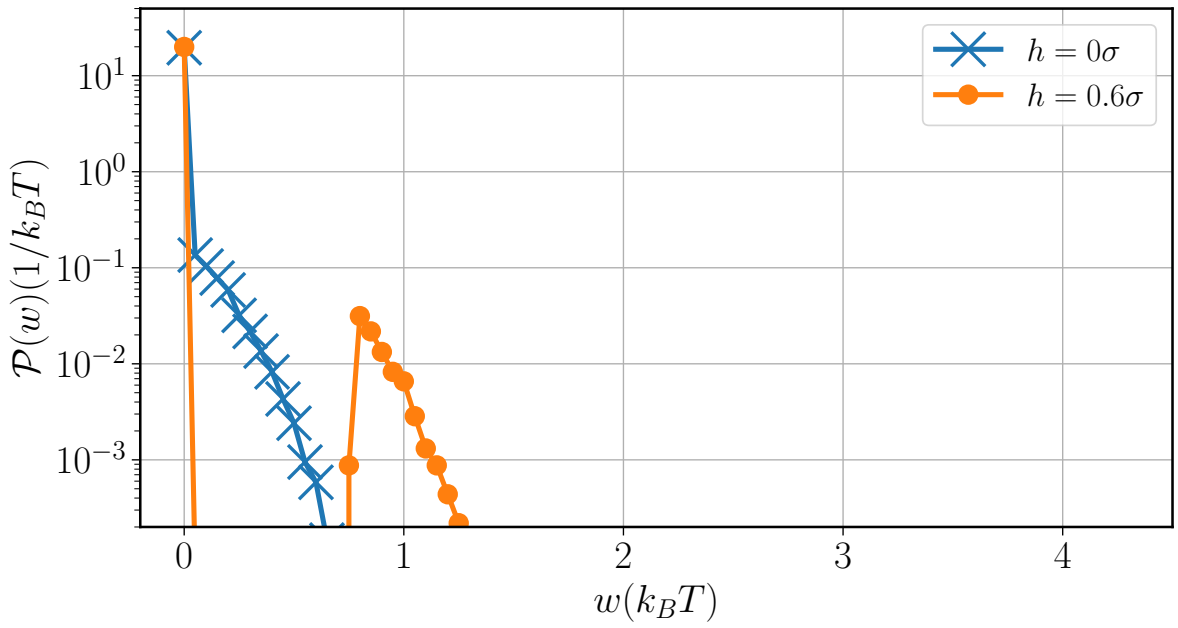

Figure 5.14: Histograms of work computed at each switching in the potential for $\tau = 0.01\, t_0$, $L = 0.6$ and $h = 0$ (blue curve) and $h = 0.6$ (orange curve). Since $\tau \ll t_0$, the potential is switched soon after the particle reaches the threshold, which leads to much narrower distributions compared to the case $\tau \to \infty$ from figure 5.3. The effect of moving the threshold h is that the position of the histogram is switched from around 0 to a non-zero value.

To compare, we simulated the trajectories of overdamped particles in a harmonic potential and computed the power extracted for different values of L and h. We use the same simulation scheme as presented in 5.4.1. This time, since $\tau \to 0$, a check between the position X_n and the current threshold is done at each time step dt of the simulation. Since in this regime the potential is always switched with the particle exactly in $+h$, the work extracted will always be $w_0 = 2Lh$. What limits the extracted power is the first passage time, t_{fp}.

To simulate our protocol in the short times, we impose a starting condition $X_0 = -\tilde{h} = h/\sigma_x$, and we simulate the trajectory corresponding to the evolution in this simple potential well. For each trajectory, we look for the first passage time t_{fp} where the condition $X_n > h$ is satisfied for the first time. Figure 5.16 shows examples of simulated trajectories for $L = 1$ and $h = 1$. All the trajectories starts in $X_0 = -h = -1$ and evolves in a single potential well centered in $-L = -1$. The first passage time is measured when a trajectory first reaches the threshold in $h = 1$, marked by the black line. Crosses indicate the first passage of each trajectory.

For each set of values for L and h, 10000 trajectories are simulated, giving a set of 10000 values of first passage times. The probability distribution of first passage times for $L = 1$ and $h = 1$ is shown in figure 5.17. From this distribution, we compute for each pair (L, h) the mean first passage time, from which we deduce the average extracted power $w_0 \times \langle t_{fp} \rangle$. From

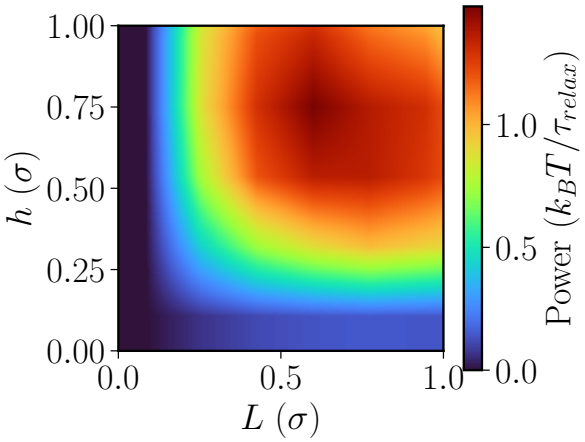

(a) Experimental heatmap of the extracted power as a function of L and h for $\tau = 0.01\,t_0$ in the underdamped regime. The optimal value is at $L^* = 0.6$ and $h^* = 0.75$

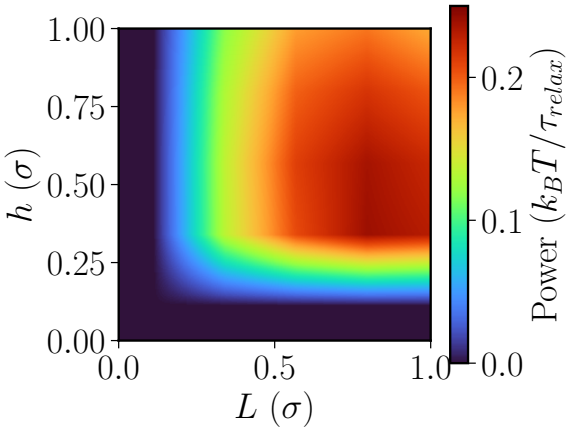

(b) Computed heatmap of the extracted power as a function of L and h for $\tau = 0.01\,t_0$ in the overdamped regime. The optimal value is at $L^* = 0.75$ and $h^* = 0.5$.

Figure 5.15

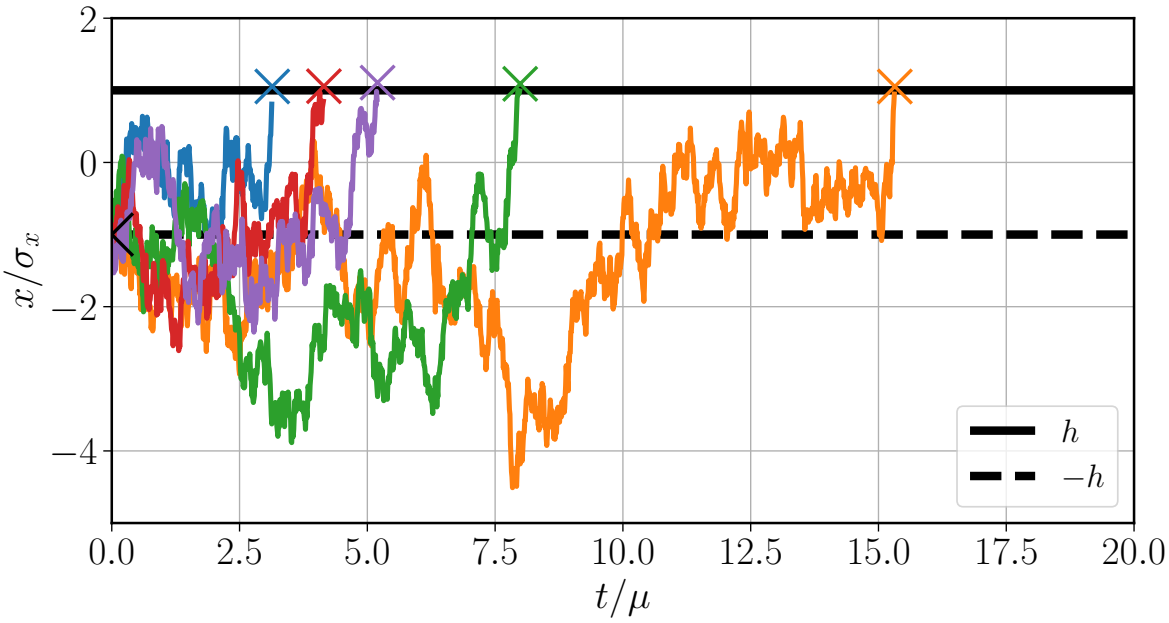

Figure 5.16: Simulated trajectories in the limit $\tau \to 0$ with $L = 1$ and $h = 1$ (black line). All the trajectories start in $-h = -1$ (black marker). Since the problem can be linked to a first passage time problem, the trajectories are ended after reaching the threshold.

the simulations, we construct a heatmap of the extracted power, shown figure 5.15b. In the overdamped case, the simulation predicts a maximum power $0.25 k_B T / t_{relax}$ for $L = 0.75$ and $h = 0.4$.

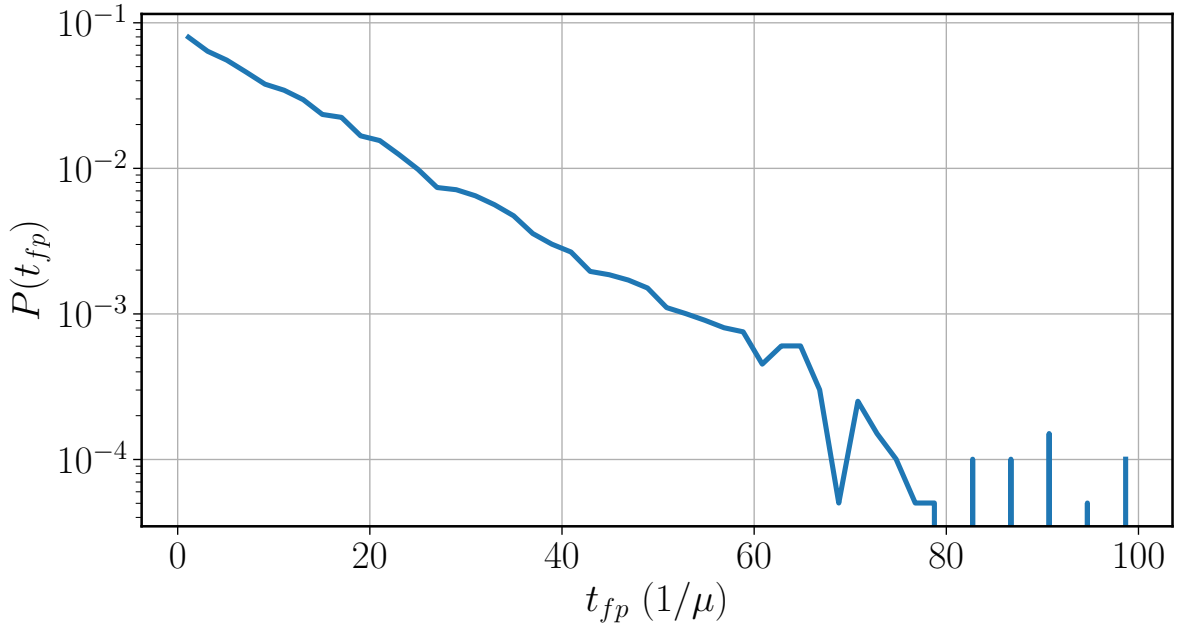

Figure 5.17: Distribution of the first passage times for $L = 1$ and $h = 1$ in the limit $\tau \to 0$, taken over 10000 simulated trajectories.

The main noticeable difference between the underdamped and the overdamped case is that for the former the optimum is $L^* < h^*$ whereas the optimum is $L^* > h^*$ for the latter. For the overdamped case, $L^* > h^*$ means that the target and the initial position of the trajectories are close. Since the dynamic is driven by diffusion, a low value of h^* means that it will be easy for the particle to diffuse from $-h^*$ to $+h^*$ and this optimum corresponds to a case with more switching events and lesser work extraction per events. For the underdamped case $L^* < h^*$ means that the particle will be far away from the threshold after a switch of the potential. However due to the oscillations, the particle will easily come back close to the threshold. This allows for a large work extraction per event while reducing the drawbacks of starting far from the threshold.

5.6 Information

We have built an engine able to extract work using information. A way to measure the efficiency of the engine is to weight the information used against the work extracted. For the simpler case of $\tau \to \infty$, we can check the bound proposed by Ashida [66], presented in section 2.3.3.

During one cycle of the engine with $\tau \to \infty$, a particle starts from equilibrium in potential $U(x; -L)$ and has a trajectory Γ up to time $t = 0$ where a reading is performed. The outcome of the measurement is $m = x(t = 0)$. The position of the center of the potential well in time is described by $\lambda(t)$ with:

$$\lambda(t < 0) = -L \tag{5.10}$$

$$\lambda(t > 0) = \begin{cases} -L & \text{if } m < 0 \\ +L & \text{if } m \geq 0 \end{cases} \tag{5.11}$$

This leads to two different protocols, presented in figure 5.18, λ_0 and λ_1 with:

$$\lambda_0(t) = -L \tag{5.12}$$
$$\lambda_1(t) = -L + 2L\theta(t) \tag{5.13}$$

with $\theta(t)$ the Heaviside step function.

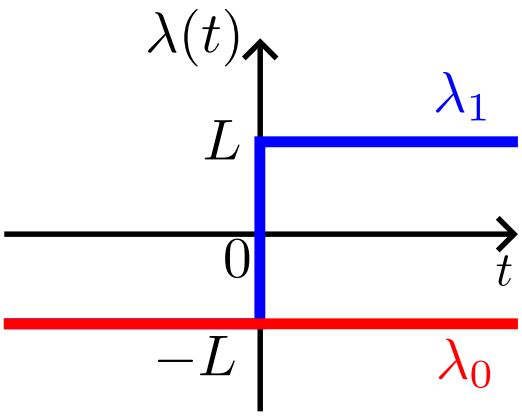

Figure 5.18: The two possible protocols if $\tau \to \infty$. The potential is initially centered in $-L$. At $t = 0$, the measurement is performed with outcome $m = x(t = 0)$. If $m > 0$, the potential is switch to $+L$, resulting in protocol λ_1. If $m < 0$ the potential is unchanged.

Our feedback measures the exact position of the particle x at each reading and the protocol is changed depending on this measurement. The result of the measurement is x itself. This leads to an extracted information $I(x) = -\log(P_{eq}(x; -L))$, where $P_{eq}(x; -L)$ is the probability of finding the particle at position x when measured. Since at each reading the system is at equilibrium in a harmonic potential centered in $-L$, $P_{eq}(x; -L) = \frac{1}{\sqrt{2\pi}} e^{-(x+L)^2/2}$. This gives an information:

$$I(x) = \frac{(x+L)^2}{2} + \log\left(\sqrt{2\pi}\right) \tag{5.14}$$

For a given measurement, different feedbacks can be applied, resulting in more or less work extraction depending on the smartness of the chosen protocol. In [66], Ashida and coworkers propose a way to quantify this amount of information I_u that is unused by the protocol. While they call it "unavailable information", our understanding of this concept leads us to call it "unused information". This unused information can be computed using the backward protocol. For a protocol $\lambda(t)$, its reverse protocol is $\lambda^\dagger(t) = \lambda(-t)$. The two possible reverse protocols are illustrated in figure 5.19. The unused information associated with a measurement x is

$$I_u(x) = -\log\left(\mathcal{P}\left(\Gamma^\dagger(t=0) = x | \lambda^\dagger = \lambda_i\right)\right) \tag{5.15}$$

where † notes the time reversal of a trajectory.

In the forward protocol, the measurement m imposes the protocol λ. The unused information I_u measures the reciprocity of this link and is measured by first imposing a protocol and then performing a measurement in the reverse process. If the outcome of the measurement is the same in both the forward and reverse processes, then it means that the link imposed between the measurement and the protocol is trivial and doesn't need a lot of information.

In the reverse protocol, since the protocols can differ before the measurement, causality prevents us from performing a feedback. A protocol is thus arbitrarily imposed. In the direct protocol, there are only two scenarios (center, non circled in figure 5.20.) :

- The particle is measured at $x < h$ and the applied protocol is λ_0.

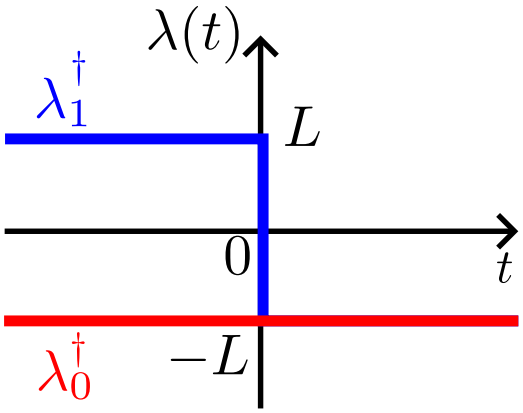

Figure 5.19: The two reversed protocols $\lambda_0^\dagger$ (red) and $\lambda_1^\dagger$ (blue). The potential is initially centered in $\pm L$ depending on the chosen protocol. The center of the potential is switched to $-L$ at $t = 0$ independently of any measurement outcome.

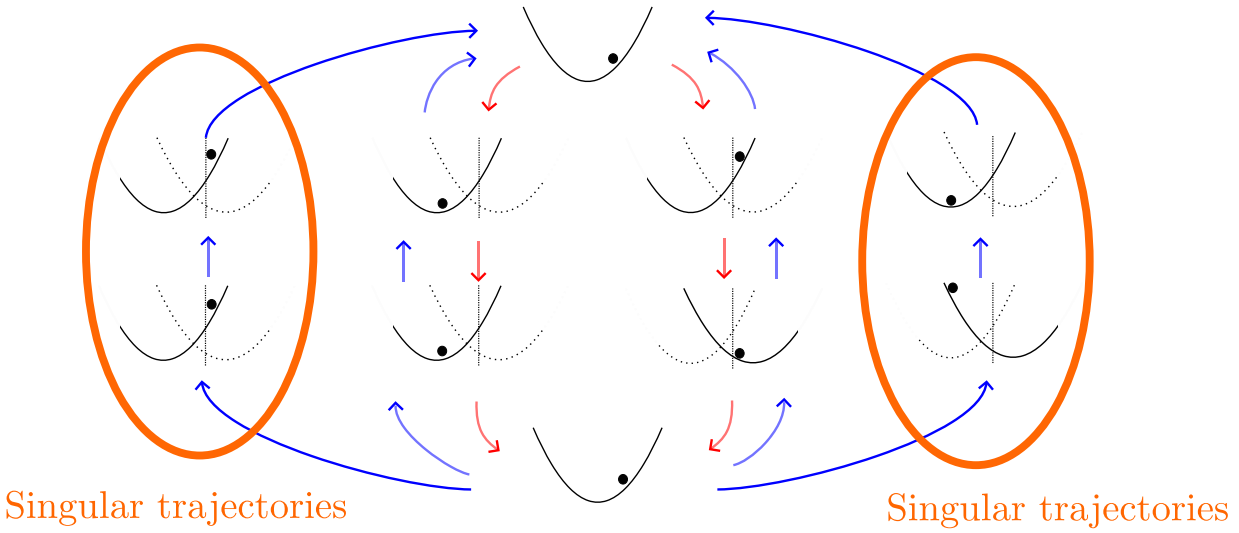

Figure 5.20: The different possible trajectories for the direct (red arrows) and reverse (blue arrows) protocols. Two types of trajectories, circled in orange, where the measurement does not correspond to the applied protocol, are only possible in the reverse protocol, without feedback, and are called singular trajectories.

- The particle is measured at $x > h$ and the applied protocol is λ_1.

In the backward protocol, the same trajectories, reversed can be obtained. Due to the absence of feedback new trajectories, called "singular trajectories" can appear (circled in figure 5.20). In our case, there are two kinds of singular trajectories :

- The applied protocol is λ_0 but the particle is measured in $x > h$. The potential is left unchanged while work extraction was possible.
- The applied protocol is λ_1 but the particle is measured in $x < h$. The potential is changed but this leads to negative work extraction (the feedback gives energy to the thermal bath).

The definition of I_u in equation 5.15 corresponds to measuring the probability of obtaining non singular trajectories, resulting in the same measurement, when performing the backward protocol.

For trajectories with protocol λ_0, $\mathcal{P}\left(\Gamma^\dagger(t=0) = x|\lambda^\dagger = \lambda_i\right) = \mathcal{P}_{eq}(x, -L)$ and $I_u(x) = \frac{(x+L)^2}{2} + \log\left(\sqrt{2\pi}\right)$. In this case, $I = I_u$ and $w = 0$. Therefore $w = I - I_u$.

For trajectories with protocol λ_1, $\mathcal{P}\left(\Gamma^\dagger(t=0) = x|\lambda^\dagger = \lambda_i\right) = \mathcal{P}_{eq}(x, +L)$ and $I_u(x) = \frac{(x-L)^2}{2}$. In this case, $I_u = \frac{(x+L)^2}{2} - 2Lx + \log\left(\sqrt{2\pi}\right)$. Using eq.5.1 and 5.14, we have $I_u = I - w$ and $w = I - I_u$.

With this discrete sampling protocol, for every trajectory, we have $w = I - I_u$. Therefore the generalised Jarzynski equality from [66], $\langle e^{w-I+I_u}\rangle = 1$, is satisfied. Furthermore, the bound $\langle w\rangle \leq \langle I - I_u\rangle$ is an equality.

To compare with experimental results, we compute $\langle I\rangle$ and $\langle I_u\rangle$:

$$\langle I\rangle = \int_{-\infty}^{+\infty} I(x)\mathcal{P}_{eq}(x; -L) \tag{5.16}$$

$$= \int_{-\infty}^{+\infty} \frac{(x+L)^2}{2} e^{-\frac{(x+L)^2}{2}} + \log\left(\sqrt{2\pi}\right) \tag{5.17}$$

$$= \frac{\sqrt{\pi}}{2} + \log\left(\sqrt{2\pi}\right) \tag{5.18}$$

Since $I(x)$ depends only on the reading performed on the equilibrium distribution, the position of the potential well has no impact and $\langle I\rangle$ is independent of L.

$$\langle I_u\rangle = \int_{-\infty}^{+\infty} I_u(x)\mathcal{P}_{eq}(x; -L) \tag{5.19}$$

$$= \int_{-\infty}^{0} \frac{(x+L)^2}{2} e^{-\frac{(x+L)^2}{2}} + \int_{0}^{+\infty} \frac{(x-L)^2}{2} e^{-\frac{(x+L)^2}{2}} + \log\left(\sqrt{2\pi}\right) \tag{5.20}$$

$$= \int_{-\infty}^{+\infty} \frac{(x+L)^2}{2} e^{-\frac{(x+L)^2}{2}} + \int_{0}^{+\infty} 2Lxe^{-\frac{(x+L)^2}{2}} + \log\left(\sqrt{2\pi}\right) \tag{5.21}$$

$$= \frac{\sqrt{\pi}}{2} - L^2 \operatorname{erfc}\left(\frac{L}{\sqrt{2}}\right) + L\sqrt{\frac{2}{\pi}} e^{-\frac{L^2}{2}} + \log\left(\sqrt{2\pi}\right) \tag{5.22}$$

Figure 5.21 shows the experimentally measured $\langle w\rangle$ as a function of L and the theoretical bound $\Delta I \equiv I - I_u$ resulting from earlier calculations. The information I is a bound for extracted work $\langle w\rangle$, measured experimentally, but this bound is very loose. The introduction of I_u, allows for a much tighter bound, taking into account the specificity of our feedback. The high discrepancy between I and ΔI means that our protocols don't use fully the information measured. However, the fact that the bound given by ΔI is saturated means that almost no work is lost when operating the system and that our description of the system is correct. Such an engine, where all the possible work is extracted, has been called a lossless information engine in previous literature and was already achieved in the case of overdamped systems [67].

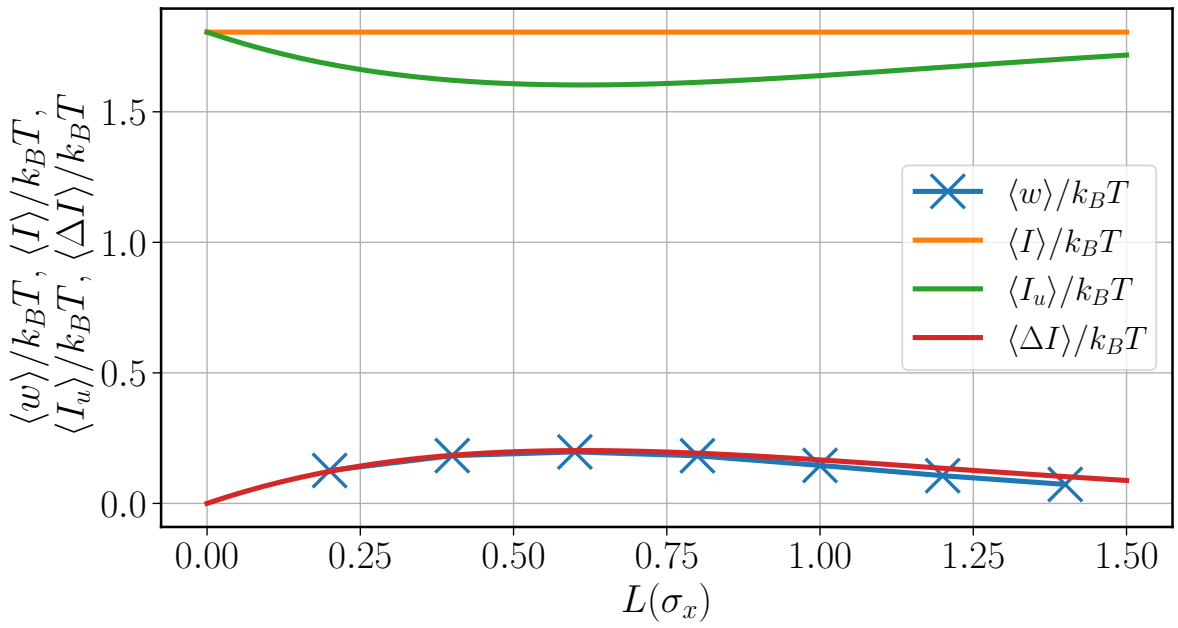

Figure 5.21: $\langle w\rangle, \langle I\rangle, \langle I_u\rangle$ as a function of L. The difference $\Delta I = I - I_u$ acts as a bound for w. In this protocol and considering the measurement result to be x itself, we get a saturation of the bound. ie: $\langle w\rangle = \langle \Delta I\rangle$.

5.7 Efficiency

We can try to define an efficiency for these information engines. However, many definitions, corresponding to different efficiencies seem interesting. We can first consider the efficiency of our experimental realisation : $\rho_{exp} = \frac{\langle w\rangle}{\langle \Delta I\rangle}$. This ratio measures the saturation of the bound $\langle w\rangle \leq \langle \Delta I\rangle$. $\rho_{exp} < 1$ indicates that some of the work is loss in the operation in the engine, due to dissipation. Another ratio can be consider: $\rho_{prot} = \frac{\langle \Delta I\rangle}{\langle I\rangle} = \frac{\langle I - I_u\rangle}{\langle I\rangle}$. This measures how efficiently the chosen protocol uses the information from the measurement. Taking into account both efficiencies corresponds to the ratio $\rho = \frac{\langle w\rangle}{\langle I\rangle}$. This ratio might be the more general one, and the closest to a usual efficiency in thermodynamics, as $\langle w\rangle$ is the useful quantity in a engine, and $\langle I\rangle$ is the amount of information that needs to be processed, thus resulting in a heat cost in the feedback due to Landauer's principle.

For our engine, $\rho_{exp} = 1$, as discussed in the previous section. We saturate the bound, $\langle w\rangle = \langle \Delta I\rangle$ and achieve a lossless information engine. From fig. 5.21, we get $\rho_{prot} \simeq 0.14$, which corresponds to the fact that our protocol used only a binary information from a very accurate measurement of the position. Since our engine is lossless, $\rho = \rho_{prot}$, and the efficiency of our engine is limited by the choice of protocols.

5.8 Conclusions

We have a precise measurement of x from which we control a rough protocol based on a binary choice. While a lot of information is extracted from the system, most of it is not used due to the simplicity of our protocol. The large discrepancy between I and ΔI in our experiment makes us think that a better protocol with lower unused information could be found and opens the question of the possibility of a protocol with $I_u = 0$ where all the information would be transformed into work. In the case of shorter τ, since the system doesn't fully relax, we cannot use the equilibrium distributions to compute I and I_u. Building an information in the regimes

from 5.4 and 5.5, taking into account the correlation between successive measurements is still an open question.

Chapter 6

Continuous sampling information engine

In the previous chapter, we are not able to define an information or unavailable information for shorter waiting times τ due to the measurements being performed on out-of-equilibrium systems. Here, we study a protocol where multiple measurements are implied, but the system starts from an equilibrium position. This makes it possible for us to define an information as well as an unavailable information, derive an extension of the Jarzynski equality from Crooks relation, and check our predictions experimentally.

In the protocol studied in the previous chapter, when a reading is performed, we wait a time τ independently of the outcome of the measurement. Here, instead of waiting a time τ if the threshold is not reached, we propose to sample continuously the position of the particle to catch it as soon as the threshold is reached. While the particle will always switch at the threshold, the time needed will be smaller.

Figure 6.1 shows an example of the effect of both protocols on a fictive trajectory. The trajectory starts at t_0 with a reading. In the case of the discrete feedback from chapter 5, a reading is performed again at $t = \tau$. If the particle crosses the threshold at $t_1 < \tau$, nothing will be done and the system will wait. Using a continuous sampling, the potential will be switched at $t = t_1$ and the time before the switching will always be smaller.

The protocol we propose here can also be seen as an intermediate to study information in the case of multiple measurements, while keeping the comfort of working with equilibrium distributions.

6.1 Feedback protocol

This protocol is a variation of the protocol presented in 5.1. As presented in figure 6.2, starting from equilibrium, the position of the particle x is sampled continuously until it reaches the threshold in h. At that point, the potential is instantaneously switched from $U(x; -L)$ to $U(x; L)$ and the feedback is locked for a time $\tau \gg t_{relax}$, letting the system go back to equilibrium, before performing a new cycle.

In this protocol, the measurements are done in quick succession. In this case, there are strong correlations between the different readings and information depends on the whole set of measurements rather than each individual reading.

A theoretical framework have been developed in collaboration with Christopher Jarzynski and Alberto Imparato and an article is in preparation.

We focus on full trajectories, starting at equilibrium in potential $U(x; -L)$. The particle evolves in a harmonic potential $U_\lambda(x)$, with $\lambda = A, B$. $U_A(x) = U(x; -L)$ and $U_B(x) = U(x; L)$. The position of the particle $x_0, x_1 ... x_M$ is measured at discrete times $t_n = n \times \delta t$. The position of

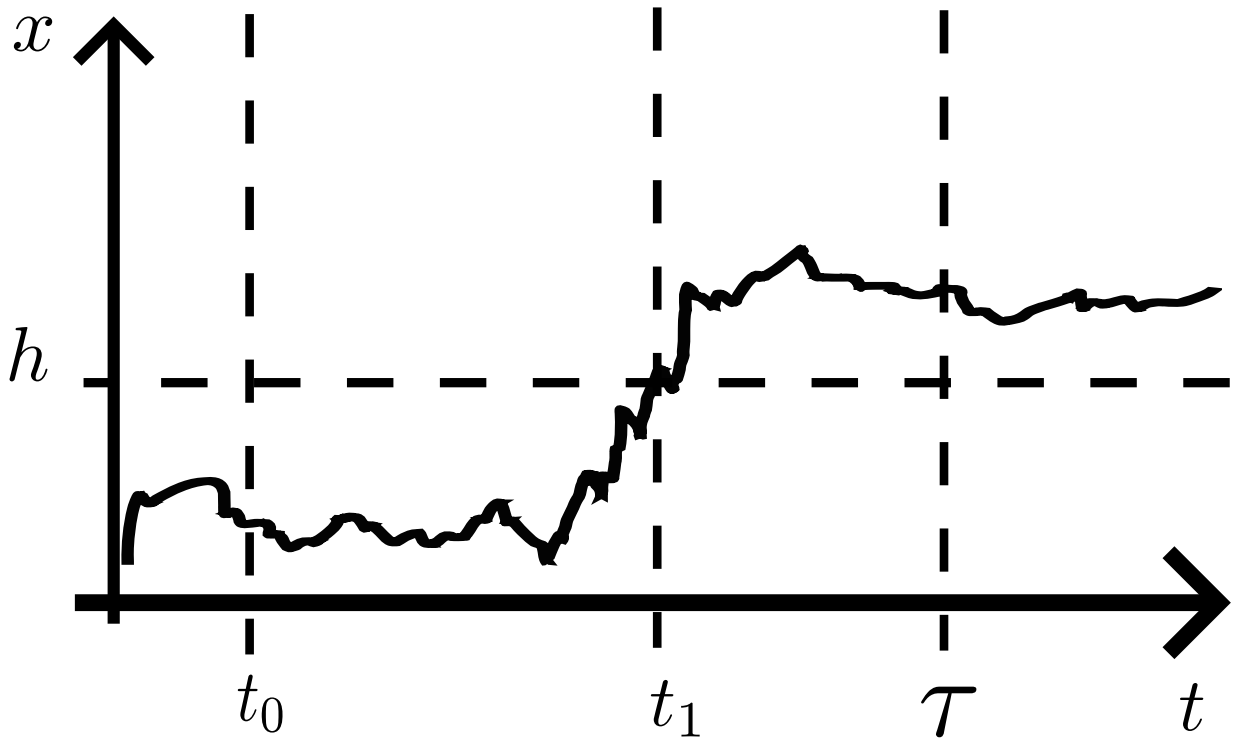

Figure 6.1: Example of a trajectory in the potential well. A reading is performed at t_0. Using the discrete sampling feedback, the position of the particle is read at $t = \tau$, and the potential will be switched. However, the particle first crossed the threshold at $t = t_1$. Using a continuous sampling, the switching happens at $t_1 < \tau$.

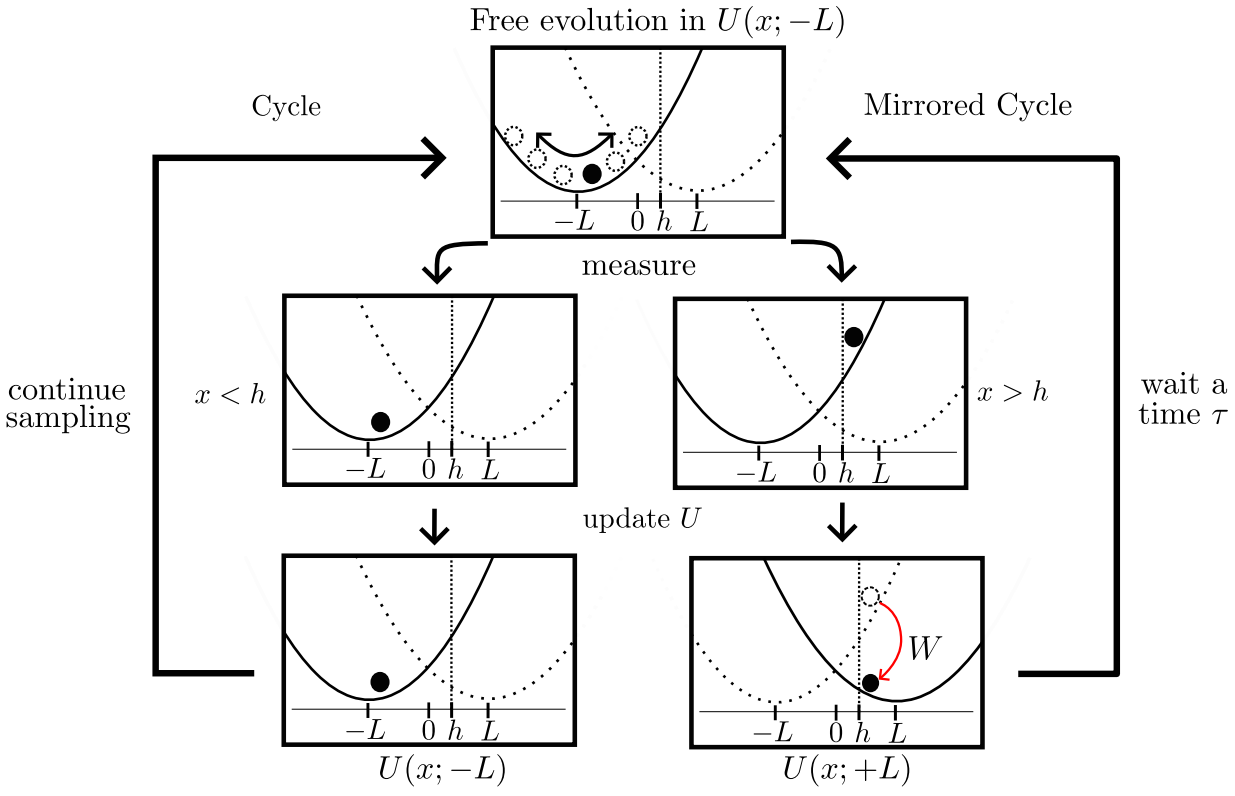

Figure 6.2: Continuous sampling protocol.

the particle is compared at each time step with a threshold h. At the first measurement where $x_n > h$, the control parameter λ is switched from A to B and is then kept at B independently of the following measurements. The final measurement is made at time t_M, long enough compared to all the other time scales of the system so the probability for the particle to reach the threshold during the measurements is 1.

This process has two outputs, a trajectory X and a protocol Λ.

$$X = (x_0, x_1, ..., x_M) \tag{6.1}$$
$$\Lambda = (\lambda_0, \lambda_1, ...\lambda_M) \tag{6.2}$$
$$\tag{6.3}$$

A protocol Λ is of the form:

$$\Lambda = (A, A... \underbrace{A}_{k^{\text{th}}\text{step}}, B, ...B) = \Lambda_k \tag{6.4}$$

with a sequence of k A's followed by $(M - k + 1)$ B's, determined by the first time k where $x_k > h$. We can group the trajectories in sets Ω_k containing all the trajectories crossing the threshold h for the first time at time t_k.

$$\Omega_k = \{X | \min\{i | x_i > h\} = k\} \tag{6.5}$$

The good parameter to describe the trajectories is k, the number of reading performed before the switching. This is the parameter that controls the protocols. Using this parameter we propose in the next section an information and an unavailable information, imposing a constraint on the extracted work.

6.2 Information

To build an information, we first study the joint probability between the trajectories X and the protocols Λ_k.

Let $P_{\text{FB}}(X, \Lambda_k)$ denote the joint probability to obtain trajectory X and protocol Λ_k when performing this process. We have that

$$P_{\text{FB}}(X, \Lambda_k) = 0 \quad \text{if } X \notin \Omega_k \tag{6.6}$$

We introduce P_k, probability of obtaining the protocol Λ_k:

$$P_k = P(\Lambda = \Lambda_k) \tag{6.7}$$
$$= \sum_X P_{\text{FB}}(X, \Lambda_k) = \sum_{X \in \Omega_k} P_{\text{FB}}(X, \Lambda_k) \tag{6.8}$$

Such that:

$$P_{\text{FB}}(X, \Lambda_k) = P_{\text{FB}}(X|\Lambda_k) P_k \tag{6.9}$$

We consider a different scenario where we choose beforehand a protocol Λ_k and apply it without feedback from the measured trajectory X and note $P_{\text{no}}(X|\Lambda_k)$ the probability of getting a trajectory X under protocol Λ_k without feedback.

A first result is that:

$$P_{\text{FB}}(X, \Lambda_k) = P_{\text{no}}(X|\Lambda_k) \quad \text{if} X \in \Omega_k \tag{6.10}$$

indeed, we can decompose $P_{\text{no}}(X|\Lambda_k)$ as:

$$P_{\text{no}}(X|\Lambda_k) = \pi_A(x_0) \cdot p_A(x_1|x_0) \cdots p_A(x_k|x_{k-1}) \cdot p_B(x_{k+1}|x_k) \cdots p_B(x_M|x_{M-1}) \tag{6.11}$$

where π_λ denotes equilibrium distribution in potential U_λ and $p_\lambda(x_i|x_{i-1})$ denotes the probability for the particle to be in x_i at time t_i after a measurement in x_{i-1} at time t_{i-1}, in potential U_λ. If $X \in \Omega_k$, the same decomposition can be done for $P_{\text{FB}}(X, \Lambda_k)$.

$$P_{\text{FB}}(X, \Lambda_k) = \pi_A(x_0) \cdot p_A(x_1|x_0) \cdots p_A(x_k|x_{k-1}) \cdot p_B(x_{k+1}|x_k) \cdots p_B(x_M|x_{M-1}) \tag{6.12}$$

In the case without feedback we introduce $q(l, k)$ the probability of obtaining a trajectory in Ω_l when imposing a protocol Λ_k:

$$q(l, k) = \sum_{X \in \Omega_l} P_{\text{no}}(X|\Lambda_k) \tag{6.13}$$

Defining $Q_k = q(k, k)$, we have by summing eq.6.10 over all $X \in \Omega_k$

$$P_k = Q_k \tag{6.14}$$

While $\{P_k\}$ is defined as a probability distribution, it is not trivial that $\{Q_k\}$ is a probability distribution without the result from eq. 6.14.

Given a protocol $\Lambda_k = (\lambda_0, \lambda_1 ... \lambda_M)$, let $\Lambda_k^\dagger = (\lambda_M ... \lambda_1, \lambda_0)$ denote the reverse protocol, and $P_{\text{no}}^R(X^\dagger|\Lambda_k^\dagger)$ the probability of getting a trajectory $X^\dagger$ when applying the reverse protocol without feedback. We define Q_k^R:

$$Q_k = \sum_{X \in \Omega_k} P_{\text{no}}(X|\Lambda_k) \tag{6.15}$$

$$Q_k^R = \sum_{X \in \Omega_k} P_{\text{no}}^R(X^\dagger|\Lambda_k^\dagger) \tag{6.16}$$

Q_k is the probability of getting a trajectory in Ω_k under protocol Λ_k without feedback. Q_k^R is the probability of getting the time reversal of a trajectory in Ω_k under protocol $\Lambda_k^\dagger$ without feedback. From Crooks' theorem [42] we have:

$$\frac{P_{\text{no}}(X|\Lambda_k)}{P_{\text{no}}^R(X^\dagger|\Lambda_k^\dagger)} = e^{-w(X,\Lambda_k)-\Delta F} \tag{6.17}$$

where $w(X, \Lambda)$ is the work performed by the system along a trajectory X under protocol Λ and ΔF is the free energy difference between potentials U_A and U_B. In our case, since U_A and U_B are the same up to a translation, $\Delta F = 0$.

For protocol Λ_k, we propose an information I_k:

$$I_k = -\log(P_k) \tag{6.18}$$

This information can be seen as the Shannon entropy of a unique measure on the duration of the protocol k. Since $P_k = Q_k$, we can also write $I_k = -\log(Q_k)$. To complement this information, we define an unavailable information $I_{u,k}$:

$$I_{u,k} = -\log\left(Q_k^R\right) \tag{6.19}$$

This definition of unavailable information is similar to the one used by Ashida [66] as it relies on the measurement in the reverse protocol of the probability of obtaining a measurement outcome corresponding to the protocol chosen beforehand. We define $\Delta I_k = I_k - I_{u,k}$, which can be written as:

$$\Delta I_k = -\log\left(\frac{Q_k}{Q_k^R}\right) \tag{6.20}$$

And we compute $\langle e^{w+\Delta F-\Delta I}\rangle_{FB}$:

$$\langle e^{w+\Delta F-\Delta I}\rangle_{FB} = \sum_{X,\Lambda_k} P_{\rm FB}(X,\Lambda_k)e^w \frac{Q_k}{Q_k^R} \tag{6.21}$$

$$= \sum_{\Lambda_k} \frac{Q_k}{Q_k^R} \sum_{X\in\Omega_k} P_{\rm no}(X|\Lambda_k)e^w \tag{6.22}$$

$$= \sum_{\Lambda_k} \frac{Q_k}{Q_k^R} \sum_{X\in\Omega_k} P_{\rm no}^R(X^\dagger|\Lambda_k^\dagger) \tag{6.23}$$

$$= \sum_{\Lambda_k} Q_k = \sum_{\Lambda_k} P_k = 1 \tag{6.24}$$

where we used results from eq.6.10, 6.14 and 6.17. This result is an extension of the Jarzynski equality [33] in the case of feedback protocols. We test experimentaly this result in the next section.

We can also notice that for all protocol Λ_k:

$$\langle e^w\rangle_k = \sum_X P_{\rm FB}(X|\Lambda_k)e^w = \sum_{X\in\Omega_k} P_{\rm FB}(X|\Lambda_k)e^w \tag{6.25}$$

$$= \frac{1}{P_k}\sum_{X\in\Omega_k} P_{\rm FB}(X,\Lambda_k)e^w = \frac{1}{P_k}P_{\rm no}(X|\Lambda_k)e^w \tag{6.26}$$

$$= \frac{1}{P_k}\sum_{X\in\Omega_k} P_{\rm no}^R(X^\dagger|\Lambda_k^\dagger) = \frac{Q_k^R}{P_k} = \frac{Q_k^R}{Q_k} = e^{\Delta I_k} \tag{6.27}$$

Averaging eq.6.25 over all values of k, we also get:

$$\langle e^w\rangle = \sum_k P_k\langle e^w\rangle_k \tag{6.28}$$

$$= \sum_k P_k e^{\Delta I_k} \tag{6.29}$$

$$= \langle e^{\Delta I}\rangle \tag{6.30}$$

which is a different result from eq.6.21.

In this protocol we can distinguish two cases: $k = 1$ and $k > 1$. For all trajectories with $k > 1$, the potential will be switched when the particle is right at threshold h and the work extracted is therefore $w_0 = 2Lh$. This leads to $\langle e^w\rangle_k = e^{2Lh}$ for all values of k. Therefore, by eq. 6.25, I_k is independent of the length of the trajectory and $\Delta I_k = 2Lh$ for all $k > 1$.

In the following we test experimentally the two main results we derived here, by separating between the cases $k = 1$ and $k > 1$.

6.3 Experimental test

We perform experiments with a sampling frequency of 100 MHz, giving $\delta_t = 10$ ns, with $\tau = 16t_0$ so each trajectory starts at equilibrium, and varying L and h.

For each trajectory, we measure the work w extracted from the system. The probability distribution of w over a trajectory is shown in figure 6.3, for $L = 0.6$ and $h = 0.25$. We notice a pdf similar to the ones from chapter 5, with a strong peak and a tail $w > 0$. In chapter 5 the peaks correspond to individual readings below the threshold leading to no work extraction because the potential is unchanged. Here, the peak corresponds to trajectories starting from

$x_1 < h$. These trajectories are sampled continuously, similarly to section 5.5, and the potential is switched from U_A to U_B as soon as the threshold h is reached with an extracted work $w_0 = 2Lh$.

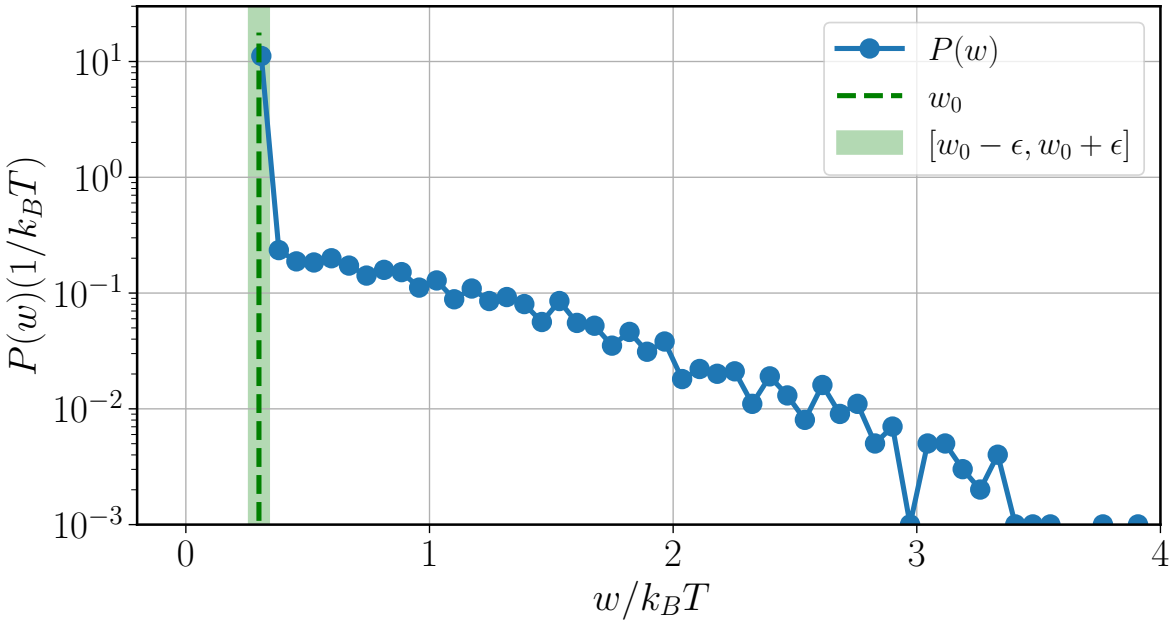

Figure 6.3: Probability distribution functions of work over trajectories $P(w)$, for $L = 0.6$ and $h = 0.25$. The green dashed line indicates w_0. The peak in the pdf is located around the predicted value for w_0. A tolerance window is allowed around w_0 in our analysis and corresponds to the shaded area.

We sort trajectories based on the value of w: If $w \simeq w_0$, this corresponds to a trajectory with $k > 1$. For these trajectories, since $\Delta I_k = 2Lh$, $w = \Delta I_k$ and $e^{w-\Delta I_k} = 1$. Experimentally, we need to check that $w = w_0$. This can be seen on the pdf shown on figure 6.3. We notice that there is indeed a peak in the pdf located close to the predicted value for w_0 (green vertical line). Since the data are experimental, we need to take a tolerance ϵ around w_0 to count an event as an event where $w = w_0$. This tolerance is shown by the shaded area on figure 6.3. This tolerance is adjusted to include the peak of the pdf to a value of $\epsilon = 0.05 k_B T$.

If $w \neq w_0$, this corresponds to a trajectory with $k = 1$. In this case, $e^{w+\Delta I_1} \neq 1$ for most trajectories. In this case we can compute ΔI_1 and check experimentally that $\langle e^w \rangle|_{k=1} = e^{\Delta I_1}$, where w is measured and ΔI_1 computed from our predictions. We can compute $\Delta I_1 = -\log\left(\frac{Q_1}{Q_1^R}\right)$ by first computing Q_1 and Q_1^R.

$$Q_1 = P_1 = P(x_1 > h) = \int_h^{+\infty} \pi_A(x)dx \tag{6.31}$$

$$= \int_h^{+\infty} \frac{1}{\sqrt{2\pi}} e^{\frac{(x+L)^2}{2}} dx = \sqrt{\frac{\pi}{2}}\,\mathrm{erfc}\left(\frac{h+L}{\sqrt{2}}\right) \tag{6.32}$$

$$Q_1^R = P(X^\dagger \in \Omega_1 | \Lambda_1^\dagger) = \int_h^{+\infty} \pi_B(x)dx \tag{6.33}$$

$$= \int_h^{+\infty} \frac{1}{\sqrt{2\pi}} e^{\frac{(x-L)^2}{2}} dx = \sqrt{\frac{\pi}{2}}\,\mathrm{erfc}\left(\frac{h-L}{\sqrt{2}}\right) \tag{6.34}$$

$$\Delta I_1 = -\log\left(\frac{Q_1}{Q_1^R}\right) = -\log\left(\frac{\mathrm{erfc}(\frac{h+L}{\sqrt{2}})}{\mathrm{erfc}(\frac{h-L}{\sqrt{2}})}\right) \tag{6.35}$$

We then need to check that $\langle e^w \rangle_{k=1} = e^{\Delta I_1}$. Figure 6.4 shows the experimentally measured $\langle e^w \rangle$, averaged over all the values of w where $\neq w_0$, as a function of L, for $h = 0.25$. We also plot $e^{\Delta I_1}$ predicted from eq. 6.35. We can see that the two curves are close, which confirms that $\langle e^w \rangle|_{k=1} = e^{\Delta I_1}$. From that and the fact that $w = w_0$ for $k > 1$, we can conclude that $\langle e^w \rangle|_k = e^{\Delta I_k}$ for all k. This implies that both results from eq. 6.21 and 6.28 are valid for our experiment. To illustrate this result, we measure in figure 6.5 $\langle e^{w-\Delta I} \rangle$ for different values of L and h. The four curves are close to 1, as predicted from eq.6.21.

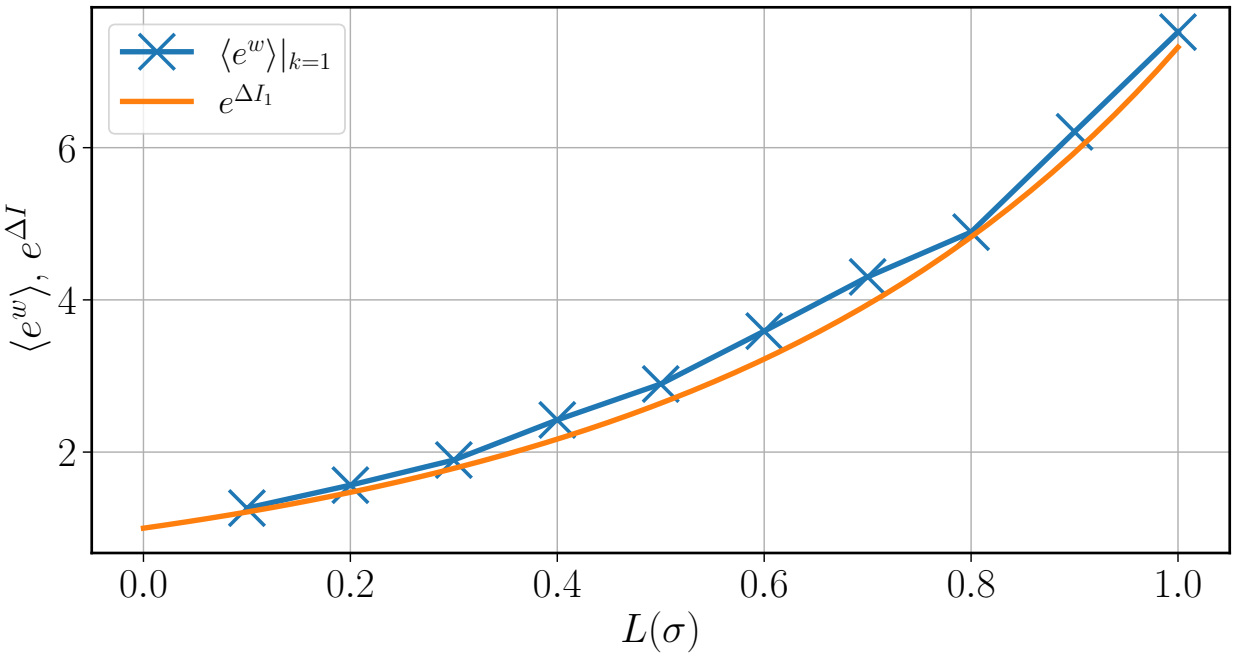

Figure 6.4: $\langle e^w \rangle$ for $k = 1$ measured experimentally (blue), compared with the prediction for $e^{\Delta I_1}$ in the case $h = 0.25$. The two curves are close, which implies that $\langle e^w \rangle|_{k=1} = e^{\Delta I_1}$.

The choice of the tolerance ϵ is crucial in the analysis. Indeed, it is the parameter used to sort between events where $k > 1$ and $k = 1$. Figure 6.6 shows a distribution of work with the windows corresponding to $\epsilon = 0.5 k_B T$, $\epsilon = 0.05 k_B T$, and $\epsilon = 0.005 k_B T$. We perform the same analysis as before to compute $\langle e^{w-\Delta I} \rangle$ as a function of L, for $h = 0.25$, using the different values of ϵ presented in figure 6.6, and report the result in figure 6.7. For values of ϵ too small, $\langle e^{w-I} \rangle$ is underestimated, whereas for higher values $\langle e^{w-\Delta I} \rangle$ is overestimated.

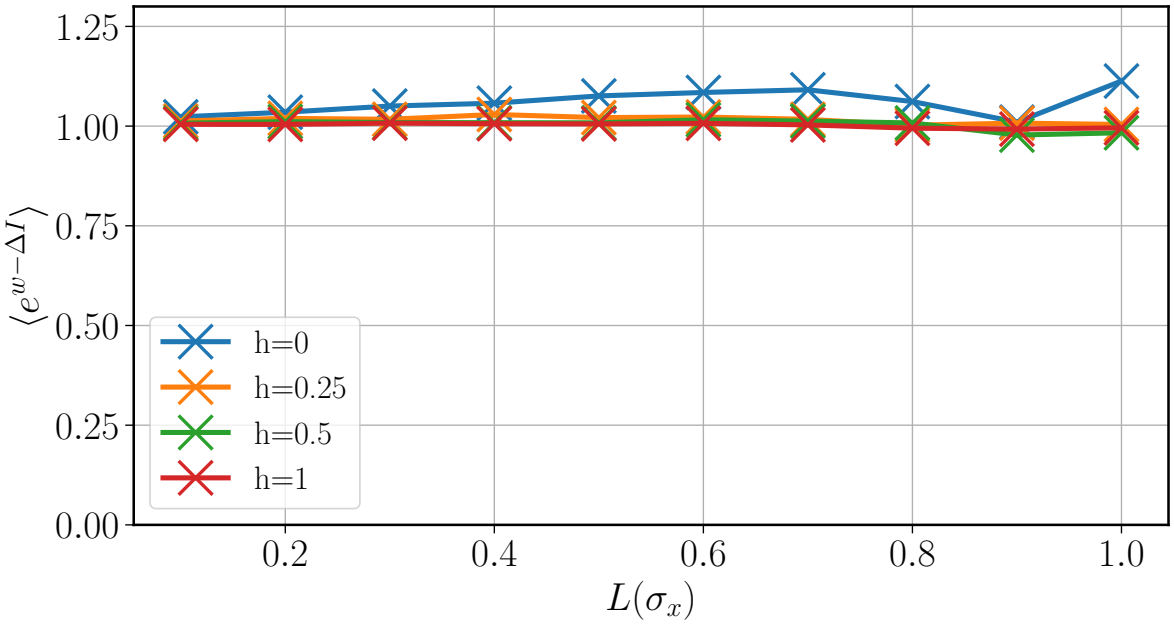

Figure 6.5: $\langle e^{w-\Delta I} \rangle$ as a function of L for different values of h. As predicted by eq.6.21, the curves are close to 1 for all values of L and h.

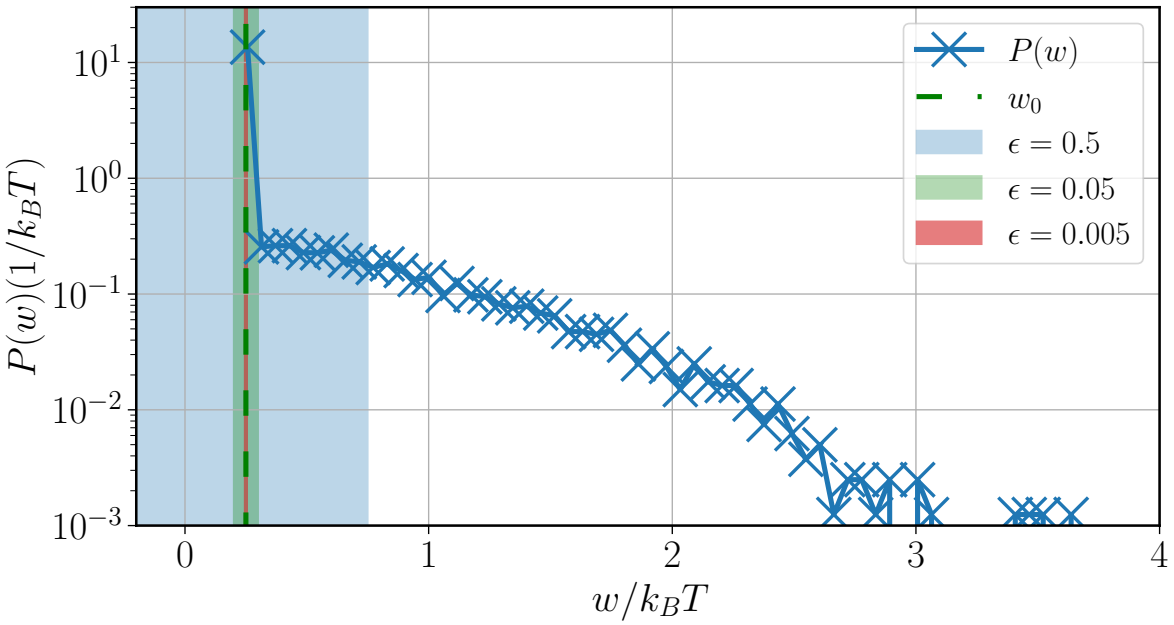

Figure 6.6: The probability distribution of work $P(w)$ for $L = 0.6$ and $h = 0.25$. Different tolerance windows around w_0 are indicated. Blue shade: $\epsilon = 0.5k_BT$, green shade: $\epsilon = 0.05k_BT$, red shade: $\epsilon = 0.005k_BT$.

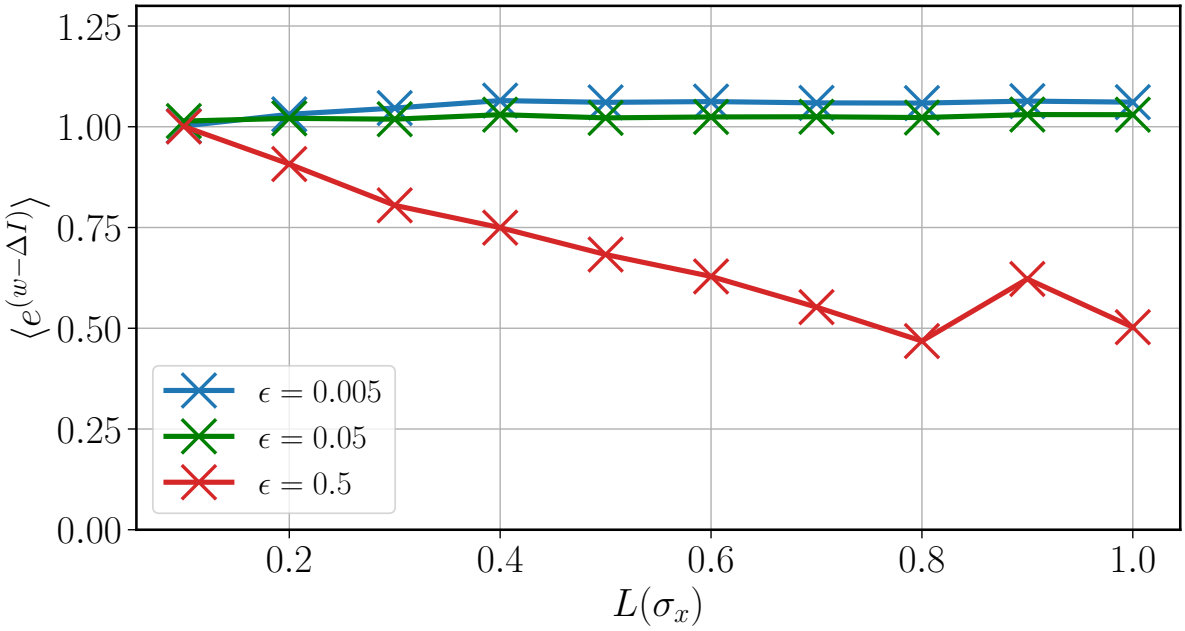

Figure 6.7: $\langle e^{w-\Delta I} \rangle$ for $L = 0.6$ and $h = 0.25$ using different values for ϵ in the analysis.

6.4 Conclusions

We study a protocol where multiple measurements are involved, with correlations between them. By identifying a quantity that gather all the information about the protocol and the measurements, k, we are able to define an information and an unavailable information, in a way coherent with the literature. Using this observable, containing all the information about the protocols, we are able to derive a generalisation of the Jarzynski equality (proposed in eq. 6.21), as well as a corollary result (proposed in eq. 6.28). Using the setup from 3 and adapting the feedback used in 5, we confirm experimentally our predictions. Building an efficiency in this case can be theoretically done in the same fashion as in 5.7. However, experimentally measuring the whole distribution $P(k)$ is a challenge, as we work with high sampling frequency, thus too many possible values for k. Reducing the sampling frequency could allow us to access the distribution of times $P(k)$, at the cost of reducing our accuracy when measuring the work exchanged.

Chapter 7

Velocity controlled Feedback: The Maxwell Demon

In this chapter, we present preliminary results on a configuration of our setup where we use the feedback loop to create a Maxwell Demon, similar to the one originally described by Maxwell [68]. In his book, Maxwell studies the case of an observer that can measure the position and speed of individual particles of a gas in a box. By operating a trapdoor in the middle of the box, this observer can sort the particles between the "hot" ones, with high velocities, on one side and the "cold" ones, with low velocities, on the other. Such an observer is able to create a temperature difference from an isolated system with homogeneous properties, without performing work. The Maxwell Demon has been a fascinating concept in physics for the last century [45, 46, 69]. Many experiments aimed to reproduce in the lab a Maxwell Demon, a device able to extract work from a monothermal source. A lot of different systems have been used, such as quantum systems [70], photonics [71–73], electronics [74–78], active systems [79], dimers [52], complex molecules [80], DNA hairpins [81] or using macroscopic systems [82].

The term "Maxwell Demon" is now used in a broad sense for any device where work is extracted by rectifying the thermal fluctuations. In previous chapters, we preferred the term information engine, to highlight the role of the measurement and to distinguish from Maxwell thought experiment, where the entropy of a system is lowered while it has no work or heat exchange with its environment. Using our setup presented in chapter 3, we can now reproduce experimentally what was first presented as a thought experiment by Maxwell.

7.1 Proposed protocol

To reproduce a Maxwell Demon in our experiment, we change the logic of the feedback loop. We need an equivalent of the trapdoor to separate space in two subdomains and a measurement of speed to control the trapdoor. Our experiment only allows us to work with a single particle. We propose a protocol that creates a Maxwell Demon on the statistic of this single particle in time, instead of using ensemble statistics on many particles.

In this protocol, presented in figure 7.1, the particle is trapped in an harmonic potential $U(x; x_0) = \frac{1}{2}k(x - x_0)^2$ where x_0 can only take two values: $\pm L$. The position of the particle x is sampled continuously. The protocol is the following:

- Each time the particle is at $x = 0$, the velocity of the particle v is measured.
- The position of the potential is adjusted depending on v and a set threshold v_0:
  - If $|v| < v_0$, the center of the potential is set to $x_0 = -L$.
  - If $|v| > v_0$, the center of the potential is set to $x_0 = +L$.

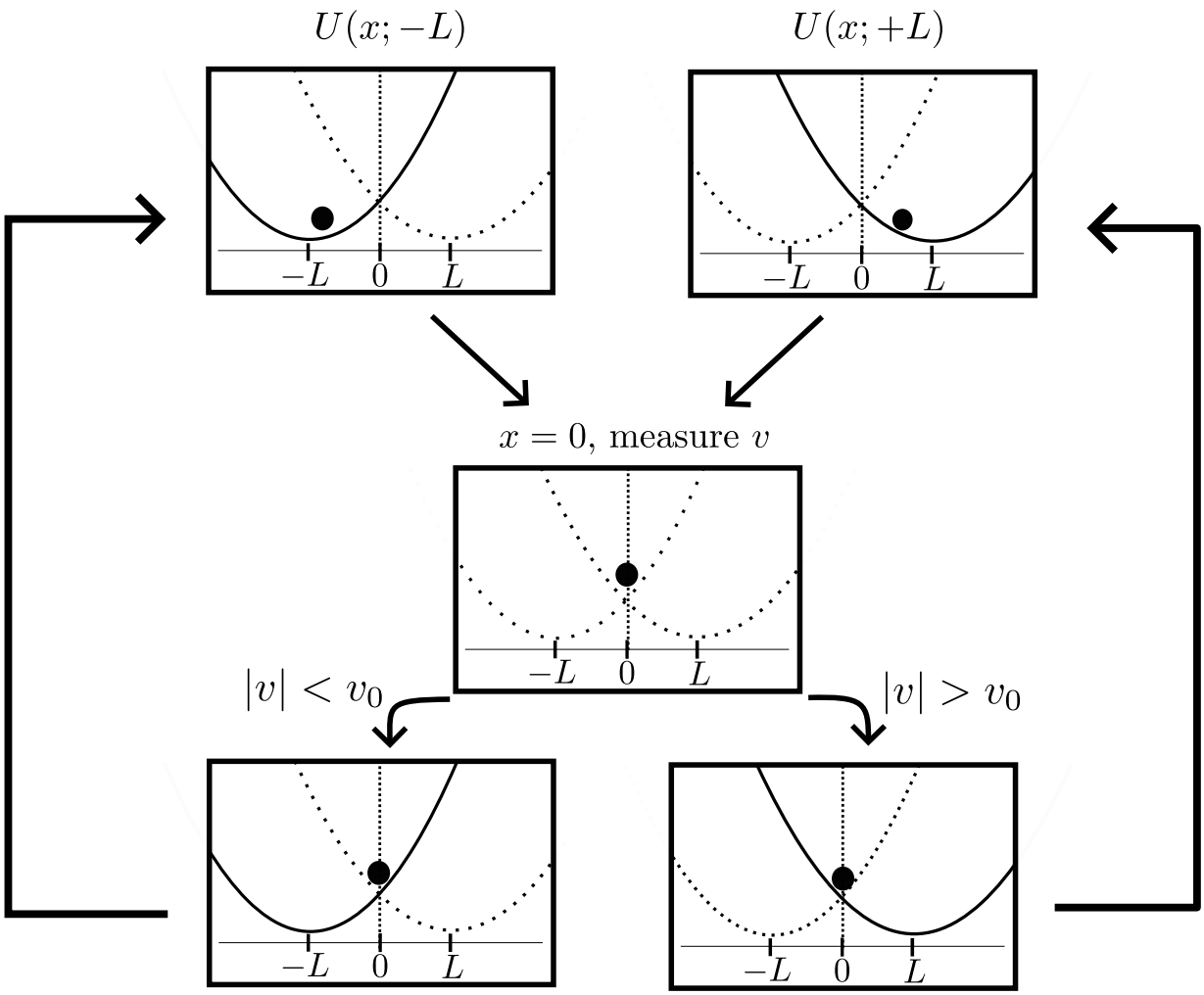

Figure 7.1: The protocol used to reproduce a Maxwell Demon. The position of the particle is sampled continuously. When the particle reaches $x = 0$, its speed v is compared to a set threshold v_0. If $v < v_0$, the position of the potential well is then set to $x_0 = -L$, else the potential is set to $x_0 = +L$.

- The sampling of the position of the particle continues.

In Maxwell's original thought experiment, the particle is trapped in a box, which can be model as an infinitely steep potential. Here we use a softer harmonic potential. While the particle is not as strongly confined to a region of space, this version is adapted to our experimental setup, where the particle is harmonically trapped by the stiffness of the cantilever.

This protocol correlates the position of the particle x and its velocity v by creating a region of space where on average the velocity of the particle is higher. We expect the velocity to be lower in the left potential well, which will be a cold well, and to be higher in the right well, which will be a hot well.

An important point in Maxwell's proposition is that the demon should not produce any work on the system. In our protocol, when the potential is switched, the variation of potential energy in the system is $\Delta U = 2Lx$. For an instantaneous change in the potential, no heat is exchanged with the thermal bath and $q = 0$ and the work performed is $w = \Delta U = 2Lx$. Since the feedback operates only when $x = 0$, we expect no work to be performed by the feedback on the particle.

7.2 Experimental Implementation

We use the setup presented in chapter 3, by setting the feedback loop to perform the aforementioned protocol. Experimentally, the position of the particle x is sampled at 100 MHz. The position is filtered using an IIR low-pass filter, presented in 3.3, set at 50 kHz. This limits the contribution of high order modes of the cantilever and high frequency noise. The velocity is computed by taking the discrete derivative of the position. The n-th sample of velocity v_n is then computed by the feedback as:

$$v_n = f_s(x_n - x_{n-1}) \tag{7.1}$$

where f_s is the sampling frequency and subscript n denotes the n-th sample, taken at time n/f_s. Since the contribution of higher frequencies is amplified by the derivation, the filtering used for the velocity is more restrictive. An IIR low-pass filter at 8 kHz is used on the position signal before computing the velocity.

The harmonic trapping is created by the stiffness of the cantilever and the center of the trap x_0 can be set to $\pm L$ by applying a constant feedback voltage $\pm V_{FB}$. Since we are not performing a continuous sampling but are limited by our acquisition frequency, we will never measure exactly $x = 0$. We therefore detect crossing by looking for change of sign in the deflection x.

When analysing the data from the experiment, the first 100 ms are discarded. This corresponds to 10 periods of the oscillator and ensures that we are working in the steady state of the demon. An example of experimental signals obtained is shown in figure 7.2. The upper figure represents the position of the particle x and the position of the center of the trapping potential x_0 during the experiment. Each time the particle crosses $x = 0$, denoted by the green crosses, the velocity of the particle is read by the feedback. The velocity during the experiment is shown on the bottom figure. Green crosses indicate the velocity at each event $x = 0$. At these points, the value of the potential center is adjusted. If $|v| < v_0$, the potential is set to $x_0 = -L$, else the potential is set to $x_0 = +L$. Since the feedback only updates the potential when $x = 0$, we can have $x_0 = -L$ (the particle is in the "cold" well), while $|v| > v_0$ or conversely.

We measure the position of the particle for a total of 10 s in the steady state of the demon. For this experiment, we use $L = 1\,\sigma_x$, with σ_x the standard deviation of the position at equilibrium without the demon, as measured in chapter 3. The threshold in velocity is set to $v_0 = 1\,\sigma_v$, with $\sigma_v = \sigma_x 2\pi f_0$ the standard deviation of velocity at equilibrium without the demon, computed from σ_x and f_0, the frequency of the oscillator extracted from the SHO fit presented in chapter 3. By sorting the positions and velocities in two sets based on the value of x_0 to distinguish between the two potential wells, we can obtain the distribution of positions and speeds in each well. These distributions are shown in figure 7.3 and 7.4.

We can see on figure 7.3 the distribution of positions in the two potential wells. The distribution in the well centered in $x_0 = +L$ is wider than for $x_0 = -L$. This is coherent with our expectation of a hot well in $+L$ and a cold well in $-L$. Since the demon is operating, the system is in an non-equilibrium steady state (NESS) and a temperature cannot be properly defined. We can however access an effective temperature and compute the ratio of these temperatures in the wells.

At equilibrium, the temperature can be measured as $T = \frac{k\sigma_x^2}{k_B}$ using equipartion theorem. For a NESS, we can define an effective temperature T_x as

$$T_x = \frac{k\,\mathrm{var}(x)}{k_B} \tag{7.2}$$

In our experiment, this gives $T_x^C = (196 \pm 6)$ K for the cold well and $T_x^H = (425 \pm 12)$ K for the hot well. We can also access the temperature ratio as the ratio of the variance of the position

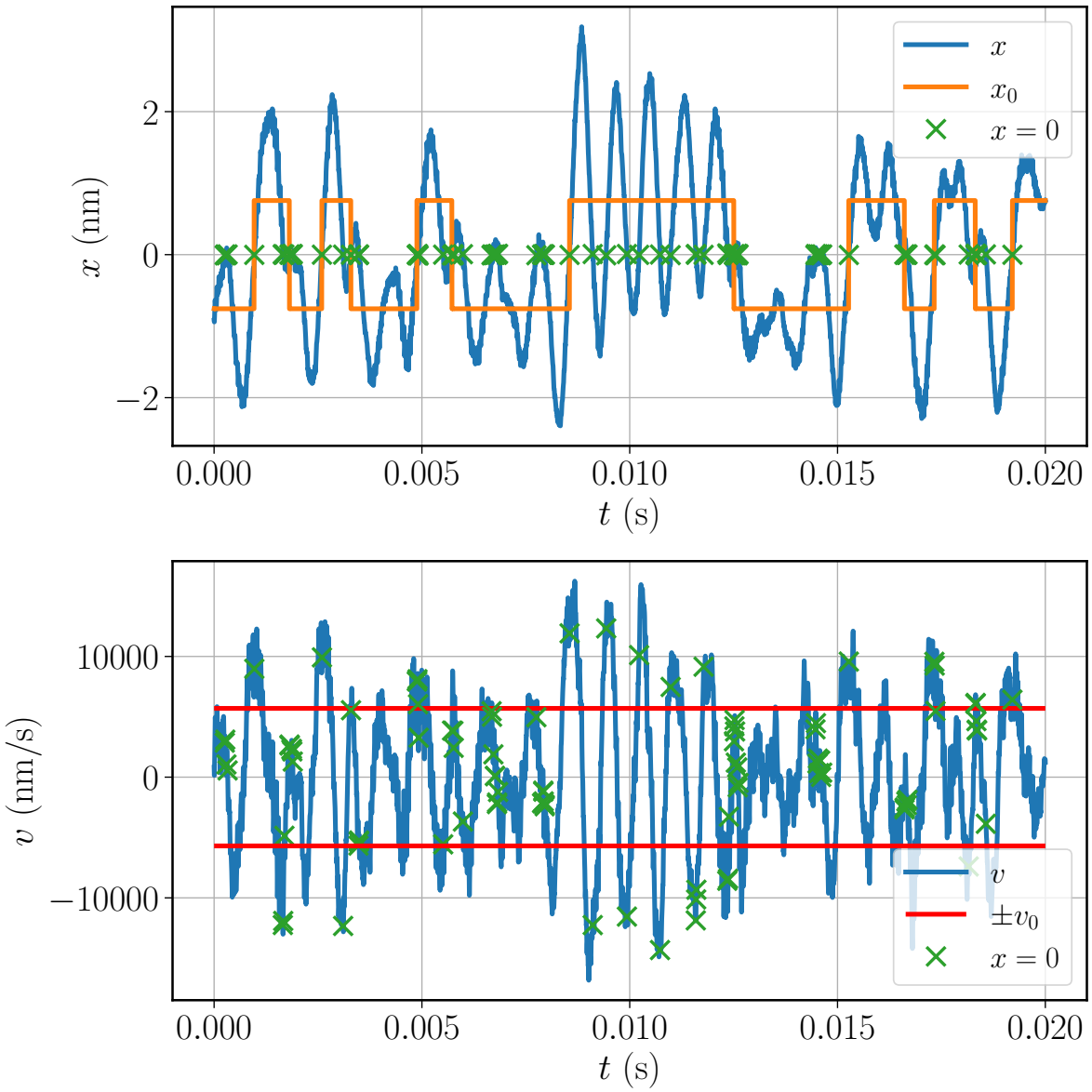

Figure 7.2: Example of trajectory obtained in the steady state of the demon. Top figure: Blue: position of the particle x. Orange: Position of the center of the potential x_0. Green crosses indicate the moments when x crosses 0. Bottom figure: Blue: Velocity of the particle. Red: Threshold v_0. Green crosses indicates the velocities measured when $x = 0$.

in each well. This measurement is independent of any equilibrium calibration. We obtain a temperature ratio of 2.1 ± 0.1.

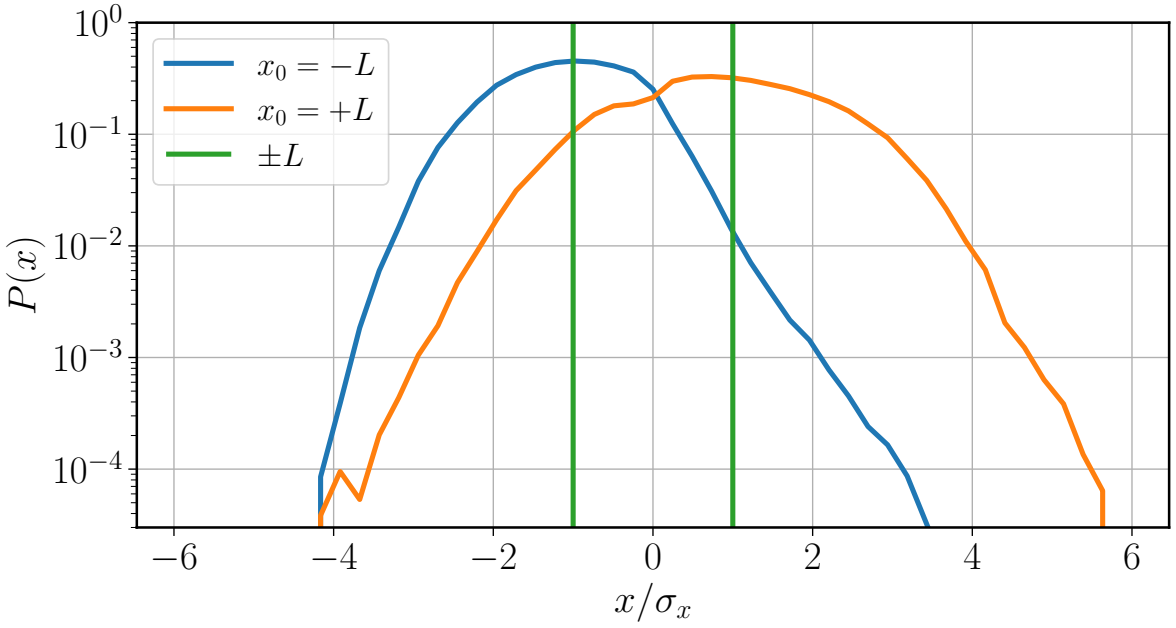

Figure 7.3: Probability distribution of x for both potential wells. The blue curve corresponds to the well centered in $x_0 = -L$. The orange curve corresponds to the well centered in $x_0 = +L$. The distribution in the right well is wider, corresponding to a hot well.

We can perform the same analysis on the distribution of speeds, presented in figure 7.4. We can see that the distribution is wider in the well centered in $x_0 = +L$, as for the position. This reinforce the interpretation of $x_0 = +L$ as a hot well, while $x_0 = -L$ is a cold well.

At equilibrium, the temperature is linked to the distribution of speeds by $T = \frac{m\sigma_v^2}{k_B}$, using again the equipartition theorem. We can adapt this definition to NESS to get an effective kinetic temperature as

$$T_v = \frac{m \operatorname{var}(v)}{k_B} \tag{7.3}$$

We obtain $T_v^C = (204 \pm 6)\,\mathrm{K}$ for the cold well and $T_v^H = (443 \pm 13)\,\mathrm{K}$ for the hot well. We can again compute a temperature ratio, independent of the equilibirum calibration. This ratio for kinetic temperature is 2.2 ± 0.1.

The kinetic temperature measured is within the uncertainty margins of the position temperature. Using the temperature ratios, independent from any calibration, gives a closer agreement between kinetic and position temperature. However, as the system is out of equilibrium there is no reason for the temperature of all degrees of freedom to be the same.

We can therefore operate a Maxwell Demon, separating high and low velocities in space, creating a hot domain and a cold domain. While the system is out of equilibrium, we can define an effective temperature from the distributions of speeds or positions. In both case, the experimental results confirm that we have indeed two regions of space, one hot and one cold, with a temperature ratio of about 2. To confirm that the demon is indeed working properly, we need to look at the statistics of work and heat in the steady state.

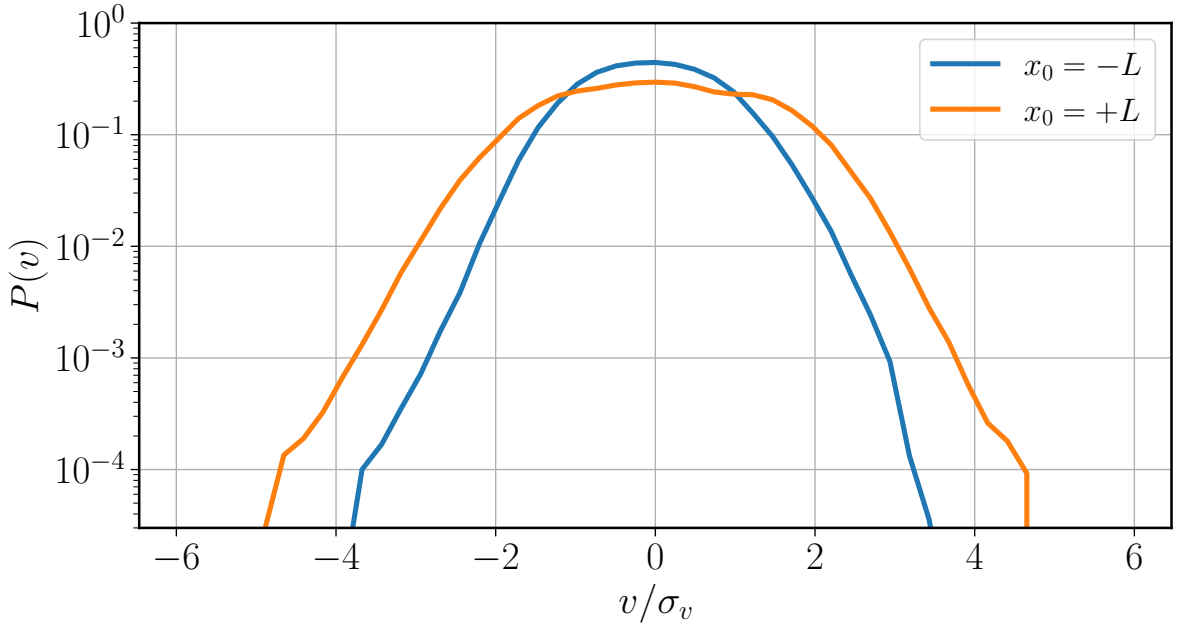

Figure 7.4: Probability distribution of v for both potential wells. The blue curve corresponds to the well centered in $x_0 = -L$. The orange curve corresponds to the well centered in $x_0 = +L$. The distribution in the right well is wider, corresponding to a hotter well.

7.3 Distribution of heat and work

A Maxwell Demon is supposed to act without performing work on the system. To confirm that we have achieved a Maxwell Demon, we need to study the exchange of heat and work with the system during the operation of our Demon.

From the time trace of speed and position in the steady state, we can reconstruct the instantaneous heat given by the bath to the system $\dot{q}$ and work $\dot{w}$ performed by the demon on the system during operation of the demon, using the method presented in 3.4 and already used in chapters 5 and 6.

The probability distributions of work when $x_0 = -L$ or when $x_0 = +L$ are shown in figure 7.5. The power, $\dot{w}$, is represented in units of k_BT/t_{relax}, with t_{relax} the relaxation time of the oscillator. This allows us to use the natural timescales and energy scales of the system. In both cases, the distribution has a peak in $w = 0$, because most of the time x_0 is constant, the potential is fixed, and no work is performed on the system. When the potential is changed from $\pm L$ to $\mp L$, the work done on the system is $w = \pm 2Lx$. The spread of the probability distribution is then due to the latency of the feedback when measuring the crossing at $x = 0$. The wider distribution in the hot well can be explained by the larger speed, thus latency, when switching to this well. From these distributions we can also compute the mean work performed by the demon on the system. We found a mean power $\langle \dot{w} \rangle^C = (0.7 \pm 0.02) k_BT/t_{relax}$ for the cold well and $\langle \dot{w} \rangle^H = (-0.04 \pm 0.02) k_BT/t_{relax}$ for the hot well. In the case of the cold well, 0 is not in the uncertainty interval. This can come from a systematic error, for example in the calibration of the position of the center of the potential at rest, $x = 0$. However, both values of work are small compared to the typical energy scale of the system, which means that our demon performs negligible work on the system.

We can also look at the distributions of heat for both potential wells. This heat is exchanged from the thermal bath to the system at room temperature (295 K). The spread of both distributions is more than a hundred time larger than for work. We can compute the average heat flux in the cold and the hot wells. For the cold well we get a mean heat flux $\langle \dot{q} \rangle^C = (4.6 \pm 0.1) k_BT/t_{relax}$.

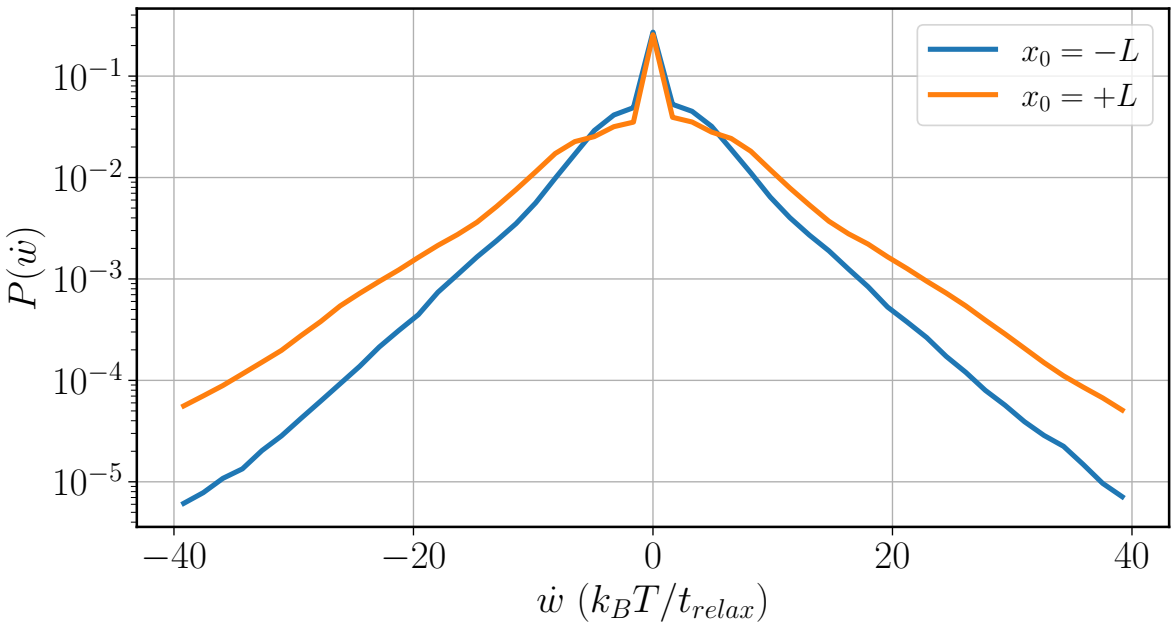

Figure 7.5: Probability distributions of instantaneous work $\dot{w}$ in the steady state of the experiment for both well. A peak in $\dot{w} = 0$ comes from all the moment where x_0 in unchanged. The rest of the pdf has a spread due to the latency of the feedback, resulting in a distribution of positions around 0 when the potential is switched.

While for the hot well we get a mean heat flux $\langle \dot{q} \rangle^H = (-6.4 \pm 0.1) k_B T / t_{relax}$. On average, the thermal bath heats the particle in the cold well and cools the particle in the hot well. We can notice that the two fluxes don't cancel each other. There is no reason that the particle spends as much time in the cold well as in the hot well. Experimentally, we measure the particle to be 55% of time in the cold well. To take into account this asymmetry in the occupation times, we can compute the mean heat flux on the whole data set and we obtain $\langle \dot{q} \rangle = (-0.3 \pm 0.1) k_B T / t_{relax}$. This heat flux is very small compared to the typical fluctuations in the distribution. We can similarly compute the mean work performed on the system and obtain $\langle \dot{w} \rangle = (0.4 \pm 0.1) k_B T / t_{relax}$. Since we are studying a steady state, the heat flux is compensating the work given to the system by the feedback.

7.4 Overall distributions and role of the demon

To understand exactly the effect of the demon on the system, we can look at the overall distributions for positions and velocities, obtained without conditioning on the value of x_0. These distributions can be compared to equilibrium distributions to see how the demon affects the system.

We first look at the distribution of position in the current potential well, $P(x(t) - x_0(t))$. The distribution is shown on the blue curve in figure 7.7. The distribution looks gaussian, centered in 0. The variance of the position can be computed and is found to be $\mathrm{var}(x) = 1.02\sigma_x^2$, very close to the equilibrium value. To check that the gaussian distribution is a good description of $P(x - x_0)$, we superimpose in figure 7.7 a curve $e^{-\frac{(x-x_0)^2}{2\mathrm{var}(x)}}$. The overall distribution of positions around the center of the potential can be described by a distribution similar to the equilibrium one, with a variance very close to σ_x measured at equilibrium.

Similarly, we can check the effect of the demon on the distribution of speeds, $P(v)$ taken over all the data. The resulting distribution is shown in blue in figure 7.8. Once again, the

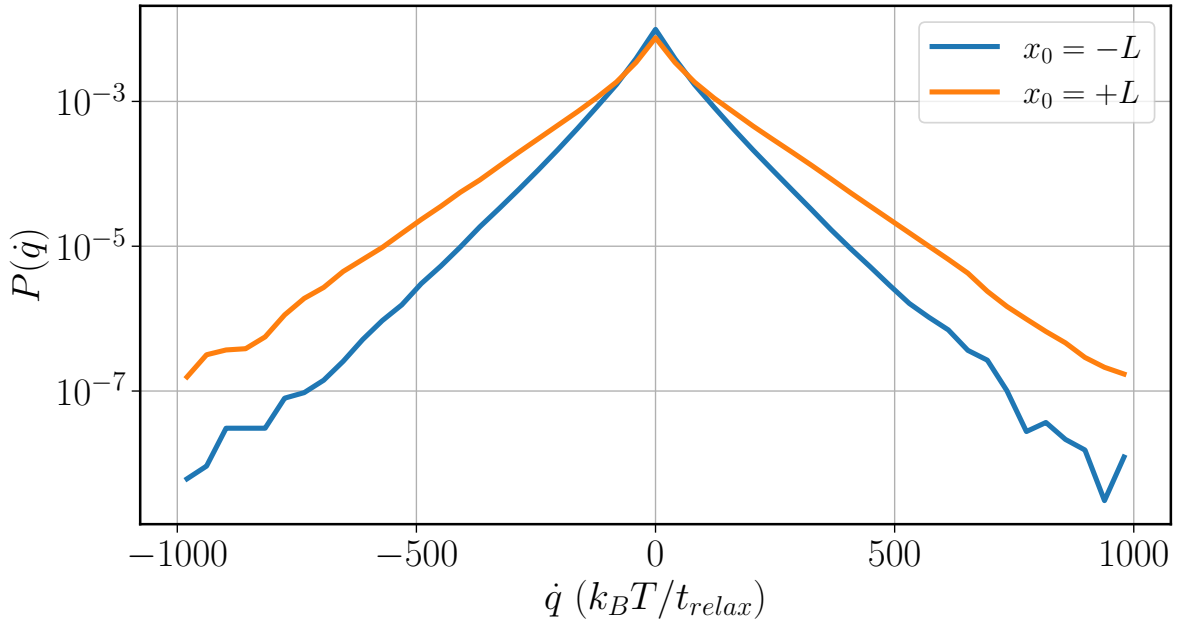

Figure 7.6: Probability distributions of instantaneous heat $\dot{q}$ in the steady state of the experiment for both wells. The distributions are exponential, which is similar to heat fluctuations in an equilibrium system.

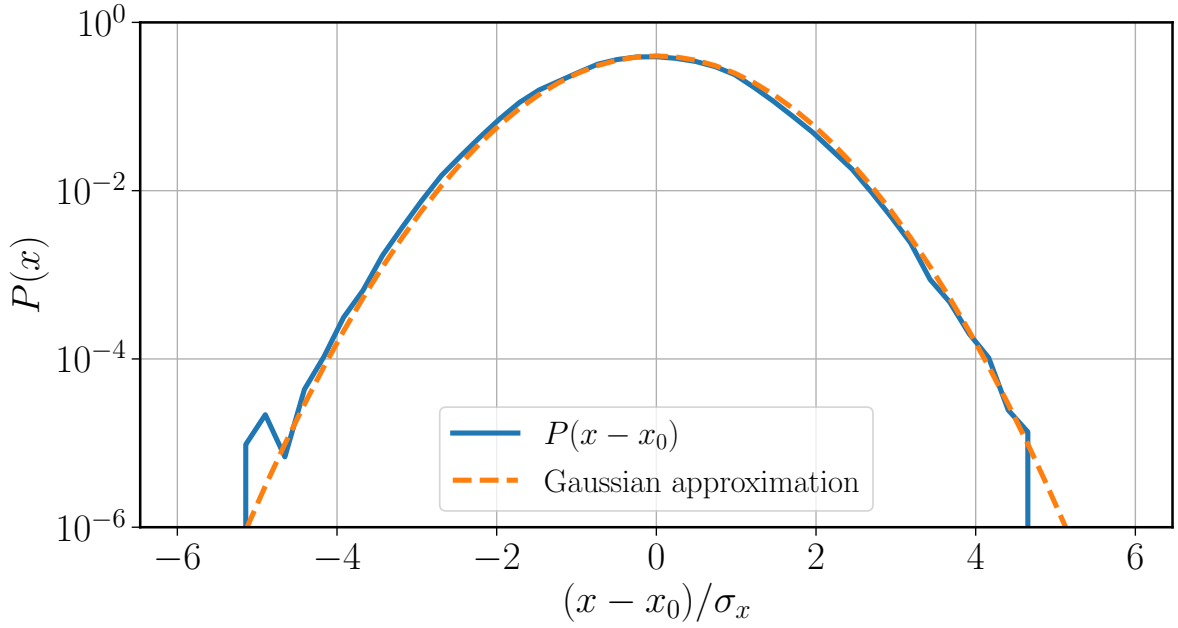

Figure 7.7: The overall distribution $P(x - x_0)$ taken over all the data without condition on the value of x_0. This distribution can be described accurately using a gaussian approximation, shown with an orange dashed line.

distribution looks like a gaussian centered in 0 and with variance v = $1.05\sigma_v^2$. The gaussian approximation is represented by the orange dashed line in figure 7.8 and describes accurately the experimental distribution. Here also, the distribution is very similar to the equilibrium one with a variance close to the one measured at equilibrium.

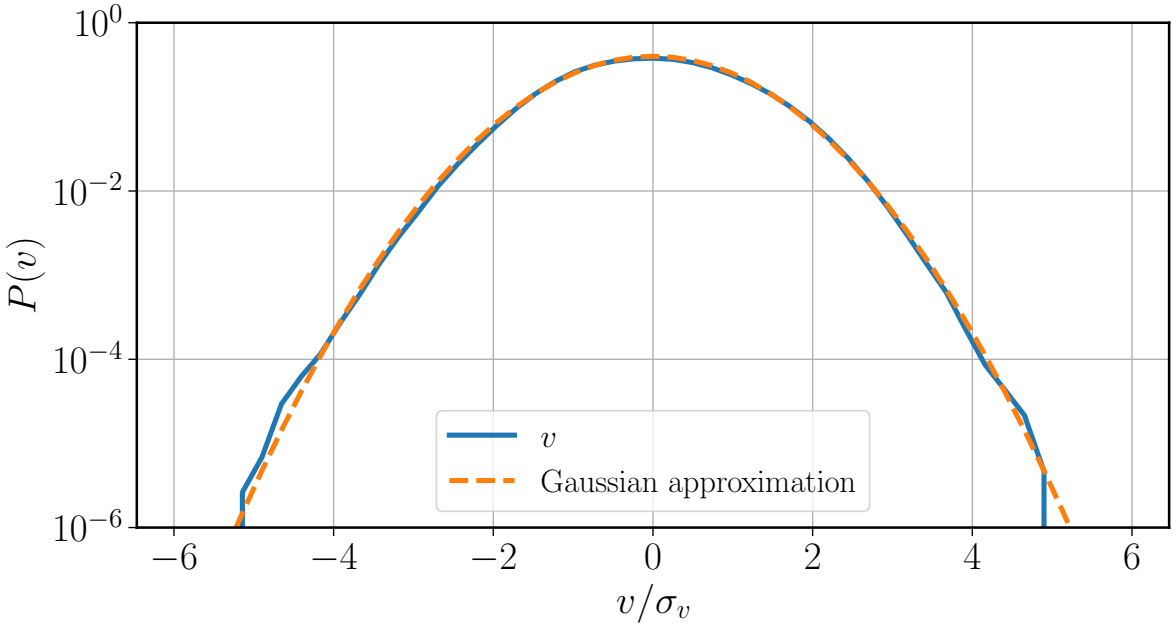

Figure 7.8: The overall distribution $P(v)$ taken over all the data without condition on the value of x_0. This distribution can be described accurately using a gaussian approximation, shown with a orange dashed line.

Both distributions of positions and velocities are very similar to the equilibrium one and would not allow an external observer to detect the operation of the demon. We can also look at the joint probability $P(x, v)$ of positions and velocities. The joint probability, obtained while the demon is operating, is shown in the top left of figure 7.9. The probability distribution is not circular, with a preferred axis in a direction that correlates x and v. Figure 7.9 shows in bottom left the joint probability $P(x, v)$ along the two diagonals of the upper figure. The distribution is wider along the blue diagonal, which indicates a correlation between speed and position.

For comparison, the same distribution but computed on data in equilibrium, without the demon, is shown in the top right of figure 7.9. The same observation, of a probability with a preferred axis in a direction that correlates position and speed, can be made. The distribution along the two diagonals of the distribution is shown in the bottom right of figure 7.9. The correlation between speed and position is confirmed by the fact that the distribution is wider along the blue diagonal.

The fact that both distributions, with and without demon present the same properties show that without knowledge on x_0, it is impossible to characterize the operation of the demon. However, the fact that a correlation between position and speed exists, even at equilibrium is striking.

This effect can be explained by a difference in the computation of x and v. Indeed, both signals are filtered, but the filter used is not the same. For the position, a low-pass Butterworth filter at 50 kHz is used, while for the velocity, a low-pass Butterworth filter at 8 kHz is used. This difference introduces a phase shift between the two signals, that creates a correlation between them.

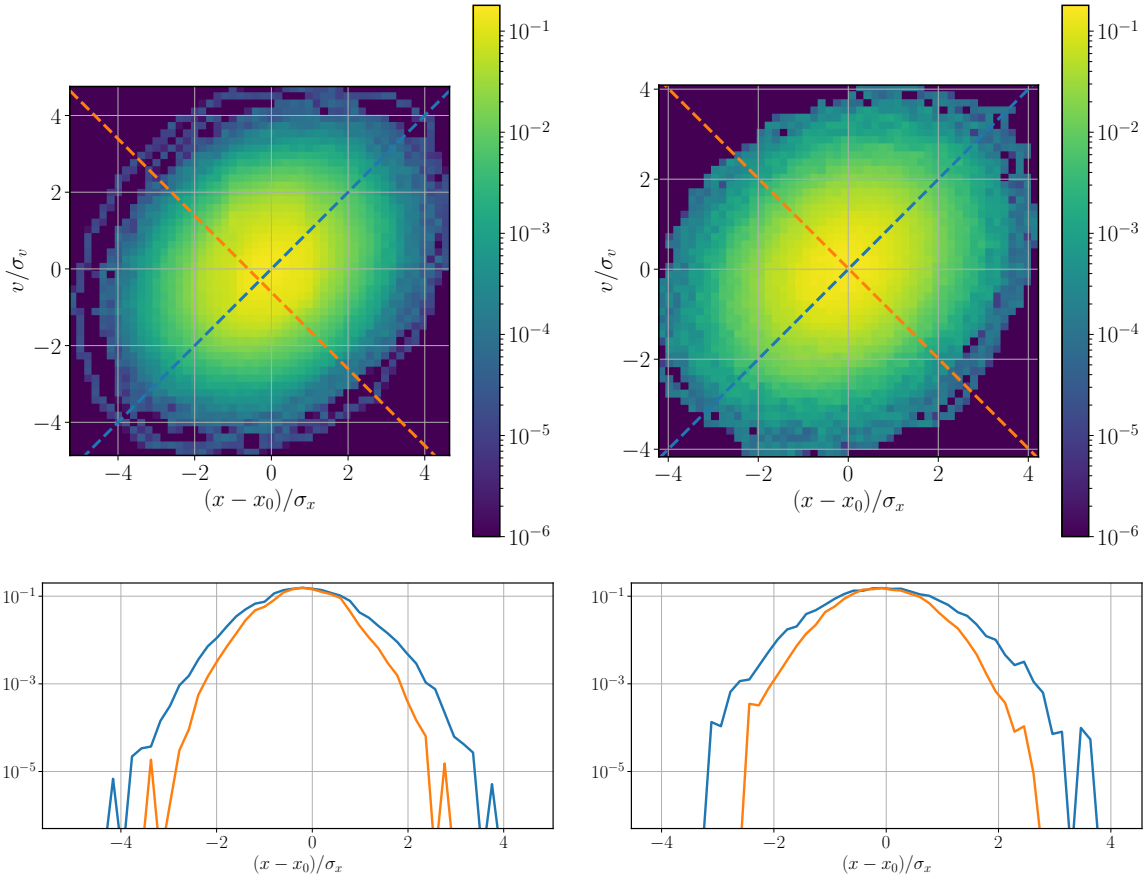

Figure 7.9: Top left: Joint probability $P(x, v)$ while the demon is active. Bottom left: Slice of the joint probability with demon along the two color diagonal from top figure. Top right: Joint probability $P(x, v)$ at equilibrium. Bottom right: Slice of the joint probability at equilibrium along the two color diagonal from top figure.

To confirm this explanation, we plot the same distributions as earlier, but using this time a filter at 8 kHz for both position and velocity. The resulting distributions with demon and without demon are shown in figure 7.10. Using the same filter, the distributions are circular, which indicates no correlation between position and velocity. This absence of correlation is confirmed when looking at slices along the diagonal of the joint probability. The distribution along the two diagonals are the same, which confirms the absence of correlation.

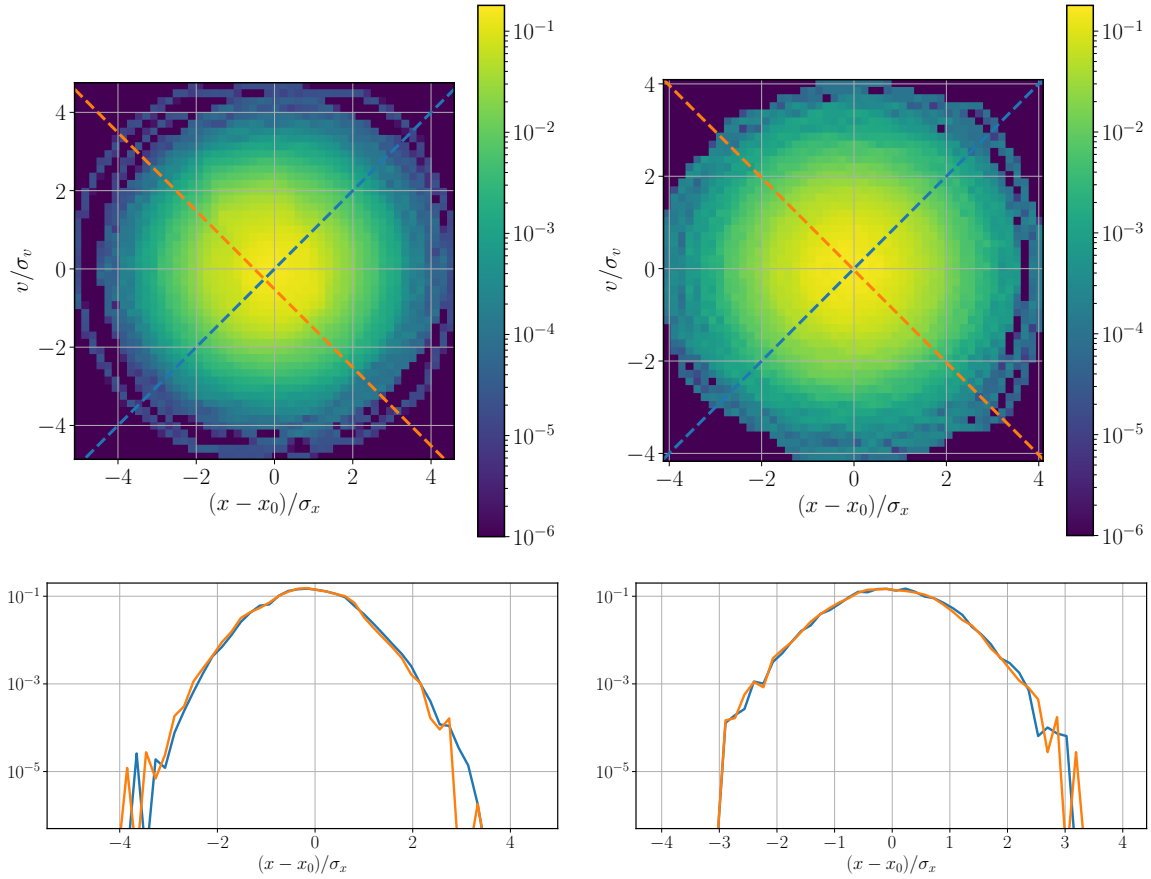

Figure 7.10: Top left: Joint probability $P(x, v)$ while the demon is active, using the same filter for x and v. Bottom left: Slice of the joint probability with demon along the two color diagonal from top figure (to compare with bottom left of fig.7.9). Top right: Joint probability $P(x, v)$ at equilibrium, using the same filter for x and v. Bottom right: Slice of the joint probability at equilibrium along the two color diagonal from top figure (to compare with bottom right of fig.7.9).

7.5 Conclusions

These preliminary results show that our setup can be used to study experimentally what was first presented as a thought experiment by Maxwell. From a particle in contact with a single thermal bath, we are able to create two subsystems at different temperature. We can access the distributions of position and speed, conditioned or not to a well, as well as the distributions of energy exchange with the demon and the thermal bath. The main questions to be studied are the dynamics of the system when the demon starts and stops acting, or how work can be extracted from this difference in temperature created by the demon. We have shown that without knowledge of x_0, it is impossible to detect the presence of the demon. This is a strong

clue that this quantity could be used to access the amount of information taken by the demon to maintain the temperature difference between the wells.

Now that we have a Maxwell Demon, the next step could be to include it in a thermodynamic cycle, for example using the compression developped in chapter 4, to exploit the temperature difference created to extract work, and finding the optimal parameters of the demon for work extraction.

Conclusion on stochastic thermodynamics

We presented an experimental setup, built around a micro-cantilever used as a model for a 1D system under thermal fluctuations. Using a Langevin equation, we are able to describe its dynamics, model its mechanical response and reconstruct thermodynamic quantities for individual trajectories at the scale of the thermal fluctuations. We used this setup to perform different kinds of feedback protocol to study the link between information and thermodynamics.

In chapter 5, we studied a feedback protocol based on discrete sampling of the position of the particle. We optimised the power output of the engine for different regimes of the sampling time. By comparing it to numerical simulation of an overdamped system, we highlighted the specific resonant effects of our inertial system. We applied the framework from [66] to measure the efficiency of our engine in terms of information. While the amount of information extracted is large, the actual amount of information used by our feedback, is low, resulting in a much lower but tighter bound on the extracted work.

In chapter 6, we studied a protocol based on continuous sampling of the position of the particle. While being similar to the protocol from chapter 5 in the regime of short sampling times, the initial equilibrium state makes theoretical studies possible. We develop a description of the system that summarises the set of measurements into one measurement and we propose an extension of the Jarzynski equality close to the one proposed by Ashida et al. We checked experimentally this prediction and found a very good agreement.

Finally, in chapter 7 we use our setup to reproduce Maxwell's original thought experiment. By using a feedback on the velocity of the particle, we are able to separate spatially two subsystems with different effective temperatures. We measured these effective temperatures using position distributions and velocity distributions and indeed found a higher temperature in one of the two subsystems. To confirm that we have a proper demon, we measured the work performed by the demon and found it to be negligible compared to the energy scale of the system. We showed that in order to study the role of the demon, the knowledge of the feedback signal is needed. This signal is a good candidate to build an estimation of the amount of information used by the demon.

A major obstacle to the definition of information we encounter is the correlation between successive measurements when the system doesn't relax to equilibrium. Our setup is a very promising system to test propositions of information in these scenario. We raise the question of minimising the unavailable information of a protocol, to maximise the amount of work possibly extracted from a given measurement. We don't know if it is possible to minimise this information loss while optimizing the power output of the engine. We propose a definition of efficiency as $\langle w \rangle / \langle I \rangle$. However, we are not able to apply it in the case of a continuous sampling as it requires the knowledge of the full distribution of durations, $P(k)$, among many values of k. In the case of the Maxwell Demon, the definition of an efficiency to characterise a "good demon" is unclear as the demon doesn't produce any work. This definition might become clearer if the demon is included in a thermodynamic cycle. We have the basic elements to build such a cycle, using the demon from chapter 7 and the compression process from chapter 4. Furthermore, we

only explored the steady-state of the demon. It could be interesting to study the energy fluxes during the transient regimes, when starting and stopping the feedback.

Chapter 8

Effects of the colloidal probe position on micro-cantilever modes

As this chapter is mostly an inclusion of a preprint, the notations used are independent from these of previous chapters.

In this chapter we work on a description of flexural modes of cantilevers loaded with a colloidal probe. We mentioned in chapter 3 that higher order flexural modes exist, and that we want to separate them from the first mode. Loading the cantilever modifies the frequencies of the modes and can be a way to isolate the first mode. This work has also applications outside of our experiments. Colloidal probes are often used in force microscopy when the geometry of the tip-sample interaction should be well controlled. Their calibration requires the understanding of their mechanical response, which is very sensitive to the details of the force sensor consisting of a cantilever and the attached colloid. We present analytical models to describe the dynamics of the cantilever and its load positioned anywhere along its length. The thermal noise calibration of such probes is then studied from a practical point of view, leading to correction coefficients that can be applied in standard force microscope calibration routines. Experimental measurements of resonance frequencies and thermal noise profiles of raw and loaded cantilevers demonstrate the validity of the approach.

8.1 Introduction

Atomic Force Microscopy (AFM) is nowadays a routine technology in many laboratories, from material science to biophysics [83–86]. This scanning microscopy is based on the interaction between a local probe and a sample. The force is recorded by monitoring the deflection of a cantilever supporting the local probe, designated as the tip. In many applications, the control of the tip shape is beneficial to an enhanced reproducibility and to reach quantitative measurements [87–98]. Colloidal probes trade the tip sharpness and associated spatial resolution for a better knowledge of the probe geometry and a better interpretation of the force signal. They are manufactured by attaching to the cantilever a bead with a diameter ranging from a few to over a hundred micrometers. To fully exploit the better knowledge of the interaction geometry and reach quantitative measurements, the probe itself and its mechanical response should be well characterized and calibrated.

One key question is the calibration of the force sensitivity [84, 99]: how do we translate the measured deflection of the cantilever into a force of interaction? To answer this question, we need to understand how a force applied locally at the tip deflects the cantilever, and how this deflection is measured. We therefore need a description of the cantilever shape, and of a calibration technique to apply a known force and read the corresponding deflection. The latter

part is often performed using a thermal noise calibration[100]: in equilibrium at room temperature T, the environnement exerts a random force whose statistical properties are described by the fluctuation-dissipation theorem. An harmonic oscillator of stiffness k for example presents a mean square displacement $\langle Z^2 \rangle = k_B T/k$, where k_B is the Boltzmann constant. Measuring $\langle Z^2 \rangle$ therefore leads to the value of k. The complexity of the problem increases for a cantilever, which is a spatially extended object, whose deflection is generally measured locally with some optical technique. For small tips, an Euler-Bernoulli description of the cantilever by a clamped-free mechanical beam is well suited, and leads to the established thermal noise calibration of the probe sensitivity[100]. The introduction of a relatively heavy and large load close to its free end modifies significantly the dynamical behavior to the force probe, and should be addressed. Some approaches rely for example on finite element analysis for the determination of calibration parameters [101]. In Refs. [90, 102–104], extensions of the analytical approach of the Euler Bernoulli model [105] to beads glued at the free end of the cantilever are worked out.

In this chapter, we further refine these last approaches to take into account more precisely the geometry of the probe. Indeed, previous approaches are restricted to a colloidal bead attached precisely at the extremity of the cantilever, which is an idealization of the experimental situation. To be more faithful to real world probes, we add here the possibility of a setback with respect to this free end (section 8.2), or of a possible rigidification of the cantilever free end due to the gluing process (section 8.3). The questions are then to understand what is the shape of the cantilever's deflection, and how should one handle the thermal noise calibration (section 8.4). Once the theoretical stage set, we demonstrate the validity of the models introduced with experiments on three different cantilevers (section 8.5). The added loads are characterized by studying how the resonance frequencies of the lever are modified by the functionalisation, and the resonance mode shape are compared to the prediction of the two models.

8.2 Analytical solution, single point contact

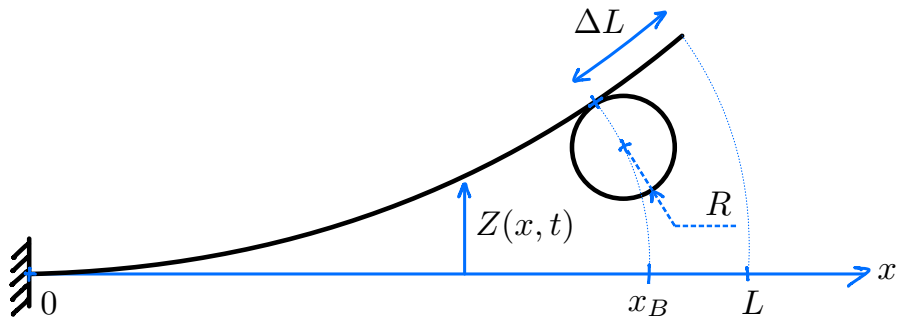

Figure 8.1: Sketch of an AFM cantilever of length L loaded with a colloïdal particle of radius R at an offset ΔL from the free end. The bead is supposed here to have a single point of contact with the cantilever, where it can exert a force and a torque. $Z(x,t)$ describes the deflection along the cantilever.

We consider a cantilever of length L, width W, thickness H, functionalized with a colloidal particle of radius R, as sketch in Fig. 8.1. This sphere is supposed to be glued on the symmetry axis of the cantilever, at a distance ΔL from the cantilever free end. We neglect in a first approximation the effect of rigidification due to the gluing process: the contact between the bead and the cantilever is supposed to be punctual, and the bead infinitely rigid. It will influence the cantilever motion by adding a local force (due to its inertia in translation) and

torque (inertia in rotation). The Euler Bernoulli equation for the deflection $Z(x,t)$ along the cantilever length writes:

$$\frac{EI}{L^4}\partial_x^4 Z(x,t) + \rho A \partial_t^2 Z(x,t) = 0, \tag{8.1}$$

where $I = WH^3/12$ is the second moment of inertia of the beam, $A = WH$ its cross section area, E the material Young's modulus, ρ its density, t the time and x the position along the cantilever normalised by L. In absence of external forces, four boundary conditions (BC) shall be applied:

$$Z(0,t) = \partial_x Z(0,t) = 0, \tag{8.2a}$$
$$\partial_x^2 Z(1,t) = \partial_x^3 Z(1,t) = 0. \tag{8.2b}$$

The first two BC express the clamping at $x = 0$, the last two hold for the absence of torque and force at the free end $x = 1$. The colloidal particle adds a pair of extra conditions, as by inertia it adds a force $-m_\mathrm{B}\partial_t^2 Z(x_\mathrm{B},t)$ and a torque $I_\mathrm{B}/L\partial_t^2\partial_x Z(x_\mathrm{B},t)$ at $x_\mathrm{B} = 1 - \Delta L/L$, with m_B and I_B the bead's mass and moment of inertia (at the contact point with the cantilever). It translates in the following jump conditions:

$$\frac{EI}{L^2}\left[\!\left[\partial_x^2 Z\right]\!\right](x_\mathrm{B},t) = \frac{I_\mathrm{B}}{L}\partial_t^2\partial_x Z(x_\mathrm{B},t), \tag{8.3a}$$
$$\frac{EI}{L^3}\left[\!\left[\partial_x^3 Z\right]\!\right](x_\mathrm{B},t) = -m_\mathrm{B}\partial_t^2 Z(x_\mathrm{B},t), \tag{8.3b}$$

where $\left[\!\left[.\right]\!\right](x_\mathrm{B})$ stand for the jump of the quantity when crossing x_B: $\left[\!\left[Z\right]\!\right](x_\mathrm{B}) = \lim_{\epsilon\to 0}[Z(x_\mathrm{B}+\epsilon) - Z(x_\mathrm{B}-\epsilon)]$. Note that the cantilever and its slope are continuous at x_B, so that

$$\left[\!\left[Z\right]\!\right](x_\mathrm{B},t) = \left[\!\left[\partial_x Z\right]\!\right](x_\mathrm{B},t) = 0. \tag{8.4}$$

Let us solve this problem by separating space and time: with $Z(x,t) = z(x)e^{i\omega t}$, Eq. 8.1 can be rewritten as

$$z^{(4)}(x) = \alpha^4 z(x), \tag{8.5}$$

where superscript $^{(n)}$ stands for the n^{th} derivative, and α is given by the dispersion relation:

$$\alpha^4 = \frac{\rho A L^4}{EI}\omega^2. \tag{8.6}$$

For the boundary conditions, Eqs. (8.2) and (8.4) apply directly replacing Z by z, and the jump condition can be rewritten as:

$$\left[\!\left[z''\right]\!\right](x_\mathrm{B}) = -\tilde{m}\tilde{r}^2\alpha^4 z'(x_\mathrm{B}), \tag{8.7a}$$
$$\left[\!\left[z^{(3)}\right]\!\right](x_\mathrm{B}) = \tilde{m}\alpha^4 z(x_\mathrm{B}), \tag{8.7b}$$

where $\tilde{m} = m_\mathrm{B}/m_c$ is the bead's mass normalised by the cantilever's one $m_c = \rho AL$, and $\tilde{r} = \sqrt{I_\mathrm{B}/(m_\mathrm{B}L^2)}$ is the normalised giration radius of the bead.

Between 0 and x_B and between x_B and 1, we thus need to solve two boundary value problems of order 4, implying 8 coefficients, we thus need to use 8 boundary conditions to solve it: Eqs. (8.2), (8.4) and (8.7). Fortunately, using an analytical shooting method, the solution can be found with less complexity. We introduce the function $\psi_c(x)$ and $\psi_s(x)$ defined by

$$\psi_c(x) = H(x)\frac{\cosh\alpha x - \cos\alpha x}{2\alpha^2}, \tag{8.8a}$$
$$\psi_s(x) = H(x)\frac{\sinh\alpha x - \sin\alpha x}{2\alpha^3}, \tag{8.8b}$$

with $H(x)$ the Heaviside function (0 if $x < 0$, 1 otherwise). Both are solutions of Eq. (8.5), and verify the BC of Eqs. (8.2a) at $x = 0$. Moreover, they are designed such that $\psi_c''(0) = 1$, $\psi_c^{(3)}(0) = 0$, $\psi_s''(0) = 0$, $\psi_s^{(3)}(0) = 1$. Both functions $\psi_c(x)$ and $\psi_s(x)$, solution of the equation between 0 and x_B, must be completed above x_B to meet the jump conditions (8.7) and continuity ones (8.4). This is conveniently done by adding two terms in $\psi_c(x - x_\mathrm{B})$ and $\psi_s(x - x_\mathrm{B})$ above x_B, with coefficients corresponding to the jump of the second derivative for ψ_c (Eq. 8.7a) and of the third derivative for ψ_s (Eq. 8.7b):

$$\begin{aligned}\phi_c(x) = \psi_c(x) + \tilde{m}\alpha^4\big[&\psi_c(x_\mathrm{B})\psi_s(x - x_\mathrm{B}) \\ &- \tilde{r}^2\psi_c'(x_\mathrm{B})\psi_c(x - x_\mathrm{B})\big],\end{aligned} \tag{8.9a}$$

$$\begin{aligned}\phi_s(x) = \psi_s(x) + \tilde{m}\alpha^4\big[&\psi_s(x_\mathrm{B})\psi_s(x - x_\mathrm{B}) \\ &- \tilde{r}^2\psi_s'(x_\mathrm{B})\psi_c(x - x_\mathrm{B})\big].\end{aligned} \tag{8.9b}$$

Those two functions ϕ_c and ϕ_s now fulfil the BC at $x = 0$ and the jump conditions at $x = x_\mathrm{B}$. We are only left to take a combination of both and write the BC at $x = 1$:

$$z(x) = a\phi_c(x) + b\phi_s(x), \tag{8.10a}$$

$$z''(1) = a\phi_c''(1) + b\phi_s''(1) = 0, \tag{8.10b}$$

$$z^{(3)}(1) = a\phi_c^{(3)}(1) + b\phi_s^{(3)}(1) = 0. \tag{8.10c}$$

Since $(a, b) \neq (0, 0)$, the following condition must be fulfilled:

$$\phi_c''(1)\phi_s^{(3)}(1) = \phi_s''(1)\phi_c^{(3)}(1). \tag{8.11}$$

This implicit equation on α prescribes the countable set of spatial eigenvalues $\alpha_n(\tilde{m}, \tilde{r}, x_\mathrm{B})$ of the resonant modes of the clamped cantilever functionalized by the colloidal particle. Each α_n corresponds to a resonance angular frequency ω_n given by Eq. (8.6).

Using Eqs. (8.10), the eigenmodes ψ_n are for example given by:

$$\psi_n(x) = \phi_c(x) - R_n\phi_s(x), \tag{8.12}$$

where $R_n = \phi_c''(1)/\phi_s''(1)$ is an implicit function of α_n. To define an orthonormal base of eigenmodes, we need to introduce the scalar product. For 2 eigenmodes ψ_n and ψ_p associated with eigenvalues α_n and α_p, let us compute

$$\begin{aligned}\alpha_n^4 \int_0^1 \psi_n(x)\psi_p(x)\mathrm{d}x = \int_0^1 \psi_n^{(4)}(x)\psi_p(x)\mathrm{d}x = \\ \lim_{\epsilon\to 0}\int_0^{x_\mathrm{B}-\epsilon} \psi_n^{(4)}(x)\psi_p(x)\mathrm{d}x + \int_{x_\mathrm{B}+\epsilon}^1 \psi_n^{(4)}(x)\psi_p(x)\mathrm{d}x.\end{aligned} \tag{8.13}$$

By carefully including the jump conditions in $x = x_\mathrm{B}$, after four integrations by parts we get:

$$\begin{aligned}(\alpha_n^4 - \alpha_p^4)\bigg(\int_0^1 \psi_n(x)\psi_p(x)\mathrm{d}x + \tilde{m}\psi_n(x_\mathrm{B})\psi_p(x_\mathrm{B}) \\ + \tilde{m}\tilde{r}^2\psi_n'(x_\mathrm{B})\psi_p'(x_\mathrm{B})\bigg) = 0.\end{aligned} \tag{8.14}$$

When $\alpha_n \neq \alpha_p$, the right parenthesis must be zero and is chosen to define the scalar product $\langle\psi_n.\psi_p\rangle$. We can eventually define the orthonormal base ϕ_n of normal modes by

$$\phi_n(x) = \frac{1}{\sqrt{\langle\psi_n^2\rangle}}\psi_n(x), \tag{8.15}$$

where the normalisation factor is the norm of ψ_n, i.e.

$$\langle \psi_n^2 \rangle = \int_0^1 \psi_n^2(x)\mathrm{d}x + \tilde{m}\psi_n^2(x_\mathrm{B}) + \tilde{m}\tilde{r}^2\big[\psi_n'(x_\mathrm{B})\big]^2. \tag{8.16}$$

This last equation can be understood as the repartition of kinetic energy of the normal mode between the elastic beam (first term), the translation of the bead (second term), and its rotation (last term) [104]. From Eqs. (8.8), (8.9), (8.12) and (8.15), the explicit form of $\phi_n(x)$ can be written, but its long and complex expression is of little interest.

8.3 Analytical solution, rigid end load

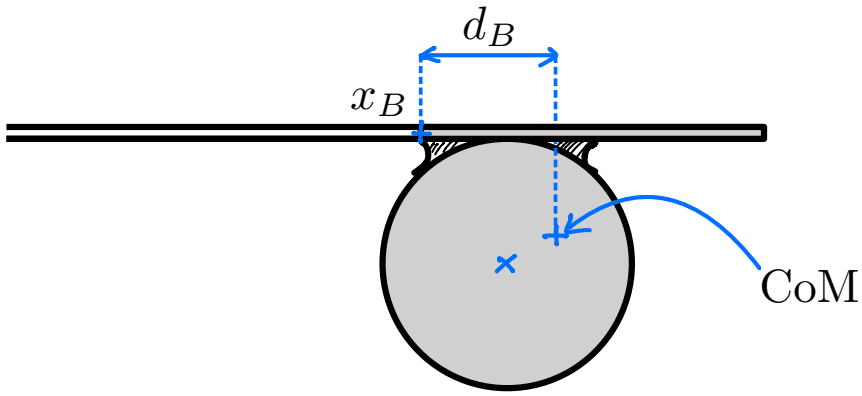

Figure 8.2: Sketch of the cantilever in the approximation of a rigid end load: due to the gluing process, the portion of the cantilever beyond x_B (gray) is supposed to be infinitely rigid. This rigid end load (colloidal particle, glue, cantilever end) will influence the dynamics of the cantilever because of its inertia in translation and rotation. The center of mass (CoM) of the load is not the bead center anymore, we note d_B is its horizontal offset from x_B.

To take into account the rigidification of the cantilever by the gluing process, it is reasonable to model the portion of the cantilever in contact with the cemented bead as infinitely rigid. The portions of the beam before and after the load can be treated with the Euler-Bernoulli equations, with adequate BC at each end: clamped at $x = 0$, free at $x = L$, and criteria matching the inertia in translation and rotation at the load connection. However, one can simplify this complex problem by noting that the portion of the cantilever after the bead is in practical always much shorter than the full cantilever length: $\Delta L \ll L$. This portion will thus be much stiffer, with natural resonance frequencies much higher than those of interest for operation of AFM colloidal probes (see appendix 8.7.4). We can therefore forget about the elasticity of this portion of the cantilever, and consider it as part of a rigid end load. In such case, the center of mass of the load is deported along the cantilever axis as well as perpendicular to it, as sketched in Fig. 8.2.

The Euler Bernoulli equation (8.5) still describes the beam, and clamping conditions (8.2a) in $x = 0$ hold. The BC at the last flexible point of the cantilever in $x = x_\mathrm{B}$ are now:

$$z''(x_\mathrm{B}) = \tilde{m}\alpha^4\big[\tilde{r}^2 z'(x_\mathrm{B}) + d_\mathrm{B} z(x_\mathrm{B})\big], \tag{8.17a}$$

$$z^{(3)}(x_\mathrm{B}) = -\tilde{m}\alpha^4\big[z(x_\mathrm{B}) + d_\mathrm{B} z'(x_\mathrm{B})\big], \tag{8.17b}$$

where d_B is the horizontal offset from x_B of the center of mass of the rigid load normalised to L, and $\tilde{r}$ its normalised giration radius. Adapting the previous derivation or following Ref. [105], we find again eigenmodes shaped as

$$\bar{\psi}_n(x) = \psi_c(x) - \bar{R}_n\psi_s(x) \quad \text{for} \quad x \leq x_\mathrm{B}, \tag{8.18}$$

with $\bar{R}_n$ given below, implicitly function of the eigenvalues values $\bar{\alpha}_n(\tilde{m}, \tilde{r}, x_\mathrm{B}, d_\mathrm{B})$, solutions of:

$$\begin{aligned}\bar{R}_n &= \frac{\tilde{m}\alpha^4(\tilde{r}^2\psi_c'(x_\mathrm{B}) + d_\mathrm{B}\psi_c(x_\mathrm{B})) - \psi_c''(x_\mathrm{B})}{\tilde{m}\alpha^4(\tilde{r}^2\psi_s'(x_\mathrm{B}) + d_\mathrm{B}\psi_s(x_\mathrm{B})) - \psi_s''(x_\mathrm{B})} \\ &= \frac{\tilde{m}\alpha^4(\psi_c(x_\mathrm{B}) + d_\mathrm{B}\psi_c'(x_\mathrm{B})) + \psi_c^{(3)}(x_\mathrm{B})}{\tilde{m}\alpha^4(\psi_s(x_\mathrm{B}) + d_\mathrm{B}\psi_s'(x_\mathrm{B})) + \psi_s^{(3)}(x_\mathrm{B})}.\end{aligned} \tag{8.19}$$

Finally, the normalisation of the eigenmodes $\bar{\phi}_n(x) = \bar{\psi}_n(x)/\sqrt{\langle\bar{\psi}_n^2\rangle}$ is assured with

$$\begin{aligned}\langle\bar{\psi}_n^2\rangle = \int_0^{x_\mathrm{B}} \bar{\psi}_n^2(x)\mathrm{d}x + \tilde{m}\bar{\psi}_n^2(x_\mathrm{B}) + \tilde{m}\tilde{r}^2\left[\bar{\psi}_n'(x_\mathrm{B})\right]^2 \\ +2\tilde{m}d_\mathrm{B}\bar{\psi}_n(x_\mathrm{B})\bar{\psi}_n'(x_\mathrm{B}).\end{aligned} \tag{8.20}$$

Note that above x_B, the normal mode is simply a linear function:

$$\bar{\phi}_n(x) = \bar{\phi}_n(x_\mathrm{B}) + (x - x_\mathrm{B})\bar{\phi}_n'(x_\mathrm{B}) \quad \text{for} \quad x > x_\mathrm{B}. \tag{8.21}$$

8.4 Application to thermal noise calibration of AFM cantilevers

We now explore the application of the computed mode shape to the calibration of AFM cantilevers with thermal noise. Indeed, the stiffness of interest in AFM is usually k_s, the one corresponding to a static deformation, while the thermal noise measurement will usually lead to k_{1m}, the measured dynamic stiffness of the first resonant mode. A correction factor β is therefore defined to link the two:

$$k_s = \beta k_{1m} \tag{8.22}$$

In the absence of colloidal probe, $\beta \simeq 1$, which justifies that the distinction between k_s and k_{1m} wasn't necessary for the previous chapters. In this chapter, we consider that k_s is the static stiffness of the cantilever submitted to a punctual force perpendicular to the cantilever and located at its free end, in $x = 1$. Obviously, when a tip or colloidal probe is present, possibly shifted with respect to $x = 1$, and the cantilever is pushed with some angle on the sample surface, some geometric correction factor needs to be applied to the static stiffness. Those have been computed in Ref. [106] for example, and can be used to translate the cantilever intrinsic stiffness into the one useful for AFM measurement. Our point here is to compute the preliminary step of translating the dynamics stiffness into the intrinsic static one.

The static deflection $z_s(x)$ of the end loaded cantilever is described by the static mode shape $\phi_s(x) = x^2(3 - x)$: $z_s(x) = Z\phi_s(x)/\phi_s(1)$, with Z the deflection in $x = 1$. In most AFM, the deflection measurement relies on a 4-quadrants photodetector and the Optical Beam Deflection (OBD) technique, which actually senses the slope θ_s of the cantilever at the measurement point x_m, i.e.

$$\theta_s = \frac{1}{L}z_s'(x_m) = \frac{\phi_s'(x_m)}{L\phi_s(1)}Z. \tag{8.23}$$

Similarly in the dynamic measurement of mode 1, the sensed slope is $\theta_1 e^{i\omega t}$, with

$$\theta_1 = \frac{1}{L}z_1'(x_m) = \frac{\phi_1'(x_m)}{L\phi_1(1)}\zeta_1, \tag{8.24}$$

where ζ_1 is the amplitude of the deflection in $x = 1$. The output Z of the measurement, interpreted with the static sensitivity by the instrument, is thus

$$Z = \frac{\phi_1'(x_m)\phi_s(1)}{\phi_s'(x_m)\phi_1(1)}\zeta_1 \tag{8.25}$$

The stiffness is estimated from the equipartition theorem, which states that

$$\frac{1}{2}k_B T = \frac{1}{2}k_1\langle\zeta_1^2\rangle, \tag{8.26}$$

with k_B the Boltzmann constant, T the temperature, and k_1 the mode 1 stiffness. Since this equation is usually applied directly to the measured deflection Z, it actually defines the measured stiffness of mode 1:

$$k_{1m} = \frac{k_B T}{\langle Z^2\rangle} = \left(\frac{\phi_s'(x_m)\phi_1(1)}{\phi_1'(x_m)\phi_s(1)}\right)^2 k_1 \tag{8.27}$$

The last step is to link the static stiffness k_s to the dynamic one k_1: as shown in Ref. [104], we have:

$$k_s = \frac{3\phi_1^2(1)}{\alpha_1^4}k_1 = \beta k_{1m}, \tag{8.28}$$

thus we end up with:

$$\beta = 3\left(\frac{\phi_1'(x_m)}{\phi_s'(x_m)}\frac{\phi_s(1)}{\alpha_1^2}\right)^2. \tag{8.29}$$

Since the mode shape $\phi_1(x)$ and the eigenvalue α_1 depend on the loading parameters of the cantilever ($\tilde{m}, \tilde{r}, x_\mathrm{B}$ and d_B in the rigid load model) on top of the measurement point x_m, β depends on up to 5 five parameters which change from one probe to another. Our models anyway take fully into accounts those 5 parameters and let one compute β in each particular situation. We provide an example in tables 8.1 and 8.2 of such an evaluation for a generic situation. We consider a typical silicon cantilever for contact mode, $L = 500\,\mu$m long, $W = 30\,\mu$m wide, $H = 3\,\mu$m thick, with a silica bead of radius $R = 0$ to $100\,\mu$m, glued at a distance $\Delta L = 0$ to $0.3L$ from the free end. The amount of glue is supposed to be negligible, but for the rigid end load model we assume the last part of the cantilever (from $L - \Delta L$ to L) to be rigid. Finally, we suppose that the measurement point x_m is tuned at the bead position x_B.

The first step to apply the model is to compute the parameters for the two models. We therefore compute the cantilever mass $m_c = \rho LWH$, with $\rho = 2330\,\mathrm{kg/m^3}$ the density of silicon, and that of the bead $m_\mathrm{B} = 4\rho_\mathrm{B}\pi R^3/3$, with $\rho_\mathrm{B} = 2650\,\mathrm{kg/m^3}$ for silica. For the punctual contact model, we compute as in Ref. [104]:

$$\begin{aligned}\tilde{m} &= \frac{m_\mathrm{B}}{m_c}\\ \tilde{m}\tilde{r}^2 &= \frac{m_\mathrm{B}}{m_c}\frac{7}{5}\frac{R^2}{L^2}.\end{aligned} \tag{8.30}$$

For the rigid load model, the last part of the cantilever has to be added to the rigid load, leading to:

$$\begin{aligned}\tilde{m} &= \frac{m_\mathrm{B}}{m_c} + \frac{\Delta L}{L}\\ \tilde{m}\tilde{r}^2 &= \frac{m_\mathrm{B}}{m_c}\frac{7}{5}\frac{R^2}{L^2} + \frac{\Delta L^3}{L^3}\\ \tilde{m}d_\mathrm{B} &= \frac{1}{2}\frac{\Delta L^2}{L^2}\end{aligned} \tag{8.31}$$

Once those parameters evaluated, we can compute numerically the eigenvalue α_1 and the associated mode shape ϕ_1, and finally the correction factor β. Note that the resonance frequency distribution of all modes, or their shift with respect to an unloaded cantilever, are also available with this approach.

Table 8.1: Generic situation, punctual contact model

α_1		R (μm)					
		0	10	20	30	60	100
x_B	1.0	1.875	1.715	1.289	0.990	0.594	0.398
	0.9	1.875	1.751	1.366	1.063	0.640	0.427
	0.8	1.875	1.783	1.450	1.147	0.696	0.462
	0.7	1.875	1.811	1.539	1.246	0.763	0.504

β		R (μm)					
		0	10	20	30	60	100
x_B	1.0	0.817	0.877	0.966	0.995	1.027	1.073
	0.9	0.832	0.854	0.898	0.918	0.949	0.999
	0.8	0.867	0.868	0.871	0.877	0.906	0.961
	0.7	0.917	0.909	0.883	0.871	0.894	0.956

Table 8.2: Generic situation, rigid load model

α_1		R (μm)					
		0	10	20	30	60	100
x_B	1.0	1.875	1.715	1.289	0.990	0.594	0.398
	0.9	1.873	1.749	1.365	1.062	0.640	0.427
	0.8	1.857	1.769	1.445	1.146	0.696	0.462
	0.7	1.820	1.765	1.518	1.239	0.763	0.504

β		R (μm)					
		0	10	20	30	60	100
x_B	1.0	0.817	0.877	0.966	0.995	1.027	1.073
	0.9	0.831	0.854	0.898	0.918	0.949	0.999
	0.8	0.857	0.859	0.867	0.875	0.905	0.961
	0.7	0.859	0.860	0.861	0.862	0.892	0.956

In tables 8.1 and 8.2, we report a set of computed values for the generic situation defined above, for the 2 models. It is interesting to note that in this generic situation, the rigid load model is an approximation of the punctual contact model, and thus monitors to what extent this rigid end approximation is valid. We see that for a small offset ΔL or a large load, values of α_1 and β differ very little: in the examples reported here, the difference is lower than 1% as soon as $x_B > 0.8$ or $R > 20\,\mu$m. In these cases indeed, the rigid end approximation is reasonable, as it concerns only a small fraction of the cantilever (small offset), or because this end part has a very little impact on the dynamics compared to the heavy load. Note that the difference on β would be more noticeable by measuring in $x_m = 1$ instead of $x_m = x_B$. Of course, when considering higher order modes, the rigid approximation would fail as well.

The values of α_1 or β displayed in tables 8.1 and 8.2 are specific for the geometry and material of the generic example, and should in general not be used for a specific experiment.

8.5 Experiments

To test our models, we measure along loaded cantilevers the amplitude of the thermal noise driven deflection of the first four flexural modes. The raw samples are uncoated silicon All-In-One type A tipless cantilevers from BudgetSensors, with nominal dimensions $L = 500\,\mu$m, $H = 2.7\,\mu$m, and $W = 30\,\mu$m. They are loaded with polystyrene beads of diameter $2R = 150\,\mu$m, placed near the tip of the cantilevers using an epoxy glue. Three different samples (respectively A, B and C) have been prepared with different positions of the bead giving values close to respectively $x_B = 1$, 0.9 and 0.8. The geometry of all cantilevers is characterized using Scanning Electron Microscopy (SEM) (Fig. 8.3), except for the thickness which is too small to be precisely measured. It can however be deduced from the measurement of the first resonance frequency of the unloaded cantilever, since Eq. 8.6 leads to:

$$H = \sqrt{\frac{12\rho}{E}}\frac{L^2}{\alpha_1^2}\omega_1, \tag{8.32}$$

where all quantities are tabulated ($E = 169\,$GPa, $\rho = 2340\,\mathrm{kg/m^3}$, $\alpha_1 = 1.875$) or measured (L, ω_1). The measured values of the geometrical parameters and deduced values of the dimensionless parameters $\tilde{r}$ and $\tilde{m}$ are presented in appendix, table 8.3.

The power spectrum density (PSD) $S_d(f)$ of the deflection is measured on a large frequency bandwidth for the 3 cantilevers using a quadrature phase differential interferometer [54] featuring a high spectral resolution reaching $10^{-14}\,\mathrm{m}/\sqrt{\mathrm{Hz}}$. This interferometric setup gives access to the calibrated vertical deflection $z(x,t)$ along cantilevers, where 4-quadrant photodiode setups measure the slope of this deflection. Fig. 8.4 shows an example of a measured PSD. Different peaks can be seen, corresponding to the different flexural or torsional modes of the cantilever, driven by thermal noise only. The resonance frequency of the first 4 flexural modes, both for the raw (f_n^r) and loaded (f_n^l) samples, are extracted from those spectra, and reported in appendix, table 8.4. The relative uncertainty on those measurements is very small, typically below 10^{-3}, making them an excellent marker to track the effect of the loading.

The resonance frequencies f_n are linked to the spatial eigenvalues α_n by Eq. 8.6, with a multiplicative factor that is unchanged when loading the cantilever. We therefore expect the ratio of loaded (superscript ^{l}) to unloaded (superscript ^{r}) values of the resonance frequency to be

$$\frac{f_n^l}{f_n^r} = \left(\frac{\alpha_n^l(\tilde{m},\tilde{r},x_B,d_B)}{\alpha_n^r}\right)^2 \tag{8.33}$$

where the dependency of α_n^l in d_B only stands if we consider the end load model. Since we can compute this ratio for four modes in our experiment, we have a set of 4 equations with 3 unknowns ($\tilde{m},\tilde{r},x_B$) for the single point contact model, and a fourth one (d_B) for the rigid end load model. We can therefore extract the values of those 3 or 4 parameters with a good precision using the frequency shifts from raw to loaded. For the single point contact model, we can even extract those parameters from the loaded frequencies alone: studying the ratio f_n^l/f_1^l with $n = 2$ to 4 leads to 3 equations with 3 unknowns. This approach relying on the measurement of resonance frequencies of the loaded cantilever alone could be expanded to the rigid end load model by considering more modes (5 at least). The values extracted for the 3 samples and the different models and approaches are reported in the appendix tables 8.5 to 8.7, they are in reasonable agreement to what is expected from the geometry. As those values are extracted from measurements, they can be more accurate as they include the effect of the

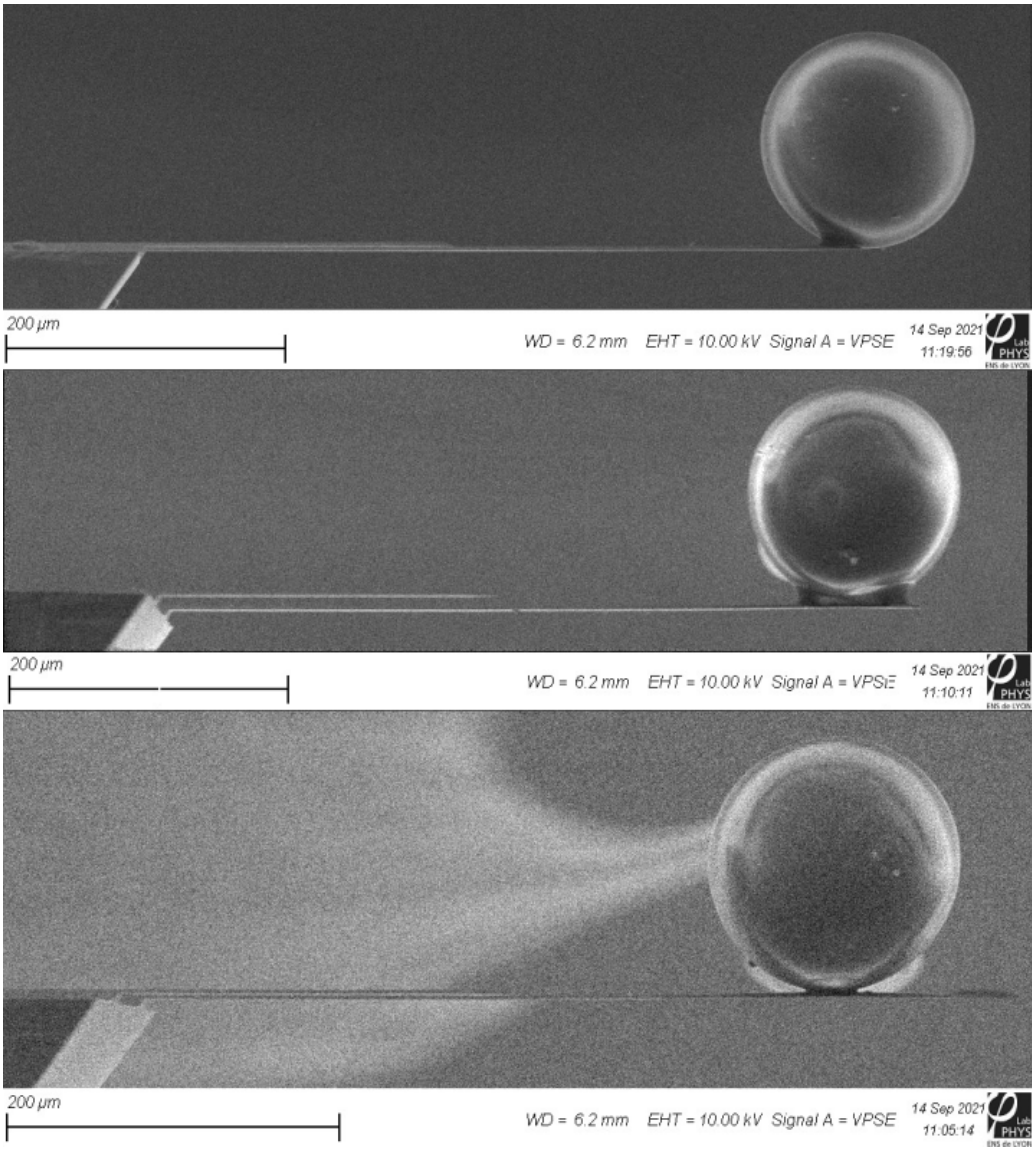

Figure 8.3: SEM images of the 3 cantilevers with, from top to bottom, $x_B = 1$, $x_B = 0.9$ and $x_B = 0.8$. The trail on the third picture is an artifact from the SEM measurement (insulating silica bead charging under the electron beam).

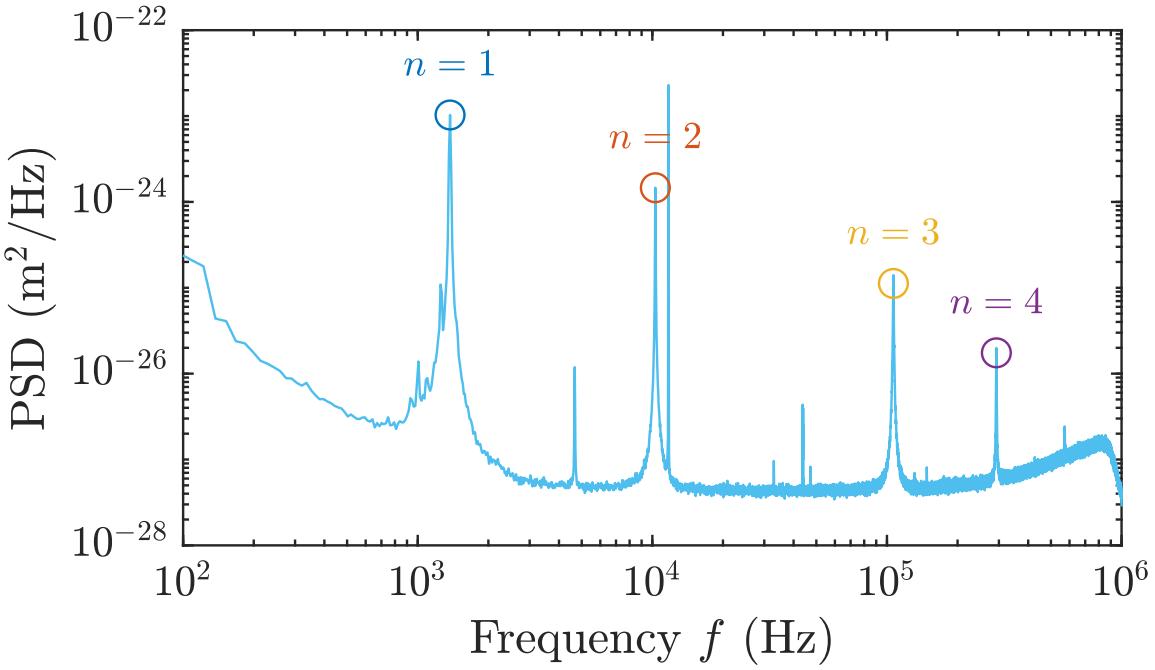

Figure 8.4: Power spectrum density of the thermal noise driven deflection of a cantilever loaded with a polystyrene bead. The different peaks correspond to the different flexural (labelled with n) and torsional (unlabelled) modes of the cantilever. This spectrum is measured on cantilever B with $x_B \sim 0.9$, at $x = 0.26$.

glue, defects on the cantilever or bead, contamination, deviations from the tabulated densities, etc. Note that when extracting the model parameter values, some precautions need to be taken with respect to the mode order, as detailed in appendix 8.7.4.

The PSD of thermal noise can be measured at different positions x along the cantilever, revealing the modes' shape [104, 107]: by integrating the spectrum on a small frequency window around the different peaks, we construct the spatial profile for each mode, as illustrated in Fig. 8.5. We can superpose on those profiles the expectations from the two models: the only parameters left to determine are the length L and origin x_0 of the position measurement, and the stiffness k_s of the cantilever that drives the amplitude of the thermal noise. We perform a simultaneous fit of the four modes profiles to extract those parameters and plot the expectation from the models in Fig. 8.5 for cantilever B, and in appendix for the two other samples (Fig. 8.6). The two models provide a very good description of the mode shape and thermal noise amplitude, except for the single contact point model for mode 2. This small deviation between the model and the measurement could either come from an excess extrinsic noise superposing to the thermal fluctuations in this frequency range, or from the model itself which is oversimplifying the actual physical system. The stiffnesses deduced from the fits are anyway very consistent with the ones measured on the raw samples, as one would expect.

8.6 Conclusions

In this chapter, we present two analytical approaches to deal with functionalized cantilevers with a load not attached exactly at their free end. The simple point contact model takes into account the inertia (in translation and rotation) added by the load in a single point of the cantilever, which is allowed to deform all along its length. This model is expected to be pertinent for geometrically small loads or for small contact areas between the load and the cantilever. The rigid end load model simply builds upon the hypothesis that the cantilever is very rigid beyond

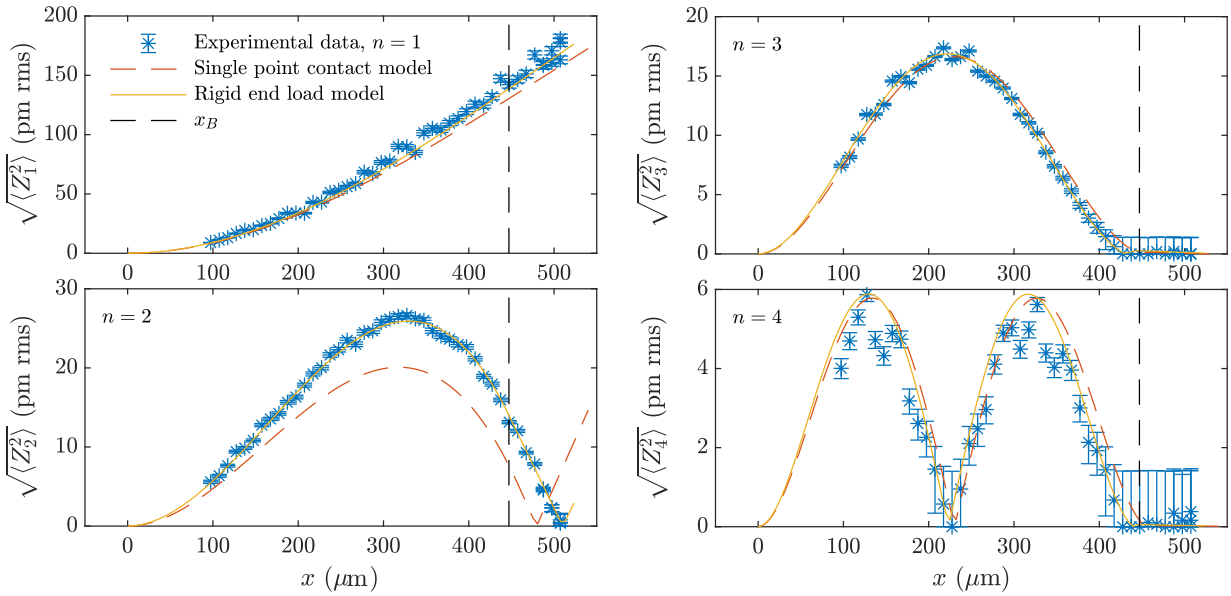

Figure 8.5: Thermal noise amplitude for the different modes measured along the cantilever (blue stars) for cantilever B ($x_B \sim 0.9$, materialized on the graph with the vertical black dashed line). The error bars correspond to the statistical uncertainty and floor noise of the measurement process. The result of a simultaneous fit on the four modes using the point contact model (dashed red) and the rigid end load model (plain line, orange) is superposed. Since the amplitude of the mode is measured as $\sqrt{Z_n^2} = \sqrt{\int S^2(\omega) d\omega}$, the absolute value of each mode is plotted for the fitted model.

the contact with the load, and should be valid for large loads close to the extremity, or large amounts of glue that rigidify the end part of the lever. We solve the Euler-Bernoulli equations corresponding to these cases and study the corresponding mode shapes. This leads to calibration coefficients that can be used to interpret thermal noise measurement in standard AFMs, and deduce the probe static stiffness. Finally, we performed some measurements on 3 different samples to illustrate the approach. From thermal noise spectra, we measure the resonance frequencies of the first modes of the cantilever, from which we deduce the properties of the load: mass, gyration radius, position. A comparison between the mode shapes, analytically computed, and extracted from the thermal noise measurements, demonstrates the relevance of the approach. For the large loads we probe here (beads of diameter 150 μm for cantilevers 500 μm long), both models work, though the rigid end load model leads to slightly better results.

A key learning from this study is that the knowledge of several resonance frequencies of the cantilever, ideally before and after loading, but potentially of the loaded cantilever alone, can be enough to extract the load parameters (mass, giration radius, position). Indeed, the ratio of these frequencies delivers this information regardless of the cantilever geometry, and is eventually enough to conclude on the calibration coefficients. Once the static stiffness extracted, the geometrical parameter can finally be used with the conclusions of Ref. [106] to make quantitative force measurements with any AFM.

Using these models, we can predict the frequency repartition of modes on a cantilever with a colloidal probe. This can be use to determine the position and characteristics needed for a probe in order to obtain certain properties for our cantilever. This knowledge can be applied to engineer specific probes for stochastic thermodynamics experiments, or have a better control over their parameters. The next chapter presents microfabrication techniques that we use to craft specific samples.

8.7 Appendix

8.7.1 Cantilevers' geometrical characteristics

Table 8.3 reports the geometrical dimensions of the cantilever (widths W and length L) and of the glued bead (radius R and position x_B), measured on SEM images. The cantilever thickness H is deduced from the first resonance frequency and the Euler-Bernoulli description of the cantilever. The dimensionless mass $\tilde{m}$ and gyration radius $\tilde{r}$ are computed from those measurements, using $\rho = 2340\,\mathrm{kg/m^3}$ for the density of silicon and $1050\,\mathrm{kg/m^3}$ for polystyrene. The stiffness computed from the geometry (using $E = 169\,\mathrm{Gpa}$ for the Young modulus of silicon in the 110 orientation corresponding to the cantilever long axis) is a good agreement with the stiffness measured from the thermal noise of the unloaded sample.

Table 8.3: Geometrical parameters of the samples measured from SEM imaging. The cross section of the cantilevers is actually trapezoidal, and characterized by its large width W_{top} and small one W_{bottom}. The thickness of the cantilever is deduced from the first resonance frequency of the raw cantilever. The stiffness deduced from the geometry k_s^{Geo} matches the one deduced from the thermal noise amplitude [100] at the end of the raw cantilever k_s^r.

Sample	A	B	C
L (μm)	499 ± 12	523 ± 12	518 ± 12
W_{top} (μm)	27.7 ± 1.4	35.3 ± 0.2	35.4 ± 0.2
W_{bottom} (μm)	14.1 ± 1.4	24.1 ± 0.2	23.9 ± 0.2
H (μm)	2.93 ± 0.14	2.42 ± 0.11	2.52 ± 0.12
R (μm)	75 ± 2.5	75 ± 2.5	75 ± 2.5
$\tilde{m}$	26.1 ± 3.4	21.2 ± 2.6	20.6 ± 2.5
$\tilde{r}$	0.18 ± 0.01	0.17 ± 0.01	0.17 ± 0.01
x_B	1 ± 0.05	0.9 ± 0.05	0.81 ± 0.05
k_s^{Geo} (N/m)	0.176 ± 0.015	0.125 ± 0.008	0.145 ± 0.010
k_s^r (N/m)	0.177 ± 0.004	0.141 ± 0.002	0.137 ± 0.017

8.7.2 Raw and loaded cantilevers' resonance frequencies

Table 8.4 reports the resonance frequencies measured on the raw and loaded samples through the thermal noise PSD.

Table 8.4: Resonance frequency f_n of the first four modes ($n = 1$ to 4) for the raw (superscript ^{r}) and loaded (superscript ^{l}) cantilevers.

	Sample	A	B	C
$n = 1$	f_1^r (Hz)	15668.0 ± 0.9	11888.0 ± 0.9	12629.4 ± 0.8
	f_1^l (Hz)	1420.1 ± 0.5	1370.3 ± 0.6	1716.7 ± 0.2
$n = 2$	f_2^r (Hz)	98692.0 ± 1.5	75381.9 ± 1.3	79132.8 ± 2.7
	f_2^l (Hz)	11006.8 ± 0.9	10305.4 ± 0.9	10378.5 ± 0.5
$n = 3$	f_3^r (Hz)	276225 ± 34	212284 ± 5	220685 ± 22
	f_3^l (Hz)	106084 ± 34	106551 ± 5	132287 ± 22
$n = 4$	f_4^r (Hz)	540627 ± 14	417686 ± 11	429696 ± 13
	f_4^l (Hz)	293643 ± 13	292674 ± 10	363590 ± 12

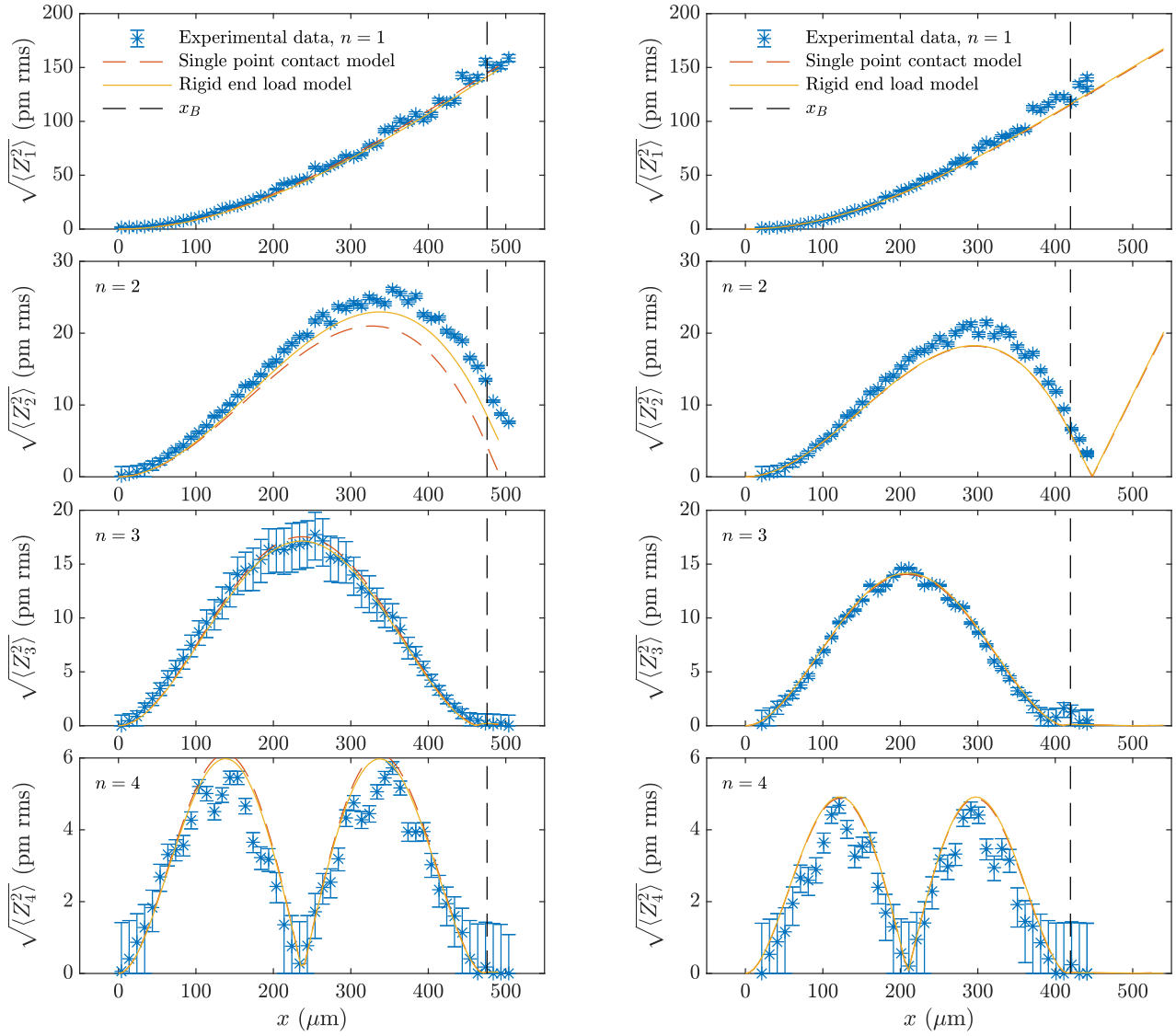

Figure 8.6: Same as Fig. 8.5 for cantilever A ($x_B \sim 1$, left) and C ($x_B \sim 0.8$, right).

8.7.3 Thermal noise profiles and mode shape fits

Fig. 8.6 report the thermal noise profile measured on cantilevers A and C, with the result of the two models superposed. Both describe accurately the experimental data, except for mode 2 of cantilever A for which the end load model is closer to the measurement (though not perfect either). The best fit parameters are reported in Tables 8.5 to 8.7.

Table 8.5: Best fit parameters, single point contact model, with $\tilde{m}$, $\tilde{r}$ and x_B extracted from the resonance frequency shift between raw and loaded samples, while k_s is fitted from the thermal profiles of Figs. 8.5 and 8.6.

Sample	A	B	C
$\tilde{m}$	30.4	27.2	24.9
$\tilde{r}$	0.153	0.141	0.164
x_B	0.970	0.854	0.777
k_s (N/m)	0.178 ± 0.625	0.135 ± 0.002	0.144 ± 0.001

Table 8.6: Best fit parameters, single point contact model, with $\tilde{m}$, $\tilde{r}$ and x_B extracted from the resonance frequency ratio of the loaded samples, while k_s is fitted from the thermal profiles of Figs. 8.5 and 8.6. Those best fit parameters are very close to the ones of Tab. 8.5, showing the equivalence of both approaches. *Note that for sample B, the fit is not converging unless we fix the value of x_B.

Sample	A	B	C
$\tilde{m}$	30.7	28.5	24.9
$\tilde{r}$	0.153	0.139	0.164
x_B	0.975	0.854*	0.777
k_s (N/m)	0.178 ± 0.625	0.135 ± 0.002	0.144 ± 0.001

Table 8.7: Best fit parameters, rigid end load model, with $\tilde{m}$, $\tilde{r}$, x_B and d_B extracted from the resonance frequency shift between raw and loaded samples, while k_s is fitted from the thermal profiles of Figs. 8.5 and 8.6.

Sample	A	B	C
$\tilde{m}$	27.2	21.2	25.2
$\tilde{r}$	0.173	0.193	0.163
x_B	0.970	0.854	0.777
d_B	0.033	0.069	0.000
k_s (N/m)	0.189 ± 0.163	0.133 ± 0.001	0.144 ± 0.001

8.7.4 Single point contact model: families of modes

In Fig. 8.7, we plot the 6 lowest values of $\alpha_n(\tilde{m}, \tilde{r}, x_B)$ computed for the single point contact model with $\tilde{m} = 30$, $\tilde{r} = 0.17$ as a function of the load position x_B. We notice very different behaviors: one family is increasing with x_B, while another is decreasing. If we look at the corresponding mode shape $\phi_n(x)$, we see that the "decreasing" modes (labelled with n) are similar to the unloaded ones, with the load acting as a fixed position for $n > 1$, due its large inertia. The other family (labelled with n') on the contrary corresponds to normal modes of the part of the cantilever beyond the load, and present increasing resonance frequencies when its effective length $L(1 - x_B)$ shortens. When fitting the model parameters x_B explores a small range where modes can change their order between families, so one should be careful to always track the right family. Here, we restrict the fit to family mode n, as the family n' is not experimentally observed: we have few clean measurements beyond x_B, since the glue often

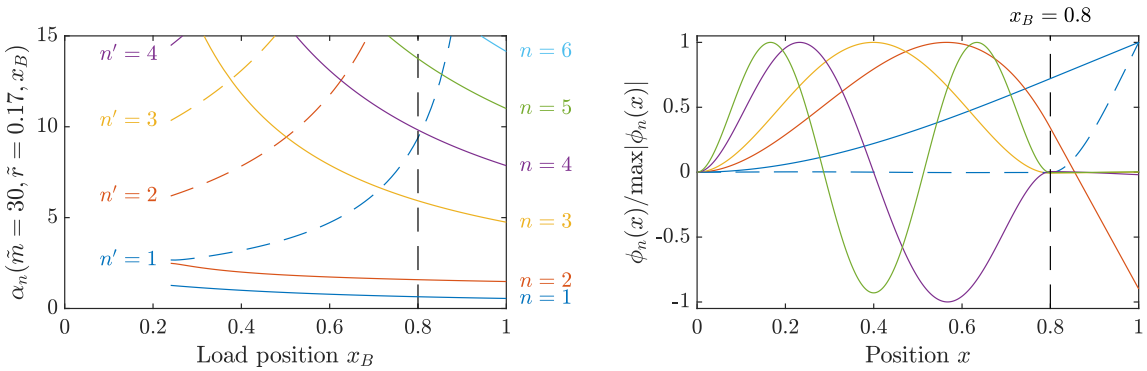

Figure 8.7: (Left) 6 lowest values of $\alpha_n(\tilde{m}, \tilde{r}, x_B)$ computed for the single point contact model with $\tilde{m} = 30$, $\tilde{r} = 0.17$, and x_B from 0.25 to 1. (Right) Mode shapes corresponding to $x_B = 0.8$, using the same color code as the top figure to identify the modes.

degrades the reflectivity of the cantilever in this area. It implies than when x_B can get close to 0.8 (the case of samples B and C), we need to make sure not to mistake the mode $n = 4$ and $n' = 1$, since they swap their order in the eigenvalue list. A simple criterion of the position of the maximum of $\phi_n(x)$ with respect to x_B works very well in this case.

Chapter 9

Experimental development for small forces measurements

9.1 Introduction

A previous project was the measurement of critical Casimir forces. These forces arise near the critical points, for example in binary mixtures, a mix of a solvent and polymers. At room temperature, these mixtures exists in a uniform, mixed, phase. When cooled, a demixing transition occurs and the system separates into two phases with different polymer concentrations. For precise values of concentration in polymers and temperature, a critical point appears. As the solution gets closer to the critical point, fluctuations in polymer density increase, with a diverging correlation length. When this correlation length becomes similar to the size of the system, the walls constrain the fluctuations and the difference between the allowed fluctuations inside and outside of the cavity creates a force on the confining surfaces [108].

Measuring these forces experimentally is a challenge [109–111]. It requires an accurate force measurement setup, good mastery of the chemistry of the mixture used, and precise control over the temperature in the experiment. Our goal here is to present a force measurement setup.

To test the setup without constraints on chemistry or temperature control, we first try to measure the quantum Casimir force predicted by Hendrik Casimir in 1948 [112, 113]. This force arises similarly by confining fluctuations, here of the electromagnetic (EM) field. Its measurement has led to the development of many high accuracy experiments [88, 114–116].

Consider two perfect mirrors (metallic conductive planes) facing each other. The two mirrors form an optical cavity that selects modes of the electromagnetic field. Quantum mechanics predicts that even in their lowest energy state, these modes have non-zero fluctuations, resulting in radiation pressure. More EM modes are allowed outside of the cavity, which results in an higher pressure and an attractive force between the two mirrors.

Experimentally, we work in a sphere-plane geometry, which has many advantages. First, no angle is involved as a rotation of the sphere or the plane keeps the geometry invariant. Second, if the dimensions of the plane are larger than the sphere-plane distance, d, boundary effects are negligible and the plane can be effectively considered infinite. In this geometry, the Casimir force has an expression [117]:

$$F_{cas} = -\frac{\hbar c \pi^3 R}{360 d^3} \tag{9.1}$$

with c the speed of light in vacuum, $\hbar$ the reduced Planck constant and R the radius of the sphere. As the force is proportional to R, it is interesting experimentally to work with large spheres.

9.2 Measurement technique

The setup used for force measurement is based on a micro-cantilever and is very similar to the one presented in chapter 3. We use the electrostatic interaction as a way to measure the sphere-plane distance as well as the contact potential V_c without interfering with the force measurement. We presented this technique in ref. [118].

If a force F is applied on the cantilever, this force will result in an average deflection $\langle x \rangle = F/k$, with k the stiffness of the cantilever. If k is known from a calibration, like the SHO fit presented in 3.1, the measurement of the deflection x results in a measurement of the force F. By varying the separation between the cantilever and the interacting plane, we can measure the force as a function of the separation.

The deflection x of the cantilever is read by a quadrature phase differential interferometer, featuring an intrinsic floor noise of about $10^{-14}\mathrm{m}/\sqrt{\mathrm{Hz}}$ [54, 116]. We use commercial silicon AFM cantilevers (Nanoandmore PPP-ContAu) at the tip of which a polystyrene bead is glued. A gold layer is then coated on the sphere/cantilever set to ensure electrical continuity. The cantilever is typically 450 µm long, 50 µm wide and 2 µm thick. The bead radius is $R = (76.0 \pm 0.5)$ µm, measured in a scanning electron microscope (SEM) before the experiments.

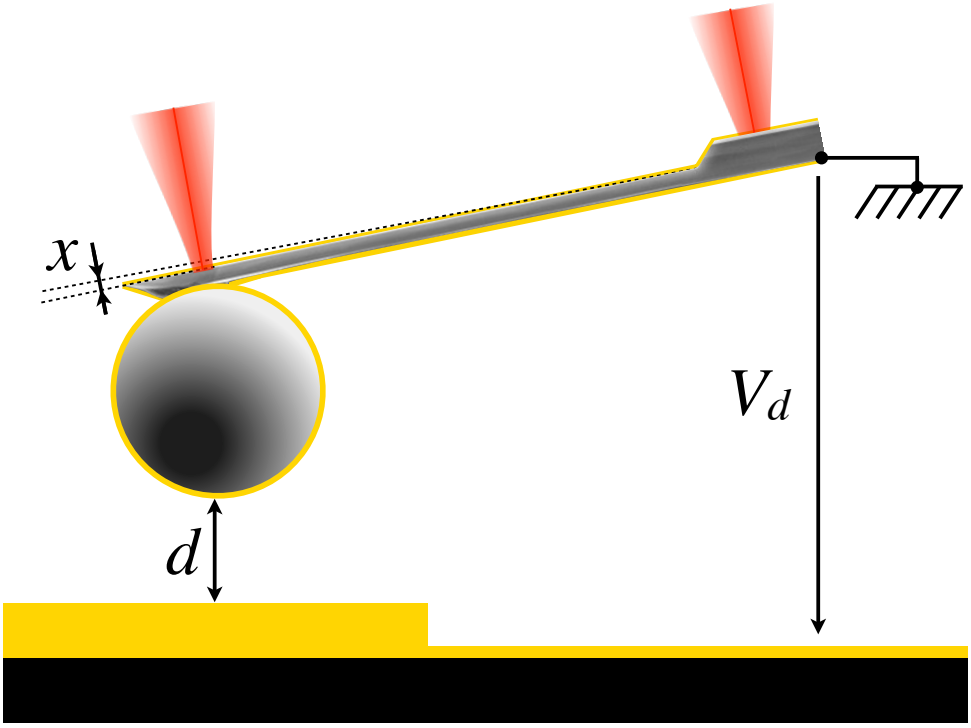

Figure 9.1: Experimental set-up. A polystyrene bead is glued at the tip of the cantilever using UV cured glue. The bead, the cantilever and the surface are coated with gold, so that a voltage V_d can be used to apply a force. The deflection x is read with a differential interferometer, sketched here by the two laser beams [54].

The cantilever is placed in a cell filled with nitrogen. The bead is facing a gold coated silicon wafer. We use a sphere plane interaction to have a well define geometry. A schematic diagram of the set-up is presented in fig. 9.1. A piezoelectric actuator with an integrated displacement sensor allows the control, with an accuracy of 0.2 nm, of the distance d between the sphere and the plane. The gold coating on both surfaces allows us to apply a voltage difference V between them. This voltage creates an electrostatic attractive force on the bead, which for $d \ll R$ takes the form:

$$F_{\mathrm{elec}} = \frac{\pi \epsilon_0 R}{d} V^2 \tag{9.2}$$

where ϵ_0 is the vacuum permittivity [119, 120]. F_{elec} can be used as a test force and as a way to measure d by comparing the response of the cantilever to the applied voltage. However one has to take into account that independently from the applied voltage, a contact potential V_c exists between the gold coatings of the bead and the surface. V_c induces an offset in the total voltage which is unknown because it depends on the surface quality [116, 121]. Thus, in eq. 9.2, $V = V_c + V_d$ where V_d is the externally applied voltage and V_c must be experimentally determined.

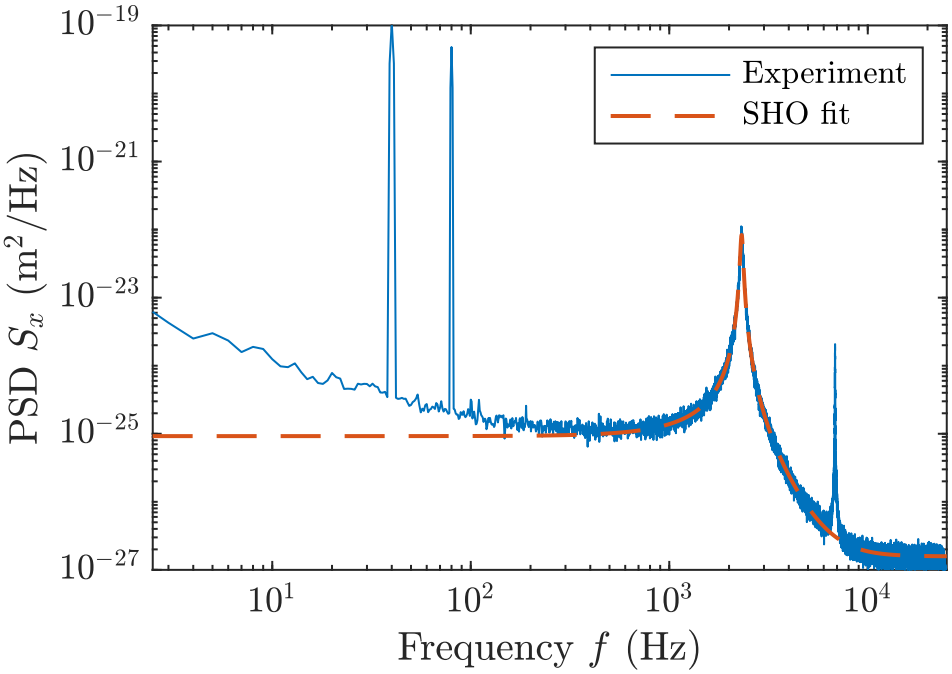

Figure 9.2: The power spectrum density S_x of the deflection when the cantilever is subjected to an electrostatic driving at $\omega_d = 2\pi.40$ rad/s. The quadratic dependency in voltage is evidence by the narrow peaks at ω_d (term $V_0 V_c$ in eq. 9.3) and $2\omega_d$ (term in V_0^2). The rest of the spectrum is only thermal noise driven. The SHO fit is performed on a 1 kHz window around the first resonance of the cantilever. The second resonance peak corresponds to the first torsion mode. The $1/f$ noise at low frequency is due to the viscoelasticity of the gold coating and is not taken into account in the SHO model [122].

9.2.1 Sphere-plane distance measurement

To measure the distance d between the sphere and the plane, we can use a technique derived from Kelvin Probe Force Microscopy, applying a voltage $V_d = V_0 \cos(\omega_d t)$ to the cantilever. The force in the Fourier Space is:

$$\tilde{F}(\omega) = \frac{\pi \epsilon_0 R}{d} \left[(V_c^2 + \frac{V_0^2}{2})\delta(\omega) + 2V_0 V_c \delta(\omega - \omega_d) + \frac{V_0^2}{2}\delta(\omega - 2\omega_d) \right] \tag{9.3}$$

The psd of x in presence of the electrostatic forcing is plotted in 9.2, showing two peaks at ω_d and $2\omega_d$. The response at $2\omega_d$ is only caused by the applied voltage and allows for a measurement of the distance, whereas the term at ω_d couples the applied voltage to the contact potential and allows us to measure V_c [116, 121].

Using eq. 9.3 at $\omega = 2\omega_d$, we have:

$$\tilde{x}(2\omega_d) = G(2\omega_d)\frac{\pi\epsilon_0 R}{d}\frac{V_0^2}{2} \tag{9.4}$$

$$d = G(2\omega_d)\pi\epsilon_0 R\frac{\widetilde{V^2}(2\omega_d)}{\tilde{x}(2\omega_d)} \tag{9.5}$$

with $G = \frac{\tilde{x}}{\tilde{F}}$ the mechanical transfer function of the cantilever, obtained from the SHO fit presented in 3.1. The term $\widetilde{V^2}(2\omega_d)/\tilde{x}(2\omega_d)$ is numerically computed as the transfer function between $V^2(t)$ and $x(t)$. This allows us to measure the distance d without using a reference, such as a contact between the sphere and the plane that would damage the surfaces. When the plane is brought closer to the sphere, $\tilde{F}(2\omega_d) \propto d^{-1}$ increases. To keep a moderate mechanical response of the cantilever V_{AC} is controlled by a feedback loop that targets a fixed value of $|\tilde{x}(2\omega_d)|^2$.

9.2.2 Contact potential

This technique can also be used to measure the contact potential V_c. Using eq. 9.3 at $\omega = \omega_d$, we have:

$$\tilde{x}(\omega_d) = G(\omega_d)\frac{\pi\epsilon_0 R}{d}2V_0 V_c \tag{9.6}$$

$$V_c = \frac{1}{G(\omega_d)}\frac{d}{2\pi\epsilon_0 R}\frac{\tilde{x}(\omega_d)}{\tilde{V}(\omega_d)} \tag{9.7}$$

$$V_c = \frac{1}{2}\frac{G(2\omega_d)}{G(\omega_d)}\frac{\widetilde{V^2}(2\omega_d)}{\tilde{x}(2\omega_d)}\frac{\tilde{x}(\omega_d)}{\tilde{V}(\omega_d)} \tag{9.8}$$

The two terms, $\tilde{x}(\omega_d)/\tilde{V}(\omega_d)$ and $\widetilde{V^2}(2\omega_d)\ \tilde{x}(2\omega_d)$ are measured experimentally as transfer functions between the measured deflection $x(t)$ and the applied voltage $V(t)$, or between the squared voltage V^2 and the deflection $x(t)$. This allows for measurement and cancellation of the contact potential. A feedback is applied such that $V_{DC} = -V_c$ to cancel the constant force due to the contact potential.

This provides us a system to perform force measurements by measuring the average value of the deflection x, with a precise measurement of the distance h between the interacting objects through the electrostatic force, and a control of the distance using a piezo electric actuator.

9.3 Microfabrication process

To measure the Casimir force and apply our distance measurement, the sphere and the plane must not be in contact. The minimal distance to which the sphere and the plane can be brought to is determined by the surface properties of the two. If their roughness is high, or impurities such as dusts are present, the closest possible distance without contact will be larger and limit our force measurement. High quality golden surfaces can be easily found commercially. We chose silicon wafers doped for electrical conductivity, with a 5 nm chromium adhesion layer and 200 nm gold layer. However, cantilevers with large beads are not available commercially, as such probes are not common for AFM measurements. In order to have the best surfaces, we develop a protocol for the microfabrication of our probes: a cantilever functionalised with a sphere, and gold coated. This work was done in collaboration with Agnès Piednoir from Institut Lumière Matière, whose knowledge of microfabrication and sputtering deposition was very useful.

9.3.1 Cantilever functionalisation

Since the interaction between the sphere and the plane is proportional to the radius of the sphere (eq. 9.2 and 9.1), we aim to functionalise the cantilever with a large sphere. We chose polystyrene spheres with a radius $R = 75\,\mu m$. Such large probes are unusual and we need to handcraft our probes from cantilevers with a thin tip, and polystyrene spheres.

The polystyrene beads are taken from a monodisperse suspension from Sigma Aldrich. The beads are dried on a microscope glass slide. To glue the bead onto the cantilever, we use Noa81 UV cured glue. This glue is fluid, which facilitates the manipulation, while requiring only a short exposure to UV (one minute) to fully cure.

To glue the bead, we use micro-manipulators to control the position of tweezers holding the cantilever, and tweezers the tip of which was dipped in the glue. The microscope slide with the beads is placed on the holder of a microscope used to follow the process. The whole setup can be seen on figure 9.3.

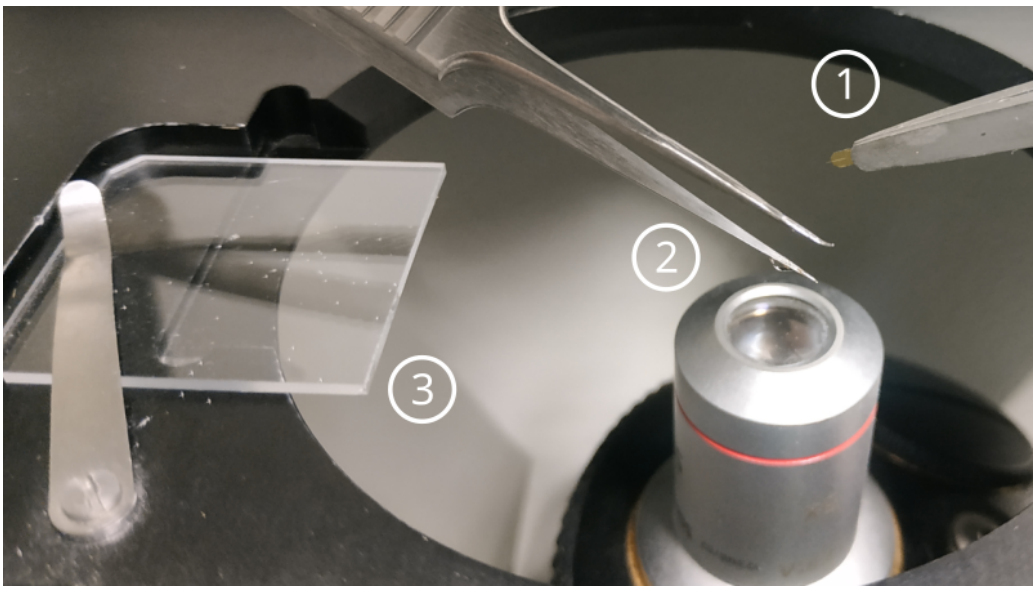

Figure 9.3: The setup used for microfabrication of our probes. Two micro-manipulator are used to move tweezers holding the cantilever (1) and glue (2). Polystyrene beads are deposited on a microscope slide (3).

The protocol is the following:

- First, the tip of the cantilever is slowly put in contact with glue to deposit a droplet. (Figure 9.4a)
- The cantilever is placed in the same plane as the bead and is approached until contact between the cantilever and the bead. (Figure 9.4b)
- The glue is cured by insolating it with UV for one minute.
- The cantilever is moved away from the surface. (Figure 9.4c)

It is crucial during this process to not pollute the sample with impurities. To prevent deposition of dust, we operate in a laminar flow hood. The whole installation is shown in figure 9.5. The laminar flow induces many mechanical vibrations that make the operation of micromanipulator trickier. This drawback is largely compensated by the reduction of the number of impurities on the beads.

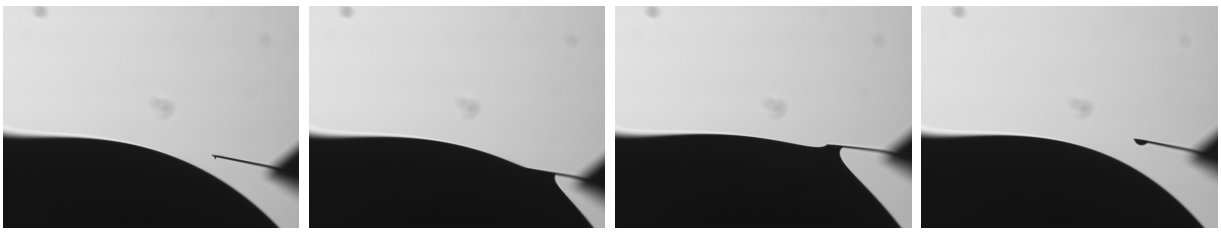

(a) Glue deposition on the tip of the cantilever. The cantilever is 450 µm long. The large shadow at the bottom is the glue drop on the tweezers.

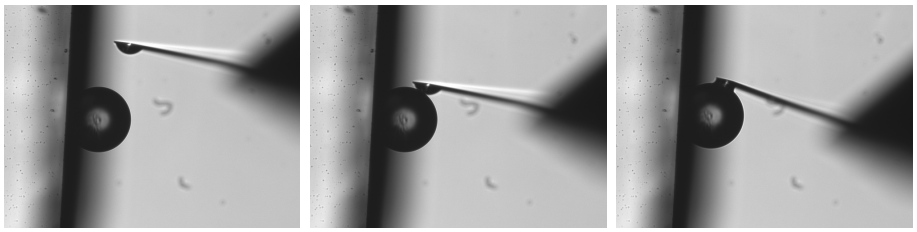

(b) Approach of the cantilever to the sphere.

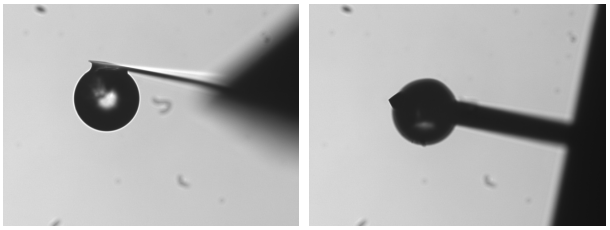

(c) End result after curing the UV glue. Left: Side view of the cantilever. Right: Top view.

Figure 9.4: Gluing process.

9.3.2 Gold coating

In order to polarise electrically the sphere, and to observe Casimir forces, we need a conductive layer around the sphere and along the cantilever. The conductive layer needs to be thick enough to constitute a bulk material and ensure good electrical conductivity. We aim for a 100 nm thick coating.

To obtain a homogeneous coating, we use a sputtering process. The sample is placed in a chamber, pumped to vacuum and filled with argon at low pressure. High voltages are applied to a gold target to extract atoms and create a plasma that will be deposited on the sample. This technique is directive, as the side of the sample facing away from the gold target will receive almost no material. The naïve approach is to coat one side of the sample, and then coat the other side. This technique is appropriate for thin film deposition but creates strong stress at the surface of the cantilever. Depositing first a thick layer on one side of the cantilever would bend the cantilever, making it unusable for force measurements with our differential interferometer.

The solution proposed was to build a rotating cantilever holder, shown in figure 9.6. 6 cantilevers can be held and a vacuum compatible motor slowly rotates the samples at one turn per minute. The assembly is installed in a sputtering machine able to deposit metal with a rate of about $0.2\,\text{Å}\,\text{s}^{-1}$. A quartz oscillator in the chamber, next to our samples is used to measure the amount of metal deposited. Since the quartz is fixed while the samples are rotating, the measured thickness of the deposited layer must be divided by π to obtain the thickness deposited on the sample. In order for gold to stick to surface, we first deposit a thin layer of 5 nm of chromium at an effective rate of $0.1\,\text{Å}\,\text{s}^{-1}$. A layer of 125 nm of gold is then deposited at an effective rate of $0.3\,\text{Å}\,\text{s}^{-1}$.

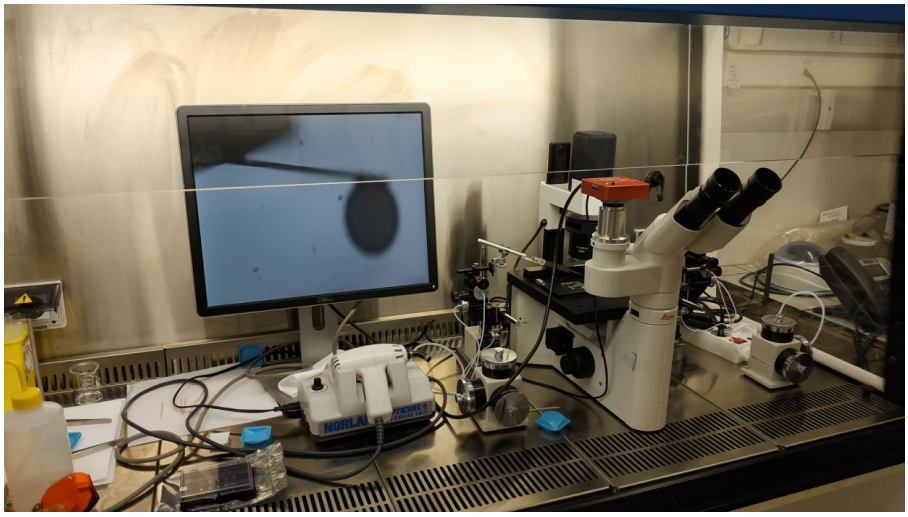

Figure 9.5: The setup used to functionalise cantilevers. A microscope is placed inside a laminar flow hood. Two micro-manipulators are used to move the cantilevers and the tweezers with the glue. A camera is mounted on the microscope and can be used to take reference pictures of the crafted sample.

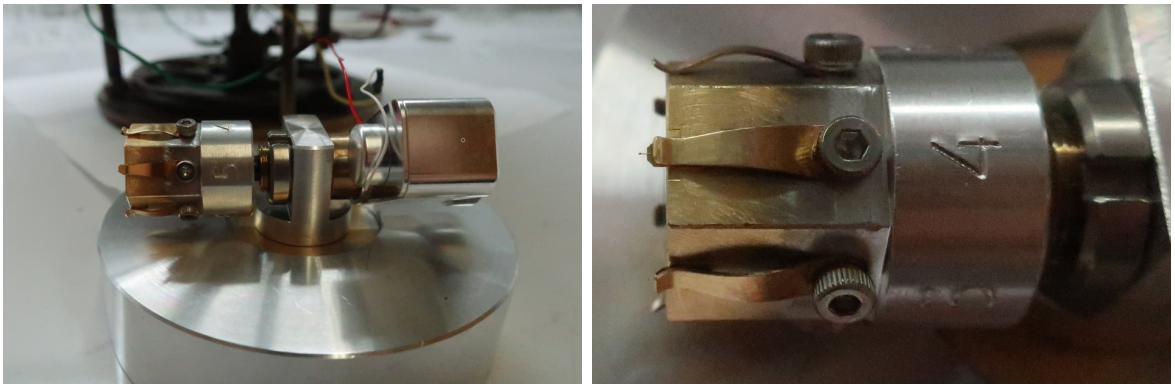

Figure 9.6: Left: The cantilever holder. The left part is a hexagonal head and can hold 6 cantilevers. The right part is vacuum proof piezo inertial motor that can rotate the head. Right: Close-up on the head. 6 cantilevers chips are held so that the cantilevers themselves can be coated without shadow.

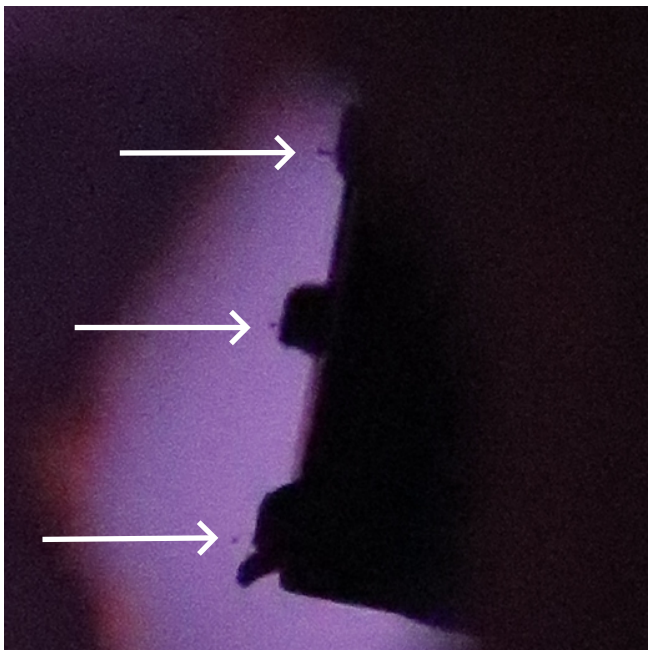

Figure 9.7: Picture of the samples inside the sputtering machine. The purple background is the gold plasma.

9.3.3 Control of the samples

To control the quality of the samples after microfabrication we use SEM and AFM imaging. SEM is useful to obtain a global image of each sample and measure the geometrical dimensions such as the sphere radius. It is a good check of the surface cleanliness. However, it doesn't give any information about the thickness of the layer or the detail of the surface structure. Figures 9.8 and 9.9 compare SEM images of a bead using the previous protocol used (left picture) and using the protocol presented here (right). The number of dust particles on the sphere has been hugely reduced by operating under laminar flow.

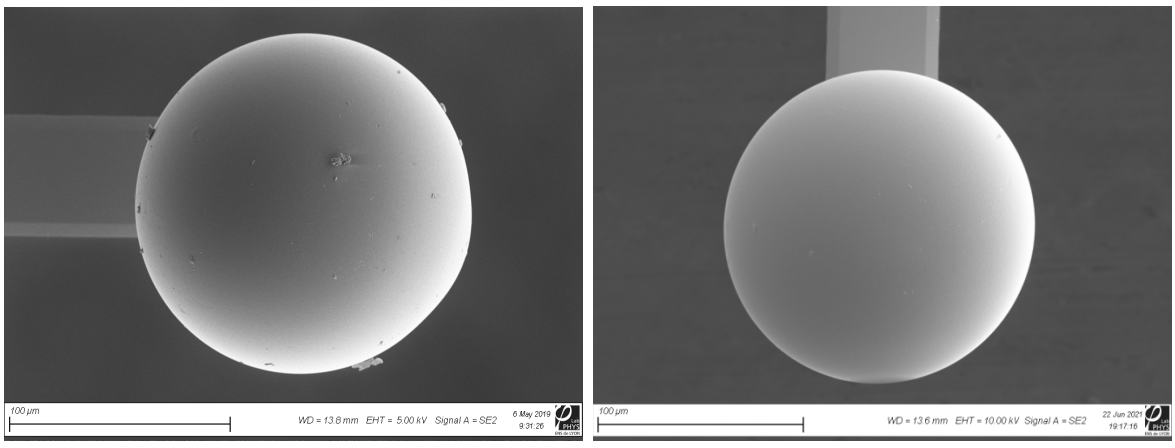

Figure 9.8: Left: SEM image of a typical sample using previous protocol in the team. Many particles can be seen. Right: SEM image of a sample obtained with the protocol presented here. The surface is much cleaner.

AFM imaging can bring more information about the local properties of the surface, especially the roughness of surfaces. We take a standard AFM image of the surface of a sphere, over a region of 250 × 500nm (figure 9.10). Since the sphere is supported itself by a cantilever, we need to carefully chose the cantilever used for imaging the sphere. As a force is applied

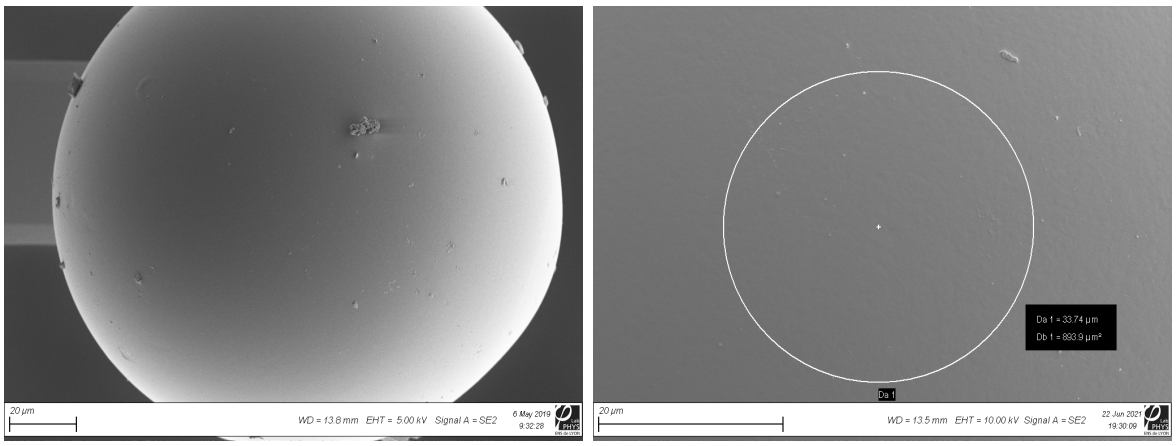

Figure 9.9: Left: Close-up on the sphere from left figure 9.8. Right: Close-up on the sphere from right figure 9.8. The close-up is taken on the area that will be the closest from the plane in the force measurement.

during the contact between the imaging tip and the sphere, both cantilevers will deflect, with a deflection inversely proportional to the contact force. We need to use a cantilever soft enough so that the sample cantilever doesn't deflect too much. The imaging cantilever used is a BudgetSensor All-in-one B, with a stiffness $7\,\mathrm{N\,m^{-1}}$, while our cantilevers have a stiffness about $0.5\,\mathrm{N\,m^{-1}}$. The scan is performed in contact mode with a 7 nN setpoint. The rms roughness of the surface is measured at 2.5 nm from the AFM map.

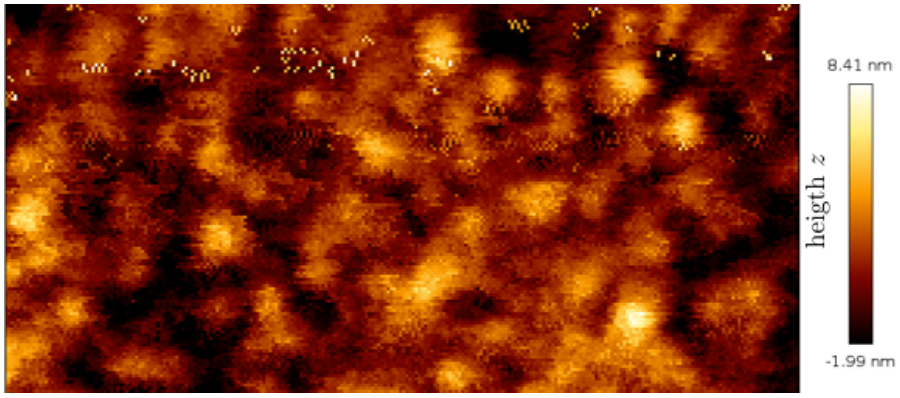

Figure 9.10: 250×500nm AFM map of the surface of a sphere after gold deposition. The structure of the gold layer can be seen. The measured roughness is $\sqrt{\langle z^2 \rangle} = 2.5\,\mathrm{nm}$ rms.

We develop a microfabrication process for our force measurement probes. By taking great care of cleanliness of the samples and the detail of the metal deposition techniques, we obtain samples with clean surfaces and low roughness.

9.4 Casimir force measurements

Now we use the crafted probes with the commercial golden silicon wafer to measure the Casimir force. The surface is brought at a distance of 2 µm from the probe, and the system is let to stabilise for 2 hours. The distance between the probe and the surface is monitored using the electrostatic measurement from 9.2.1 and adjusted to the target value by using the piezoelectric actuator.

The surface is approached slowly at a speed of $10\,\mathrm{nm\,s^{-1}}$ up to $d = 400\,\mathrm{nm}$. The approach is slowed to a speed of $2\,\mathrm{nm\,s^{-1}}$ between 400 nm and 100 nm, then to $1\,\mathrm{nm\,s^{-1}}$ between 100 nm

and 50 nm. Slowing the approach allows us to have a better statistic and resolution on the force curve. Once the distance reaches 50 nm, the displacement is reversed, back to 1 µm. This cycle is performed 50 times. For each second of acquisition, the electrostatic distance is computed, and the constant force is measured as $F = k\langle x \rangle$, where $\langle \cdot \rangle$ is a statistical average taken over one second. This results in a force curve $F(d)$, shown in figure 9.11, averaged over the 50 cycles, by imposing that $F(d = 1\,\mu\text{m}) = 0$. We can compare these new measurements with data from a previous experiment in the group (orange curve in fig. 9.11), obtained using the contact between the sphere and the plane as a reference for distance measurement. Our data match the previous measurement and extends the range of measurement by a factor of two (from 100 nm to 50 nm).

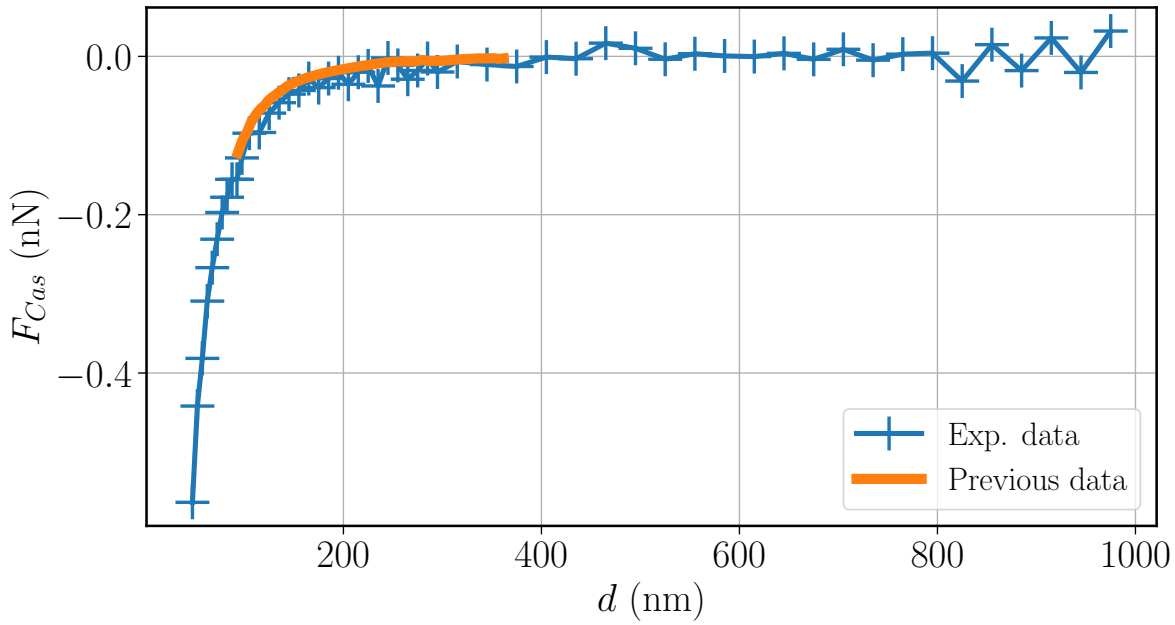

Figure 9.11: Blue: Measured force curve of the sphere-plane Casimir interaction. The force curve is averaged over 50 cycles. Orange: Previous data without electric measurement of d.

9.5 Conclusions

We develop a protocol for careful microfabrication of force measurement probes. By combining these probes with a low-noise interferometric setup and an electric measurement of the sphere-plane distance, we are able to measure the Casimir force for a separation as close as 50 nm. In this work we developed microfabrication techniques that can be used to craft custom cantilevers and can be used in the future to engineer the mechanical properties of cantilevers for other experiments. In chapter 3, we mentioned the necessity to isolate the first flexural mode of the cantilevers for stochastic thermodynamic protocols. Using the techniques presented in this chapter and the models from chapter 8, we can load cantilevers to separate their different modes or change their mechanical response.

Conclusions on cantilever functionalisation

In chapter 8 we presented two models for the description of cantilever loaded with colloidal probe. We describe the different flexural modes, their shape, and their mechanical response (frequency, stiffness). We also propose a method based on frequency ratios to extract the relevant geometrical parameters from measurements of the fluctuations spectrum. This can be seen as an extension of the Simple Harmonic Oscillator calibration technique we presented in chapter 3.

In chapter 9 we describe a force measurement setup dedicated to small forces, on the scale of the nanonewton, with a direct distance measurement technique based on the response to an electrostatic force. To obtain high quality surfaces for our samples, we developed a microfabrication process for functionalisation of micro-cantilever with wich we obtained clean, low-roughness surfaces. These samples were used to measure the Casimir interaction in a sphere-plane geometry, in good agreement with previous measurements.

The theoretical models from chapter 8, coupled to our microfabrication technique from chapter 9 give us everything we need to design and craft samples for specific applications. For example, we can design loaded cantilevers with a given repartition of the modes frequencies that can be used to isolate the first flexural mode for stochastic thermodynamic experiments. We can also imagine functionalising the cantilever with specific probes to apply forces other than electrostatic, while still controlling the mechanical response of the cantilever. This mastery of cantilever functionalisation coupled to the tunable feedback loop makes our experimental setup even more versatile, opening many possibilities of future experiments.

Bibliography

[1]Donald E. Simanek, *Perpetual futility a short history of the search for perpetual motion.* `http://web.archive.org/web/20100109053102/http://www.lhup.edu/~dsimanek/museum/people/people.htm`.

[2]Museo Galileo Firenze, *Leonardo da vinci and perpetual motion*, `https://mostre.museogalileo.it/motoperpetuo/en/`.

[3]C. Van Den Broeck, "The many faces of the second law", Journal of Statistical Mechanics: Theory and Experiment **2010**, P10009 (2010).

[4]R. Clausius, "I. on the moving force of heat, and the laws regarding the nature of heat itself which are deducible therefrom", The London, Edinburgh, and Dublin Philosophical Magazine and Journal of Science **2**, Publisher: Taylor & Francis, 1–21 (1851).

[5]Sadi Carnot, "Réflexions sur la puissance motrice du feu", (1824).

[6]J. C. Maxwell, "Illustrations of the dynamical theory of gases. part i. on the motions and collisions of perfectly elastic spheres", Philosophical Magazine, 19–32 (1860).

[7]Ludwig Boltzmann, "Weitere studien über das wärmegleichgewicht unter gasmolekülen.", Sitzungsberichte der Kaiserlichen Akademie der Wissenschaften in Wien **66**, 275–370 (1872).

[8]R. Brown, "A brief account of microscopical observations made in the months of june, july, and august 1827, on the particles contained in the pollen of plants; and on the general existence of active molecules in organic and inorganic bodies", The Edinburgh New Philosophical Journal (1828).

[9]A. Einstein, "Über die von der molekularkinetischen Theorie der Wärme geforderte Bewegung von in ruhenden Flüssigkeiten suspendierten Teilchen", Annalen der Physik **322**, 549–560 (1905).

[10]j. Perrin, *Les atomes* (1913).

[11]M. Von Smoluchowski, "Zur kinetischen Theorie der Brownschen Molekularbewegung und der Suspensionen", Annalen der Physik **326**, 756–780 (1906).

[12]L. Szilard, "Ober die Entropieverminderung in einem thermo- dynamischen System bei Eingriffen intelligenter VCesen.",

[13]R. Feynman, "The feynman lectures on physics vol. i ch. 46: ratchet and pawl", in *The feynman lectures on physics vol. i* (1963).

[14]R. Landauer, "Irreversibility and heat generation in the computing process", IBM Journal of Research and Development **5**, 183–191 (1961).

[15]A. Bérut, A. Arakelyan, A. Petrosyan, S. Ciliberto, R. Dillenschneider, and E. Lutz, "Experimental verification of landauer's principle linking information and thermodynamics", Nature **483**, 187–189 (2012).

[16]S. Dago, J. Pereda, N. Barros, S. Ciliberto, and L. Bellon, "Information and thermodynamics: fast and precise approach to landauer's bound in an underdamped micromechanical oscillator", Physical Review Letters **126**, 170601 (2021).

[17]E. Lutz and S. Ciliberto, "Information: from maxwell's demon to landauer's eraser", Physics Today **68**, 30–35 (2015).

[18]A. Deshpande, M. Gopalkrishnan, T. E. Ouldridge, and N. S. Jones, "Designing the optimal bit: balancing energetic cost, speed and reliability", Proceedings of the Royal Society A: Mathematical, Physical and Engineering Sciences **473**, 20170117 (2017).

[19]L. Martini, M. Pancaldi, M. Madami, P. Vavassori, G. Gubbiotti, S. Tacchi, F. Hartmann, M. Emmerling, S. Höfling, L. Worschech, and G. Carlotti, "Experimental and theoretical analysis of landauer erasure in nano-magnetic switches of different sizes", Nano Energy **19**, 108–116 (2016).

[20]A. O. Orlov, C. S. Lent, C. C. Thorpe, G. P. Boechler, and G. L. Snider, "Experimental test of landauer's principle at the sub-k $_{B}$ t level", Japanese Journal of Applied Physics **51**, 06FE10 (2012).

[21]J. Hong, B. Lambson, S. Dhuey, and J. Bokor, "Experimental test of landauer's principle in single-bit operations on nanomagnetic memory bits", Science Advances **2**, e1501492 (2016).

[22]L. L. Yan, T. P. Xiong, K. Rehan, F. Zhou, D. F. Liang, L. Chen, J. Q. Zhang, W. L. Yang, Z. H. Ma, and M. Feng, "Single-atom demonstration of the quantum landauer principle", Physical Review Letters **120**, 210601 (2018).

[23]Y. Jun, M. Gavrilov, and J. Bechhoefer, "High-precision test of landauer's principle in a feedback trap", Physical Review Letters **113**, 190601 (2014).

[24]R. Gaudenzi, E. Burzurí, S. Maegawa, H. S. J. Van Der Zant, and F. Luis, "Quantum landauer erasure with a molecular nanomagnet", Nature Physics **14**, 565–568 (2018).

[25]T. M. Cover and J. A. Thomas, *Elements of information theory*, 2nd ed, OCLC: ocm59879802 (Wiley-Interscience, Hoboken, N.J, 2006), 748 pp.

[26]S. Verdú, "Empirical estimation of information measures: a literature guide", Entropy **21**, 720 (2019).

[27]C. Van Den Broeck, "Bits for less or more for bits?", Nature Physics **6**, 937–938 (2010).

[28]U. Seifert, "Stochastic thermodynamics: principles and perspectives", The European Physical Journal B **64**, 423–431 (2008).

[29]Paul Langevin, "Comptes rendus hebdomadaires des séances de l'Académie des sciences / publiés... par MM. les secrétaires perpétuels", comptes rendus de l'académie des sciences **146**, 530–532 (1908).

[30]K. Sekimoto, "Langevin equation and thermodynamics", Progress of Theoretical Physics Supplement **130**, 17–27 (1998).

[31]C. Jarzynski, "Equalities and inequalities: irreversibility and the second law of thermodynamics at the nanoscale", Annual Review of Condensed Matter Physics **2**, 329–351 (2011).

[32]U. Seifert, "Stochastic thermodynamics, fluctuation theorems and molecular machines", Reports on Progress in Physics **75**, 126001 (2012).

[33]C. Jarzynski, "Nonequilibrium equality for free energy differences", Physical Review Letters **78**, 2690–2693 (1997).

[34]C. P. Broedersz and P. Ronceray, "Twenty-five years of nanoscale thermodynamics", Nature **604**, Bandiera_abtest: a Cg_type: News And Views Number: 7904 Publisher: Nature Publishing Group Subject_term: Biophysics, Physics, 46–47 (2022).

[35]J. Liphardt, S. Dumont, S. B. Smith, I. Tinoco, and C. Bustamante, "Equilibrium information from nonequilibrium measurements in an experimental test of jarzynski's equality", Science **296**, 1832–1835 (2002).

[36]T. Hatano, "Jarzynski equality for the transitions between nonequilibrium steady states", Physical Review E **60**, R5017–R5020 (1999).

[37]T. Hatano and S.-i. Sasa, "Steady-state thermodynamics of langevin systems", Physical Review Letters **86**, 3463–3466 (2001).

[38]E. H. Trepagnier, C. Jarzynski, F. Ritort, G. E. Crooks, C. J. Bustamante, and J. Liphardt, "Experimental test of hatano and sasa's nonequilibrium steady-state equality", Proceedings of the National Academy of Sciences **101**, 15038–15041 (2004).

[39]J. Kurchan, *A quantum fluctuation theorem*, Aug. 16, 2001.

[40]H. Tasaki, *Jarzynski relations for quantum systems and some applications*, Sept. 25, 2000.

[41]S. An, J.-N. Zhang, M. Um, D. Lv, Y. Lu, J. Zhang, Z.-Q. Yin, H. T. Quan, and K. Kim, "Experimental test of the quantum jarzynski equality with a trapped-ion system", Nature Physics **11**, 193–199 (2015).

[42]G. E. Crooks, "Entropy production fluctuation theorem and the nonequilibrium work relation for free energy differences", Physical Review E **60**, 2721–2726 (1999).

[43]F. Douarche, S. Ciliberto, A. Petrosyan, and I. Rabbiosi, "An experimental test of the jarzynski equality in a mechanical experiment", Europhysics Letters (EPL) **70**, 593–599 (2005).

[44]D. Collin, F. Ritort, C. Jarzynski, S. B. Smith, I. Tinoco, and C. Bustamante, "Verification of the crooks fluctuation theorem and recovery of RNA folding free energies", Nature **437**, 231–234 (2005).

[45]H. S. Leff and A. F. Rex, eds., *Maxwell's demon 2: entropy, classical and quantum information, computing*, OCLC: ocm51569169 (Institute of Physics, Bristol ; Philadelphia, 2003), 485 pp.

[46]H. S. Leff and A. F. Rex, eds., *Maxwell's demon: entropy, information, computing* (Adam Hilger, Bristol, 1990), 349 pp.

[47]A. C. Barato and U. Seifert, "Thermodynamic cost of external control", New Journal of Physics **19**, 073021 (2017).

[48]D. Mandal and C. Jarzynski, "Work and information processing in a solvable model of maxwell's demon", Proceedings of the National Academy of Sciences **109**, 11641–11645 (2012).

[49]M. Lagoin, "Thermodynamique dans les systèmes stationnaires hors équilibre macroscopiques: démons de Maxwell et machines thermiques aléatoires", PhD thesis (École Normale Supérieure de Lyon, 2023).

[50]T. Sagawa and M. Ueda, "Generalized jarzynski equality under nonequilibrium feedback control", Physical Review Letters **104**, 090602 (2010).

[51]J. V. Koski, V. F. Maisi, T. Sagawa, and J. P. Pekola, "Experimental observation of the role of mutual information in the nonequilibrium dynamics of a maxwell demon", Physical Review Letters **113**, 030601 (2014).

[52]S. Toyabe, T. Sagawa, M. Ueda, E. Muneyuki, and M. Sano, "Experimental demonstration of information-to-energy conversion and validation of the generalized jarzynski equality", Nature Physics **6**, 988–992 (2010).

[53]L. Bellon, S. Ciliberto, H. Boubaker, and L. Guyon, "Differential interferometry with a complex contrast", Optics Communications **207**, 49–56 (2002).

[54]P. Paolino, F. A. Aguilar Sandoval, and L. Bellon, "Quadrature phase interferometer for high resolution force spectroscopy", Review of Scientific Instruments **84**, 095001 (2013).

[55]L. Bellon, *Exploring nano-mechanics through thermal fluctuations* (HDR, École Normale Supérieure de Lyon, 2010).

[56]S. Dago, "Stochastic thermodynamics: driving of micro-oscillators applied to the study and the optimisation of information processing", PhD thesis (École Normale Supérieure de Lyon, 2022).

[57]C. Kwon, J. D. Noh, and H. Park, "Work fluctuations in a time-dependent harmonic potential: rigorous results beyond the overdamped limit", Physical Review E **88**, 062102 (2013).

[58]K. Sekimoto, F. Takagi, and T. Hondou, "Carnot's cycle for small systems: irreversibility and cost of operations", Physical Review E **62**, 7759–7768 (2000).

[59]I. A. Martínez, É. Roldán, L. Dinis, D. Petrov, and R. A. Rica, "Adiabatic processes realized with a trapped brownian particle", Physical Review Letters **114**, 120601 (2015).

[60]I. A. Martínez, É. Roldán, L. Dinis, D. Petrov, J. M. R. Parrondo, and R. A. Rica, "Brownian carnot engine", Nature Physics **12**, 67–70 (2016).

[61]V. Blickle and C. Bechinger, "Realization of a micrometre-sized stochastic heat engine", Nature Physics **8**, 143–146 (2012).

[62]S. Rana, P. S. Pal, A. Saha, and A. M. Jayannavar, "Single-particle stochastic heat engine", Physical Review E **90**, 042146 (2014).

[63]S. Bo and A. Celani, "Entropic anomaly and maximal efficiency of microscopic heat engines", Physical Review E **87**, 050102 (2013).

[64]T. Schmiedl and U. Seifert, "Efficiency at maximum power: an analytically solvable model for stochastic heat engines", EPL (Europhysics Letters) **81**, 20003 (2008).

[65]J.-M. Park, J. S. Lee, and J. D. Noh, "Optimal tuning of a confined brownian information engine", Physical Review E **93**, 032146 (2016).

[66]Y. Ashida, K. Funo, Y. Murashita, and M. Ueda, "General achievable bound of extractable work under feedback control", Physical Review E **90**, 052125 (2014).

[67]G. Paneru, D. Y. Lee, T. Tlusty, and H. K. Pak, "Lossless brownian information engine", Physical Review Letters **120**, 020601 (2018).

[68]J. C. Maxwell, *Theory of heat*, 1st ed. (Cambridge University Press, June 2, 2011).

[69]A. Rex, "Maxwell's demon—a historical review", Entropy **19**, 240 (2017).

[70]N. Cottet, S. Jezouin, L. Bretheau, P. Campagne-Ibarcq, Q. Ficheux, J. Anders, A. Auffèves, R. Azouit, P. Rouchon, and B. Huard, "Observing a quantum maxwell demon at work", Proceedings of the National Academy of Sciences **114**, 7561–7564 (2017).

[71]M. D. Vidrighin, O. Dahlsten, M. Barbieri, M. S. Kim, V. Vedral, and I. A. Walmsley, "Photonic maxwell's demon", Physical Review Letters **116**, 050401 (2016).

[72]T. Admon, S. Rahav, and Y. Roichman, "Experimental realization of an information machine with tunable temporal correlations", Physical Review Letters **121**, 180601 (2018).

[73]P. Orem and F. Orem, "Implementing demons and ratchets", Entropy **19**, 34 (2017).

[74]N. Freitas and M. Esposito, "Information flows in macroscopic maxwell's demons", Physical Review E **107**, 014136 (2023).

[75]N. Freitas and M. Esposito, "Maxwell demon that can work at macroscopic scales", Physical Review Letters **129**, 120602 (2022).

[76]S. Ciliberto, "Autonomous out-of-equilibrium maxwell's demon for controlling the energy fluxes produced by thermal fluctuations", Physical Review E **102**, 050103 (2020).

[77]J. Rojas, I. Rivera, A. Figueroa, and F. Vázquez, "Coupled thermoelectric devices: theory and experiment", Entropy **18**, 255 (2016).

[78]J. V. Koski and J. P. Pekola, "Maxwell's demons realized in electronic circuits", Comptes Rendus Physique **17**, 1130–1138 (2016).

[79]O. Chor, A. Sohachi, R. Goerlich, E. Rosen, S. Rahav, and Y. Roichman, *A many-body szilard engine with giant number fluctuations*, Aug. 21, 2023.

[80]V. Serreli, C.-F. Lee, E. R. Kay, and D. A. Leigh, "A molecular information ratchet", Nature **445**, 523–527 (2007).

[81]M. Ribezzi-Crivellari and F. Ritort, "Large work extraction and the landauer limit in a continuous maxwell demon", Nature Physics **15**, 660–664 (2019).

[82]M. Lagoin, C. Crauste-Thibierge, and A. Naert, "Human-scale brownian ratchet: a historical thought experiment", Physical Review Letters **129**, 120606 (2022).

[83]F. J. Giessibl, "Advances in atomic force microscopy", Rev. Mod. Phys. **75**, 949–983 (2003).

[84]H.-J. Butt, B. Cappella, and M. Kappl, "Force measurements with the atomic force microscope: technique, interpretation and applications", Surf. Sci. Rep. **59**, 1 (2005).

[85]T. G. Kuznetsova, M. N. Starodubtseva, N. I. Yegorenkov, S. A. Chizhik, and R. I. Zhdanov, "Atomic force microscopy probing of cell elasticity", Micron **38**, 824 (2007).

[86]D. J. Müller and Y. F. Dufrêne, "Atomic force microscopy as a multifunctional molecular toolbox in nanobiotechnology", Nature Nanotech. **3**, 261 (2008).

[87]A. Maali and B. Bhushan, "Nanorheology and boundary slip in confined liquids using atomic force microscopy", J. Phys. Condens. Matter **20**, 315201 (2008).

[88]J. Laurent, H. Sellier, A. Mosset, S. Huant, and J. Chevrier, "Casimir force measurements in au-au and au-si cavities at low temperature", Physical Review B **85**, 035426 (2012).

[89]M. Kim and J. R. Chelikowsky, "CO tip functionalization in subatomic resolution atomic force microscopy", Appl. Phys. Lett. **107**, 163109 (2015).

[90]M. Chighizola, L. Puricelli, L. Bellon, and A. Podestà, "Large colloidal probes for atomic force microscopy: fabrication and calibration issues", J. Mol. Recognit.. **34**, e2879 (2020).

[91]A. Eskhan and D. Johnson, "Microscale characterization of abiotic surfaces and prediction of their biofouling/anti-biofouling potential using the afm colloidal probe technique", Adv. Colloid Interface Sci. **310**, 102796 (2022).

[92]H. Holuigue, E. Lorenc, M. Chighizola, C. Schulte, L. Varinelli, M. Deraco, M. Guaglio, M. Gariboldi, and A. Podesta, "Force sensing on cells and tissues by atomic force microscopy", Sensors **22**, 2197 (2022).

[93]E. Kim and H. Lee, "Mechanical characterization of soft microparticles prepared by droplet microfluidics", J. Polymer Sci. **60**, 1670 (2022).

[94]V. Sharma, X. Shi, G. Yao, G. M. Pharr, and J. Y. Wu, "Surface characterization of an ultra-soft contact lens material using an atomic force microscopy nanoindentation method", Sci. Rep. **12**, 20013 (2022).

[95]K. Xu and Y. Liu, "Studies of probe tip materials by atomic force microscopy: a review", Beilstein J. Nanotechnol. **13**, 1256 (2022).

[96]T. Zielinski, J. Pabijan, B. Zapotoczny, J. Zemla, J. Wesolowska, J. Pera, and M. Lekka, "Changes in nanomechanical properties of single neuroblastoma cells as a model for oxygen and glucose deprivation (ogd)", Sci. Rep. **12**, 16276 (2022).

[97]N. Zimron-Politi and R. C. Tung, "Experimental validation of contact resonance AFM using long massive tips", Nanotechnology **34**, 365712 (2023).

[98]E. Lorenc, L. Varinelli, M. Chighizola, S. Brich, F. Pisati, M. Guaglio, D. Baratti, M. Deraco, M. Gariboldi, and A. Podesta, "Correlation between biological and mechanical properties of extracellular matrix from colorectal peritoneal metastases in human tissues", Sci. Rep. **13**, 12175 (2023).

[99]N. A. Burnham, X. Chen, C. S. Hodges, G. A. Matei, E. J. Thoreson, C. J. Roberts, M. C. Davies, and S. J. B. Tendler, "Comparison of calibration methods for atomic-force microscopy cantilevers", Nanotechnology **14**, 1 (2002).

[100]H. .-. Butt and M. Jaschke, "Calculation of thermal noise in atomic force microscopy", Nanotechnology **6**, 1 (1995).

[101]J. Rodriguez-Ramos and F. Rico, "Determination of calibration parameters of cantilevers of arbitrary shape by finite element analysis", Rev. Sci. Instrum. **92**, 045001 (2021).

[102]H. Li, Y. Chen, and L. Dai, "Concentrated-mass cantilever enhances multiple harmonics in tapping-mode atomic force microscopy", Appl. Phys. Lett. **92**, 151903 (2008).

[103]M. S. Allen, H. Sumali, and P. C. Penegor, "DMCMN: Experimental/Analytical Evaluation of the Effect of Tip Mass on Atomic Force Microscope Cantilever Calibration", J. Dyn. Sys., Meas., Control. **131**, 064501 (2009).

[104]J. Laurent, A. Steinberger, and L. Bellon, "Functionalized AFM probes for force spectroscopy: eigenmode shapes and stiffness calibration through thermal noise measurements", Nanotechnology **24**, 225504 (2013).

[105]D. Oguamanam, "Free vibration of beams with finite mass rigid tip load and flexural–torsional coupling", Int. J. Mech. Sci. **45**, 963 (2003).

[106]S. A. Edwards, W. A. Ducker, and J. E. Sader, "Influence of atomic force microscope cantilever tilt and induced torque on force measurements", J. Appl. Phys. **103**, 064513 (2008).

[107]P. Paolino, B. Tiribilli, and L. Bellon, "Direct measurement of spatial modes of a microcantilever from thermal noise", J. Appl. Phys. **106**, 094313 (2009).

[108]A. Gambassi, A. Maciołek, C. Hertlein, U. Nellen, L. Helden, C. Bechinger, and S. Dietrich, "Critical casimir effect in classical binary liquid mixtures", Physical Review E **80**, 061143 (2009).

[109]C. Hertlein, L. Helden, A. Gambassi, S. Dietrich, and C. Bechinger, "Direct measurement of critical casimir forces", Nature **451**, 172–175 (2008).

[110]I. Martínez, C. Devailly, A. Petrosyan, and S. Ciliberto, "Energy transfer between colloids via critical interactions", Entropy **19**, 77 (2017).

[111]L. Helden, T. Knippenberg, L. Tian, A. Archambault, F. Ginot, and C. Bechinger, "Critical casimir interactions of colloids in micellar critical solutions", Soft Matter, 10.1039.D0SM02021D (2021).

[112]H. B. G. Casimir and D. Polder, "The influence of retardation on the london-van der waals forces", Physical Review **73**, 360–372 (1948).

[113]H. B. Casimir, "On the attraction between two perfectly conducting plates", in Proc. kon. ned. akad. wet. Vol. 51 (1948), p. 793.

[114]S. K. Lamoreaux, "Demonstration of the casimir force in the 0.6 to 6 mm range", Physical Review Letters **78** (1997).

[115]R. S. Decca, D. López, E. Fischbach, and D. E. Krause, "Measurement of the casimir force between dissimilar metals", Physical Review Letters **91**, 050402 (2003).

[116]A. Le Cunuder, A. Petrosyan, G. Palasantzas, V. Svetovoy, and S. Ciliberto, "Measurement of the casimir force in a gas and in a liquid", Physical Review B **98**, 201408 (2018).

[117]J. Laurent, "Mesures de la force de casimir à basse température", PhD thesis (Université de Grenoble, 2006).

[118]S. Albert, A. Archambault, A. Petrosyan, C. Crauste-Thibierge, L. Bellon, and S. Ciliberto, "Calibrated force measurement in atomic force microscopy using the transient fluctuation theorem", EPL (Europhysics Letters) **131**, 10008 (2020).

[119]É. Durand, *Electrostatique*, Masson, Vol. 1 (1964).

[120]J. M. Crowley, "Simple expressions for force and capacitance for a conductive sphere near a conductive wall",

[121]S. de Man, K. Heeck, and D. Iannuzzi, "No anomalous scaling in electrostatic calibrations for casimir force measurements", Physical Review A **79**, 024102 (2009).

[122]P. Paolino and L. Bellon, "Frequency dependence of viscous and viscoelastic dissipation in coated micro-cantilevers from noise measurement", Nanotechnology **20**, 405705 (2009).